# IMPROVING QUANTITATIVE INFRARED IMAGING FOR MEDICAL DIAGNOSTIC APPLICATIONS

by
Tze-Yuan Cheng

A dissertation submitted to Johns Hopkins University in conformity with the requirements for the degree of Doctor of Philosophy

Baltimore, Maryland
February, 2015

# Abstract

Infrared (IR) thermography is a non-ionizing and non-invasive imaging modality that allows the measurement of the spatial and temporal variations of the infrared radiation emitted by the human body. The emitted radiation and the skin surface temperature that can be derived from the emitted radiation data carry a wealth of information about different processes within the human body. To advance the quantitative use of IR thermography in medical diagnostics, this dissertation investigates several issues critical to the demands imposed by clinical applications.

We developed a computational thermal model of the human skin with multiple layers and a near-surface lesion to understand the thermal behavior of skin tissue in dynamic infrared imaging. With the aid of this model, various cooling methods and conditions suitable for the clinical application of dynamic IR imaging are critically evaluated. The analysis of skin cooling provides a quantitative basis for the selection and optimization of cooling conditions in the clinical practice of dynamic IR imaging.

To improve the quantitative accuracy for the analysis of dynamic IR imaging, we proposed a motion tracking approach using a template-based algorithm. The motion tracking approach is capable of following the involuntary motion of the subject in the IR image sequence, thereby allowing us to track the temperature evolution for a particular region on the skin.

In addition, to compensate for the measurement artifacts induced by the surface curvature in IR thermography, a correction formula was developed based on the emissivity model and phantom experiments. The correction formula was integrated into a 3D imaging procedure based on a system combining Kinect and IR cameras. We demonstrated the feasibility of mapping 2D IR images onto the 3D surface of the human body. The accuracy of temperature measurement was improved by applying the correction method.

Finally, we designed a variety of quantitative approaches to analyze the clinical data acquired from patient studies of pigmented lesions and hemangiomas. These approaches allow us to evaluate the thermal signatures of lesions with different characteristics, measured in both static and dynamic IR imaging.

The collection of methodologies described in this dissertation, leading to improved ease of use and accuracy, can contribute to the broader implementation of quantitative IR thermography in medical diagnostics.

Primary Reader: Cila Herman

Secondary Reader: Robert Ivkov

Tertiary Reader: Michael E. Thomas

# Acknowledgements

First I want to give my greatest gratitude to my PhD advisor- Prof. Cila Herman, who had provided the most valuable guidance and support throughout my graduate school career, and it has been a great honor to be her PhD student. As the best role model for a scientist, mentor, and teacher, Prof. Herman has been helpful in providing insightful discussion in my study and research. I also want to thank the committee of dissertation- Dr. Robert Ivkov and Dr. Michael E. Thomas for their valuable advice and insights that greatly enrich this thesis.

In addition, I thank our MD collaborators in Johns Hopkins Children's Center- Dr. Bernard Cohen and Dr. Annie Grossberg for providing their help to the IRB and the patient study of infantile hemangiomas. I would also like to acknowledge the contributions of Dr. Müge Pirtini Çetingül for collecting the clinical IR thermograph data of pigmented lesions, the help of Dr. Rhoda Alani to the IRB and the patient study, as well as the support of Dr. Sewon Kang and his department during the patient study.

I also want to show appreciation to all the members and alumni in Heat Transfer Lab- Akanksha Bhargava, Srikamal Kandala, Rajeev Hatwar, Daxiang Deng, Yuanyang Li, Xinrong You, Jianan Wang, Cameron Ahmad, Andrew Frazier, Alice Fang. They all provided indispensable assistance in the imaging experiments and clinical study in this

thesis. The lab also became an enjoyable place because of their supportive friendship, which gave me energy to tackle the difficulties encountered in my research.

Furthermore, I express my gratitude for the financial support provided by the National Science Foundation, the Alexander and Margaret Stewart Trust through the Cancer Center of the Johns Hopkins University, and National Institutes of Health NCI Grant.

Lastly, I would like to thank my family in Taiwan– my parents and sister for giving me all kinds of unconditional support through these years in United States. This work is dedicated to them, and I hope my dad in heaven would be proud of me.

# Contents

# List of Tables



# List of Figures

# Chapter 1 Introduction

## 1.1 Background

Thermoregulation is a physiological mechanism that maintains the temperature of the human body within specific, relatively narrow, boundaries. It responds to changes in the ambient and other external and internal variations (caused by disease, physical activity, mechanical or chemical stress and other factors) by controlling the rates of heat generation and heat loss. There is a large body of evidence that disease or deviation from normal function is accompanied by changes of body temperature, which again affect the temperature of the body surface (skin). For example, the behavior and appearance of some benign and cancerous lesions [1-9] and other inflammatory [10-12] processes differ from those of healthy tissue in terms of heat generation, because of a combination of inflammation, increased metabolic rate, interstitial hypertension, abnormal vessel morphology and lack of response to homeostatic signals.

The human body is a complex biophysical system because numerous parameters affect the temperature distribution within the body: understanding, modeling, and controlling these has been a quest since the early days of medicine. Clearly, accurate data

about the temperature of the human body and skin, in addition to shape and color information, would be invaluable for a better understanding and diagnosing of the many complex processes. This information can be coupled with a high fidelity thermal (computational) model of the body to provide a wealth of information on the processes responsible for heat generation and thermoregulation, in particular the deviation from normal conditions that can be caused by disease, for diagnostic purposes as well as for the planning of treatment strategies.

Medical thermometers provide local estimates of the core body temperature. However, accurate temperature measurements of the human body, especially 3D temperature mapping of the skin temperature still remain a challenge. Body surface temperature and surface temperature in general are difficult to measure accurately using conventional sensors, since applying the sensor to the skin can in itself change the surface temperature distribution. Attempts with thermochromatic liquid crystals did not lead to quantitative diagnostic tools because of difficulties related to the application of the sensor, its influence on the temperature distribution of the surface to which it is applied and calibration issues. While researchers have been attempting to develop thermographic techniques (thermocromatic crystals, infrared thermography) for diagnostic applications for over four decades, they faced numerous challenges associated with the complexity of the investigated geometry, variations of surface properties and complexities of the imaging hardware.

Non-invasive in-vivo imaging techniques are of particular interest in diagnostic applications, such as the early detection of cancer, wound care, assessment of lesions, etc. Some of these imaging techniques, including digital photography, dermoscopy,

multispectral imaging, laser-based systems, ultrasound imaging, and magnetic resonance imaging, have been studied in the literature [13-18]. The review of past studies [13-18] suggests that the aforementioned imaging tools provide improvement in recognizing malignant lesions. However, most of these in-vivo imaging techniques still rely on subjective interpretation in clinical practice and lack quantitative standards for measurement [13]. While some of these diagnostic tools hold the potential in reducing the unnecessary biopsies [15], development of quantitative diagnostic criteria requires extensive clinical studies and fine tuning of instrumentation and decision making criteria based on the results of these studies. This dissertation aims at improving the image processing and measurement accuracy associated with infrared imaging in clinical applications. In view of the growing demand for objective and quantitative diagnostic tools that can be utilized in primary care specialized clinics and even telemedicine, the quantitative information provided by infrared (IR) thermography offers advantages over conventional approaches, as a versatile, relatively low-cost, easy-to-use and objective diagnostic tool in a variety of clinical applications.

Infrared (IR) thermography is a non-invasive imaging modality that allows the measurement of the spatial and temporal variations of the electromagnetic radiation emitted in the IR region of the spectrum by the object under study, which is the human body in this thesis. The emitted radiation and the skin surface temperature that can be derived from the emitted radiation data carry a wealth of information about different processes within the human body. The medical community embraced infrared imaging with enthusiasm in the sixties and attempts of quantitative diagnostic efforts were reported over the following two decades [9, 10, 19]. Following the initial enthusiasm

interest waned, as early results did not meet expectations, due to insufficient temperature measurement accuracy, insufficient spatial resolution, lack of thorough insight into the underlying thermal processes, lack of adequate control of measurement and ambient conditions, complexity of implementation and equipment size, as well as cost [20]. Even though over the past four decades a considerable amount of effort focused on using IR imaging in medical diagnostics, the accurate quantification of skin temperature distributions based on IR emission measurements remained an elusive task. Until recently, infrared imaging was mainly used as a research tool to gain additional qualitative insight into the temperature patterns of the skin, and its value in medical diagnostics was limited.

One of the rare FDA approved applications of IR thermography, breast cancer imaging, is qualitative [11, 21] and it is not widely used because early studies indicated that thermography yields too many false positive diagnoses of breast cancer. However, a longitudinal follow-up study of breast cancer patients conducted by Handley [22] in 1962 showed that the patients with 3 $^{o}$C temperature rise were more likely to present cancer in the future than those with only 1-2 $^{o}$C temperature rise. In 1980, Gautherie and Gros conducted another longitudinal study with a group of 1245 females [23] who had an abnormal IR image, but appeared to be normal under the conventional testing methods, including physical exam, mammography, ultrasound, and biopsy. They reported that within the subsequent five years, more than one third of the group with abnormal thermographic findings was diagnosed with breast cancer histologically. These two studies suggest that IR thermography holds potential to serve as a quantitative predictor, and it is also more sensitive than the conventional methods to detect early stage breast cancer.

Infrared imaging has experienced a revival and a revolution over the past 15 years as a result of the development of new materials used in focal plane arrays, new cooling methods that replaced cooling with liquid nitrogen and the introduction of novel uncooled detectors. This dramatic technology development was accompanied by the decrease of the cost of IR imaging systems since 2005. As a consequence, IR imagers that can yield high accuracy and high spatial and temporal resolution data have become available at a reasonable price. These developments were accompanied by the rapid progress in computer technology as well as the advances in computer vision algorithms since the 1990s, enabling novel and sophisticated applications. While military applications rely heavily on these new developments, progress is not yet reflected in medical applications. The research described in this thesis is a step in that direction.

IR thermography can be implemented either as a static or a dynamic technique in medical diagnostic applications. In static IR imaging, a steady state situation is measured: the patient is generally in thermal equilibrium, with normal ambient conditions present. The spatial distribution of thermal radiation emitted by the body is acquired and analyzed. In contrast, dynamic IR imaging detects both spatial and temporal variations of the emitted thermal radiation. Prior to image acquisition, a thermal excitation, such as cooling or heating, is applied to skin surface in dynamic IR imaging [8]. The phase after removal of thermal excitation is called thermal recovery process, during which IR images are acquired and analyzed. Dynamic imaging increases local temperature differences between healthy and diseased tissue, which yields a stronger signal essential in quantitative diagnostic applications. By analyzing thermal recovery of skin temperature, abnormalities such as malignancy of skin lesions can be examined, quantified and

potentially diagnosed (with appropriate calibration and clinical validation) [1-8]. The general advantage of dynamic measurement methods is that they exempt the subject from reaching a well-defined steady state, which can be very time consuming and challenging. For example, in the past, when static applications prevailed, the patient was required to spend one or more hours in a thermally conditioned exam room in order to fully acclimate (reach a steady state) to the environment prior to the measurement [24]. Reaching a true steady state may not always be possible and there will still exist individual variations between test subjects.

Due to the rapid revival of infrared imaging systems as well as the growing potential of dynamic IR imaging applications in medicine, infrared thermography is becoming an important quantitative imaging modality to assist medical diagnostics. However, quantitative imaging requires high accuracy – high sensitivity and high spatial resolution, and several factors hindered widespread use of infrared thermography in quantitative medical diagnostic applications. The prevailing conception in part of the community is that the color coded images generated by commercial, off-the-shelf, often low-cost imagers deliver accurate temperature data for diagnostic applications, and that all problems with thermographic measurements have been resolved. Unfortunately, this is not the case, and there are numerous challenges in the development of quantitative diagnostic applications that need to be resolved first. For example, the data shown in the image generated by the imager can carry a variation up to 2-4$^{o}$C, depending on surface shape, size and curvature, surface properties and ambient conditions. This discrepancy can be explained by the calibration method using data for a blackbody, a flat surface with the emissivity of 1 perpendicular to the camera axis during the calibration process. In

dynamic IR imaging, the challenge is to apply sufficient cooling to maximize thermal contrast between lesion and healthy tissue that can be accurately quantified with current IR imaging hardware, while the cooling time and temperature have to be controlled to minimize the discomfort to patient. However, the lack of systematic procedures to select cooling conditions in clinical sites thus hinders the wide spread applications of dynamic IR imaging. Moreover, during the acquisition of dynamic IR image sequences, the patients' involuntary movements (breathing or small involuntary movements of the body and limbs) will undermine the accurate temperature recording at any particular point on the skin, therefore influencing the validity and accuracy of the local temperature analysis and the associated diagnosis.

## 1.2 Organization of the thesis

In order to address the aforementioned problems that hinder the use of infrared imaging as a quantitative tool in medical diagnostics, in the thesis, several technical topics are investigated, and these topics are organized in the following chapters, as summarized below:

**Chapter 2** – Analysis and optimization of skin cooling for dynamic infrared imaging

To better understand the thermal behavior of skin tissue in dynamic infrared imaging, a computational bioheat model of the skin with multiple layers and a near-surface lesion is developed. With the aid of this model, various cooling methods and conditions suitable

for clinical applications of dynamic IR imaging are critically evaluated. The goal of this chapter is to find optimal cooling methods and parameters which are easy to apply in a clinical setting, leading to strong thermal contrasts while minimizing patient discomfort and measurement duration.

**Chapter 3 -** Motion tracking in infrared imaging for quantitative medical diagnostic applications

To achieve high-accuracy quantitative IR image analysis, in this chapter, a tracking approach using a template-based algorithm is proposed and investigated. The proposed tracking approach is capable of following the involuntary motion of the subject in the IR image sequence acquired in the clinical environment. To evaluate the tracking accuracy of the proposed method, the algorithm is tested experimentally using static and dynamic IR image sequences of a human subject with random motion.

**Chapter 4 -** Quantification of curvature-induced artifacts in infrared imaging

The key challenge of IR imaging in medical diagnostic applications involves accurate quantification of body surface temperatures. Temperature measurement errors and biased diagnostic results are often caused by artifacts induced by the curvature of imaged objects. In this chapter, an experiment-based analysis is conducted to address the artifacts, and the experimental results are compared with theoretical models proposed in the literature. An empirical formula for the correction of this artifact is developed based on the experimental results. The goal is to integrate the correction formula into the 3D IR thermal mapping methodology developed in Chapter 5.

**Chapter 5** -Three-dimensional quantitative thermal mapping of the human body

In this chapter, we introduce methodologies that generate an accurate 3D thermal map of the human body using the combination of Microsoft Kinect and a precise IR camera. Furthermore, we utilize the empirical formula described in Chapter 4 to compensate for curvature-induced artifacts in the reconstructed raw 3D thermal map. We evaluate the feasibility of 3D thermal mapping using the Kinect-IR camera system in a clinical setting. The accuracy of the correction formula to account for curvature induced artifacts developed in Chapter 4 is also validated.

**Chapter 6** – Clinical case studies of in-vivo IR imaging

With the aid of the motion tracking approach developed in Chapter 3, in this chapter we conducted quantitative analyses of in-vivo IR images acquired in clinical studies of melanoma and infantile hemangioma. In addition, some case-specific analytical approaches are also devised to quantify the thermal signatures of different skin lesions. The goal of this chapter is to gain technical insight into the performance of quantitative IR imaging in the clinical setting.

**Chapter 7-** Conclusions and discussion

This chapter summarizes the knowledge and conclusions gained from previous chapters, and the prospects of quantitative IR imaging in medical diagnostic applications are addressed.

# Chapter 2

# Analysis and optimization of skin cooling for quantitative dynamic infrared imaging of near-surface lesions

## 2.1 Overview

Melanoma incidence is increasing at one of the fastest rates for all cancers in the United States, with a current lifetime risk of 1 in 55 [25]. According to clinical reports, 1-year survival rates for patients with advanced melanoma range from 40% to 60% [26]. If melanoma is detected at an early stage, i.e. before the tumor has penetrated the epidermis, the 5-year survival rate is about 99%. However, for patients with advanced disease, the 5-year survival rate drops dramatically, to 15%[27]. Therefore early detection is critical to extend the lifespan of patients with more advanced disease. In order to enable early

detection and diagnosis and avoid unnecessary biopsies, it is essential to develop accurate, sensitive and objective quantitative diagnostic instruments.

The dramatic advances in IR imaging hardware, computers and image analysis techniques opened new avenues for quantitative IR imaging in a variety of medical and engineering applications. Over the past decade quantitative IR imaging has become a powerful and accurate tool in a variety of settings and has overcome many of the challenges of the past (most past IR imaging and diagnostic applications were qualitative). Active IR imaging involves introducing external forcing (also called thermostimulation), heating or cooling, to induce or enhance relevant thermal contrasts between the investigated lesion and healthy tissue. The general advantage of dynamic (active) measurement methods is that they exempt the subject from reaching a well-defined steady state, which can be very time consuming and challenging. For example, in the past, when static applications prevailed, the patient was required to spend one or more hours in a thermally conditioned exam room in order to fully acclimate (reach a steady state) to the environment prior to the measurement [24]. Reaching a true steady state may not always be possible and there will still exist individual variations between test subjects.

In the dynamic method the thermal response to an excitation, often applied as a step change in the thermal boundary conditions (heating or cooling), is measured. This is a much faster and more robust approach than the steady method. The dynamic method is well-established in numerous engineering applications, such as thermophysical property measurements. It also offers advantages in clinical applications, for which the duration of the measurement, patient comfort and the ease of use are critical. It has been demonstrated that thermostimulation by cooling can improve the thermal contrast

(defined as the temperature difference between the lesion and healthy skin) between healthy and cancerous tissue in the thermography of breast [28]. When the skin surface is imaged during cooling and thermal recovery following the removal of the cooling stress, the difference in the thermophysical properties of the lesion (when compared to healthy tissue) underneath the surface results in identifiable temperature contours during these transients. These surface temperature contours will differ from those present in steady state observed during passive IR imaging. Therefore the measurement process consists of three phases: (i) the initial phase when the skin is exposed to nominal ambient conditions, (ii) the cooling phase which is followed by (iii) the thermal recovery phase. The dynamic thermal response of the structure acquired using active IR imaging provides critical information which allows identifying the malignant lesion, as shown by Pirtini Cetingul and Herman [4, 6]. Since IR imaging (with proper calibration) yields quantitative data, the method holds the potential of allowing the staging of the disease.

To optimize diagnostic measurements for medical applications, computational modeling of the tissue response for different cooling (or heating) scenarios is used. It allows better understanding of the influence of different system parameters and predicting the responses to various thermal stimuli. The computational model accounts for the variations of thermophysical properties, layer thicknesses, metabolic heat generation, and blood perfusion for the different tissue layers. Several types of computational models of human tissue, based on the Pennes bioheat equation [29], have been proposed in the literature [2, 30-36]. A tissue layer is generally treated as a homogenous continuum with vascular network These models rely on a variety of assumptions to account for the effects of blood flow [2, 31-35]. By modeling

the tissue as porous matrix, Mahjoob and Vafai [37, 38] examined heat transport in biological media for biomedical applications, such as hyperthermia. In their model, prescribed heat flux is imposed on the cancerous tissue. In these studies, several important parameters influencing heat transport through the biological tissue were investigated, including volume fraction of vascular network space, depth of organ/tissue, imposed heat flux, metabolic heat generation, and core body temperature. For designing thermal management devices and small-scale biomedical applications which utilize porous channels, Mahjoob and Vafai [39, 40] analytically investigated the effects of geometrical configuration of channels on the heat transfer behavior.

In order to improve the effectiveness and sensitivity of active quantitative IR imaging for diagnostic purposes, in particular for the early diagnosis of melanoma, a thorough understanding and optimization of the cooling process and the subsequent thermal recovery phase is essential. The challenge is to apply sufficient cooling to maximize thermal contrast between lesion and healthy tissue that can be accurately quantified with current IR imaging hardware. At the same time the overcooling of the tissue, which would lead to extended thermal recovery periods, delayed appearance of thermal contrasts and long measurement times unacceptable in a clinical setting, has to be avoided. With competing effects and requirements that depend on a wide range of system parameters (thermal and metabolic inputs, geometrical considerations, thermophysical properties) this problem can mathematically be cast as an optimization problem in a multidimensional parameter space. In past studies the cooling method, temperature and duration were selected ad hoc, usually by trial and error. The goal of the chapter is to systematically examine this parameter space for a range of conditions and develop

practical recommendations regarding cooling procedures for clinical applications using a computational approach with experimental validation.

In this chapter a computational model of skin tissue with a near-surface lesion is introduced first, and with the aid of this model various cooling methods and conditions suitable for clinical application are considered, compared and critically evaluated. Our goal is to find optimal cooling methods and parameters which are easy to apply in a clinical setting and provide strong thermal contrasts while minimizing patient discomfort and measurement duration.

Since the primary aim of the study is the detection of early stages of melanoma (before the cancer enters the capillary bed, which is nominally 6 mm below the surface), the cooling conditions discussed in this chapter focus on near-surface lesions. In this study near-surface lesions are defined as lesions characterized by less than 4 mm invasion. As illustrated in Figs. 2.1(a), (b) and (c), skin cancer lesions, port wine stains and some burn lesions would fall into this category. Deep lesions, such as breast cancer (Fig. 2.1(d)) or deep tissue injuries [41], such as pressure ulcers (Fig. 2.1(e)), would require a separate analysis to understand and optimize the cooling conditions. Even though the physical situation considered in the chapter is biomedical, the general considerations and conclusions drawn are of interest to other engineering systems described by similar sets of equations (for example detection of failure in composite materials) and similar geometries.

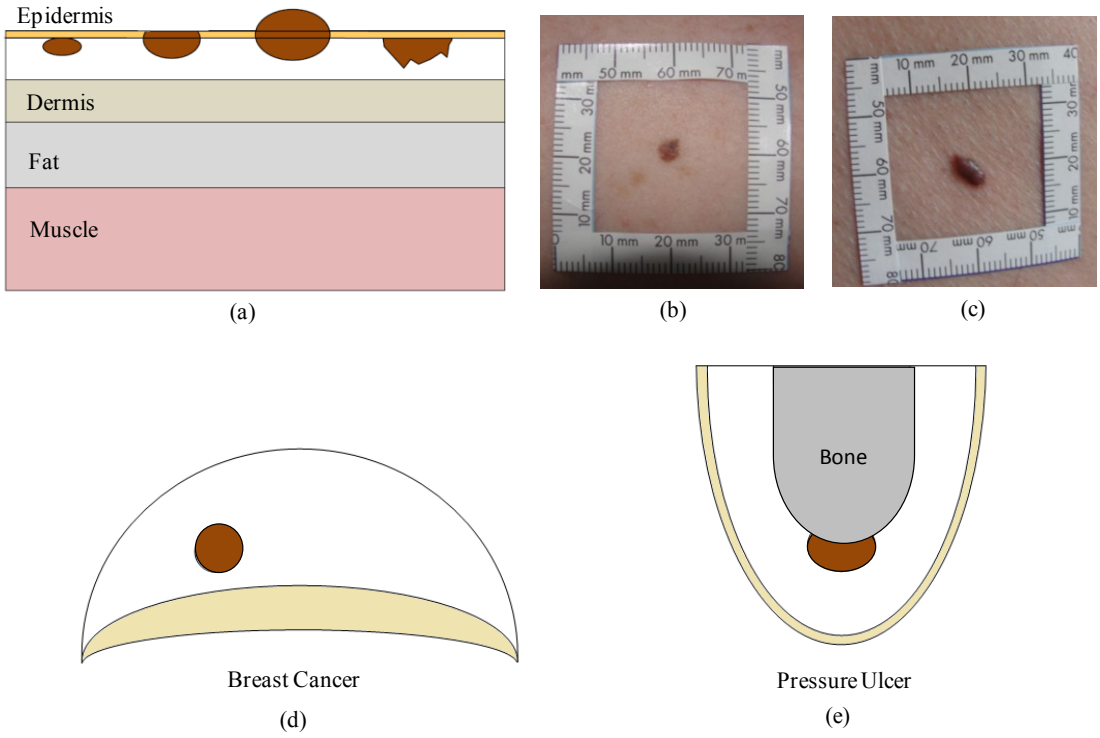


**Figure 2.1** (a) Schematic of near-surface skin lesions of various invasion levels: (b) photo of a melanoma lesion flush with the skin surface and (c) lesion with elevation above the skin surface. Schematics of deep lesions: (d) breast cancer and (e) pressure ulcer.

## 2.2 Literature review for skin cooling in clinical application

Various skin cooling approaches have become an active research area of clinical interest since the introduction of thermally mediated therapeutic procedures. Cooling burn injuries with poured or sprayed on water at around 20 °C can improve the initial treatment of extensive burns [42]. Conductive, convective, and evaporative methods have

been used by clinicians to cool down the body to treat fever or hyperthermia [43]. Wyndham et al. [44] compared the cooling rates of different cooling methods, such as the spraying of water, the blowing of air or immersion in water, for the management of hyperpyrexia. In the past, contact skin cooling using ice or chilled gels was used for local anesthesia in dermatologic surgery [45] and spray coolants are currently being used for local anesthesia and cryosurgery [46]. Chilled water or gas flow for skin cooling are applied in surgical and therapeutic procedures [47-51]. Since the applications and goals of cooling vary broadly, the mathematical models that capture the effects relevant for a particular application will vary as well.

Di Carlo et al. [52] designed a thermostimulation method for the detection of melanoma using active IR imaging. Buzug et al. [53] used cold gel packs as the cooling medium to induce the temperature difference on the skin surface in the imaging of basal cell carcinoma. Santa Cruz et al. [54] cooled the leg of the patient by immersion into a pool of cold water for thermographic imaging to detect the recurrence of melanoma after surgery. Pirtini Cetingul and Herman [4, 6, 55] cooled the area of the skin containing the lesion and surrounding tissue with a gel pack or by blowing air from a vortex tube in a patient study conducted by the Heat Transfer Lab of the Johns Hopkins University. This application is the immediate motivation for the study reported in this chapter.

## 2.3 Theory and method

### 2.3.1 Physical situation and mathematical model

Melanoma lesions and many of the lesions of interest in clinical diagnostics are of irregular shape, therefore a representative idealized elliptical cross section of the lesion is considered in this study without loss of generality [2]. For a more accurate thermal model of a particular lesion, the three dimensional geometry information has to be included into the computational model. In our study, human tissue is modeled as a 2D semi-infinite domain representative of the cross section of the tissue and lesion in the Cartesian coordinate system. Five main layers are considered in the model, the epidermis, papillary dermis, reticular dermis, fat and muscle (viewed from the surface). As shown in Fig. 2.2, each layer $n$ is modeled as a homogeneous medium of finite thickness $d_n$ in the $y$ direction and characterized by its unique thermophysical properties, summarized in Table 2.1 [2]. The lesion is modeled as an elliptical domain with major axis $W$ and minor axis $P$, as illustrated in Fig. 2.2(a) and (b).

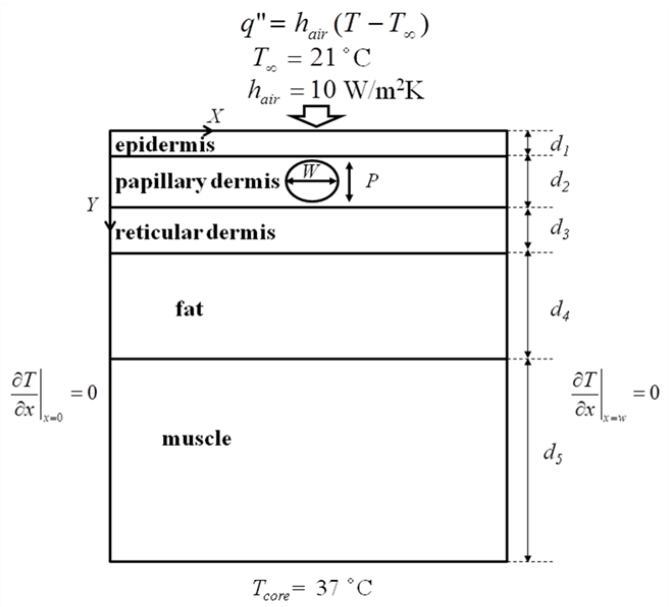


(a)

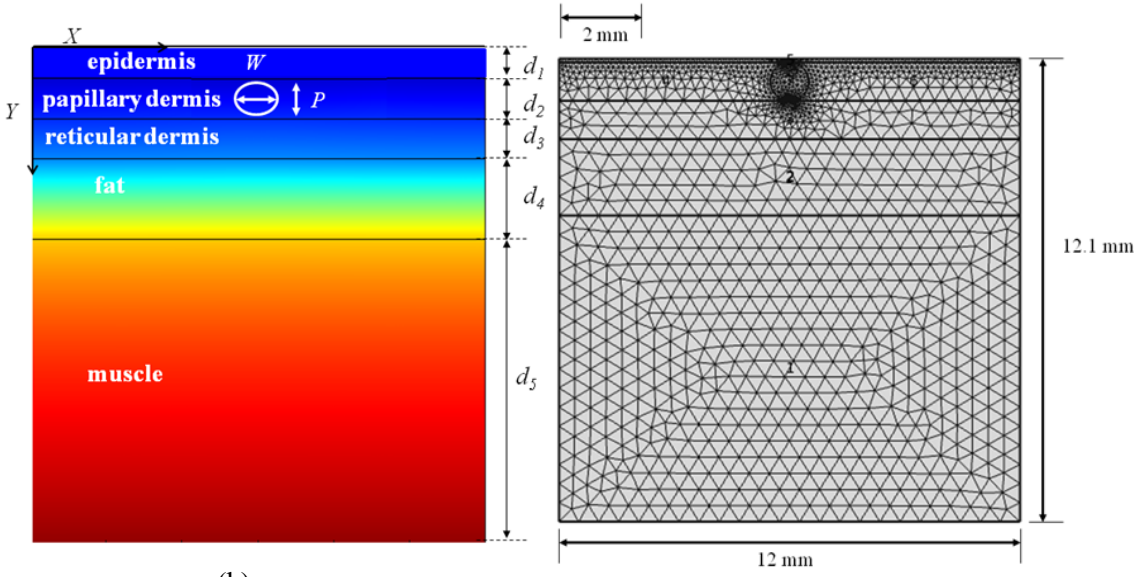


(b) (c)

**Figure 2.2** (a) Schematic of the tissue layers and the lesion in the computational domain with boundary conditions for the steady state situation, (b) computed temperature distributions for the steady state situation and (c) the computational mesh.

**Table 2.1** The properties of tissue layers (based on [2]).

| | $d$ (mm) | $C$ (J/kg·K) | $k$ (W/m·K) | $\rho$ (kg/m$^3$) | $w_b$ (m$^3$/s·m$^3$) | $Q$ (W/m$^3$) |
|---|---|---|---|---|---|---|
| Epidermis | 0.1 | 3589 | 0.235 | 1200 | 0 | 0 |
| Papillary dermis | 1 | 3300 | 0.445 | 1200 | 0.00018 | 368.1 |
| Reticular dermis | 1 | 3300 | 0.445 | 1200 | 0.00126 | 368.1 |
| Fat | 2 | 2674 | 0.185 | 1000 | 0.00008 | 368.3 |
| Muscle | 8 | 3800 | 0.51 | 1085 | 0.0027 | 684.2 |
| Lesion | $W = P = 1$ | 3852 | 0.558 | 1030 | 0.0063 | 3680 |

Heat transfer processes in the human skin and underlying tissue can be modeled using the bioheat equation proposed by Pennes (1948) [29] , which is the transient heat conduction equation of the form

$$\rho_n C_n \frac{\partial T_n}{\partial t} = k_n \nabla^2 T_n + \rho_b C_b w_{b,n} (T_b - T_n) + Q_n, \qquad (2.1)$$

where $n$ = 1,2, … 5 denote the tissue layers considered in the model, epidermis, papillary dermis, reticular dermis, muscle and fat, respectively. $\rho_n$, $C_n$, $k_n$, $T_n$ and $Q_n$ represent the parameters that describe layer $n$ and denote the tissue density, specific heat of the tissue, thermal conductivity, local tissue temperature and the metabolic heat generation rate, respectively. $\rho_b$, $C_b$, $w_b$, $T_b$ denote the properties of blood, density, specific heat, blood perfusion rate and temperature, respectively. Eq. (2.1) is solved by imposing appropriate boundary conditions at the skin surface, continuity conditions for the temperature and heat flux at each interface between skin layers, the core body temperature condition at the bottom of the muscle layer and zero heat flux at the lateral boundaries.

For $t < 0$ we assume that steady state ambient conditions exist within the tissue. In steady state, the top skin surface at $y = 0$ is exposed to ambient natural convective boundary conditions specified as

$$q'' = h(T(y = 0, t < 0) - T_\infty)\,. \tag{2.2}$$

The convection heat transfer coefficient $h$ in Eq. (2.2) is assumed to be $h = 10$ W/m$^2$ K (a typical value for natural convection) and the ambient temperature is $T_\infty = 21$ °C. The same natural convective boundary condition is also prescribed at the skin surface during the thermal recovery phase following the removal of the cooling stress. In our simulation, the surface-to-ambient radiation associated with skin emissivity is neglected due to its limited effect. A detailed discussion of the influence of radiation is presented in Section 2.4.4.

The temperature continuity and conservation of heat flux conditions at the interface between skin layers can be written as

$$T_n(y = y_n, t) = T_{n+1}(y = y_n, t) \quad \text{and}$$

$$k_n \left.\frac{\partial T_n}{\partial y}\right|_{y=y_n} = k_{n+1} \left.\frac{\partial T_{n+1}}{\partial y}\right|_{y=y_n}, \quad n = 1, \ldots, 4. \tag{2.3}$$

In Eq. (2.3) $y_n$ denotes the $y$ location of the bottom boundary of the $n$th tissue layer of thickness $d_n$, $y_n = y_{n-1} + d_n$. The sixth domain in this model is the lesion, and the temperature distribution within the lesion is also described by the Pennes bioheat equation [29], Eq. (2.1). Similar interfacial conditions hold at the interface of the lesion and the healthy tissue as those between the skin layers, described by Eq. (2.3). The bottom boundary of the muscle layer can be assumed to be at core body temperature $T_{c,b}$ at all times, which is also the boundary condition commonly prescribed in porous media models [37, 38] for heat transfer through biological media. The core body temperature in this study is

$$T(x, y_5, t) = T_{c,b} = 37\ ℃\,. \tag{2.4}$$

In this study we consider small lesions (which are of particular interest for the early diagnosis of melanoma, for example) and a larger area of healthy tissue surrounding the lesion. We assume zero heat flux from both sides of the computational domain, at $x = 0$ and $x = w$, at a sufficient distance from the heat-generating lesion. This suggests that the temperature at the lateral boundary (as well as the bottom boundary) is unaffected by the presence of the lesion in steady state conditions and during thermal recovery. Therefore the lateral boundary condition takes the form

$$\left.\frac{\partial T_n}{\partial x}\right|_{x=0,w} = 0. \tag{2.5}$$

Based on published data from the literature [2, 56-59], the dimensions used in our computations and the thermophysical properties of each skin layer are listed in Table 2.1. In this chapter typical nominal values introduced by [2] were selected for the calculations. While individual and local variations in these properties can exist, a previous sensitivity analysis carried out by Pirtini Cetingul and Herman [2] concluded that the impact of these variations on the surface temperature is small. Therefore the general trends of the thermal responses relevant for this study remain, with property variations resulting in small variations in absolute values. In general, the lesion is three dimensional, however the shape has a small impact on the surface temperature response. The dominant effect will be that of the overall volume of the lesion, as shown in [2]. For a more accurate analysis of a particular situation actual measured data should be used. Since the lesions of importance for clinical practice are relatively small and confined to the top tissue layers (near-surface lesions), the impact of small variations of dimensions and the properties of the deeper tissue layers on the thermal response is relatively small too. We also assume that, because of the relatively short cooling times and small

temperature differences used in thermostimulation, the thermophysical properties remain constant during the 1–2 min interval needed for the imaging process.

In addition to the values summarized in Table 2.1, the properties of blood are prescribed as follows: density of blood $\rho_b = 1060$ kg/m$^3$ [60], specific heat $C_b = 3770$ J/kg K [59], and blood temperature $T_b = 37$ °C [59]. Regarding the variation range of the thermophysical properties discussed in the literature [56-59], prior studies [2] show that the surface temperatures are most sensitive to the variations in the blood perfusion rate and skin layer thicknesses. The studies of Song et al. [61] suggest that a cancerous lesion is characterized by increased metabolic activity and blood flow, and a highly vascularized skin tumor may cause increase of local skin temperature [62]. Thus, in the tissue model introduced in this chapter, the domain of the lesion is represented as a region of increased metabolic heat generation and blood perfusion. As shown in Table 2.1, based on prior studies [61, 63, 64], blood perfusion is considered to be five times larger and the metabolic heat generation is ten times larger in the region of the lesion than in normal surrounding tissue. Since these values were not measured specifically for melanoma lesions, in our analysis we consider these low values as the worst case scenario for IR imaging as well as higher values which yield good agreement with our experimental measurements.

We used the commercial software COMSOL Multiphysics v.4.0 to find the numerical solution for our model described by Eqs. (2.1)–(2.5) with the dimensions and property values indicated in Table 2.1. The heat transfer module of COMSOL 4.0 was used to solve for the steady-state spatial temperature distribution first (Fig. 2.2(b)), and this solution serves as the initial condition for the investigation of the time-dependent

effects of various cooling methods. The software uses the finite element method to solve the bioheat transfer equation for the five coupled tissue layers and the lesion. The computational domain is 12 mm wide and 12.1 mm deep, with its dimensions selected to satisfy the conditions described by Eq. (2.5). Free triangular elements were used in the mesh as shown in Fig. 2.2(c). Since the temperature of skin surface is of particular interest for IR imaging, we set the maximum element size to be 0.15 mm (finest mesh) in the top layer (epidermis), and to 0.53 mm in other layers. To verify the convergence of the solution with respect to the mesh size, the maximum element size was further refined to 0.02 mm for the epidermis and to 0.15 mm for other layers. It was found that there was less than 1% difference in the solutions before and after refining the mesh size.

To validate the numerical model with respect to the existing analytical model for biological media [38], we divided our tissue model into two main layers, lesion and muscle, with thicknesses of 4.1 mm and 8 mm, respectively. Based on the thermophysical properties of lesion and muscle and the boundary conditions described in Section 2.3.1, the steady-state temperature in the skin layers was computed and compared with results reported in [38]. For the analytical model [38] we adopted the simplified solution for uniform core temperature of 37 °C and steady-state natural convection described by Eq. (2.2) was imposed as the uniform heat flux at the body surface. According to the analysis presented in [38], the parameters of the biological tissue matrix $K$, $\xi_b$, and $\xi_t$, , were taken to be 0.111, 0.111, and 1, respectively, in the validation procedure. The temperature distribution through the two layers, predicted by our numerical model, was then compared with the analytical solution developed in [38]. Good agreement between the numerical and analytical predictions was observed, with the largest temperature

differences being less than 0.071 °C. The agreement between data obtained using the two modeling approaches therefore validates our computational model.

### 2.3.2 Thermal boundary conditions for the selected cooling methods

A diversity of methods has been applied to achieve skin cooling in clinical applications. The clinical diagnostic application considered in this study requires cooling methods that are easy and inexpensive to apply, easily reproducible and cause little discomfort to the patient. We selected three cooling methods for our analysis, (i) constant temperature cooling (accomplished by applying melting ice in a pouch that can also be approximated with a gel pack), to be referred to as Case C1, (ii) cooling with a cotton patch soaked in cold water, Case C2, and (iii) convective cooling by blowing cold air onto the skin or immersion into a liquid, Case C3. During the cooling phase, the thermal boundary condition at skin surface depends on the cooling method applied. The cooling method and temperature will also affect the required or optimal duration of cooling and the thermal contrast between the lesion and healthy tissue.

#### 2.3.2.1 Constant temperature cooling, Case C1

Constant temperature cooling is an idealized case of contact cooling, for which the temperature of cooling medium applied to the skin surface remains constant during the entire cooling phase. In practice this condition is challenging to achieve, and can be approximated by a phase change (melting) process, a very high (infinite) heat capacity

cooling patch, or a process with very high (infinite) heat transfer coefficient. This type of cooling is modeled by prescribing a constant cooling temperature $T_c$ at the skin surface at $y = 0$ for the duration of cooling $t_c$ as

$$T(x, y = 0, t) = T_c \ , \quad 0 \leq t \leq \ t_c \, . \tag{2.6}$$

### 2.3.2.2 Cooling with a cotton patch soaked in water, Case C2

The second cooling method considered in this study involves applying a water-soaked cotton patch on the skin surface, which is a commonly used clinical procedure. Since the patch will mainly consist of water, we can model the patch as a 2 mm thick water layer in direct and ideal contact with the skin surface. In the computational model this layer of water will be represented by a sixth parallel layer (domain 7) above the tissue layers in Fig. 2.2, and heat transfer in this domain is modeled by the transient heat diffusion equation of the form

$$\rho_w C_w \frac{\partial T_w}{\partial t} = k_w \nabla^2 T_w \ , \quad 0 \leq t \leq \ t_c \ , \tag{2.7}$$

where the water properties are $k_w = 0.6$ W/m K, $\rho_w = 998$ kg/m$^3$, $C_w = 4186$ J/kg K. During the cooling phase, heat flux conservation and temperature continuity are prescribed between the water layer and the skin surface at $y = 0$ as

$$T_w(y = 0, t) = T_1(y = 0, t) \ \text{and}$$

$$k_w \frac{\partial T_w}{\partial y}\bigg|_{y=0} = k_1 \frac{\partial T_1}{\partial y}\bigg|_{y=0} \, . \tag{2.8}$$

The cooling temperature for Case C2 is defined as the initial temperature of this water layer at $t = 0$. In addition, to account for the heat loss $q''$ between the soaked cotton

and the environment at the surface of the cotton exposed to ambient air, the convective thermal boundary condition (with a convective heat transfer coefficient of $h$ = 10 W/m K, and $T_\infty$ = 21 °C) is prescribed at the top of water layer as

$$q" = h(T(y = -2\ mm,\ 0 \le t \le\ t_c) - T_\infty)\,. \tag{2.9}$$

#### 2.3.2.3 Convective cooling, Case C3

The third cooling method considered in this study is convective cooling, accomplished by directing a jet of cold air onto the skin surface or immersion of the area into a stagnant or circulating liquid. To achieve higher values of the heat transfer coefficient $h$, air can be replaced by water as the coolant (cooling by immersion into water). Mathematically the heat flux $q''$ due to air convection at $y = 0$ with a heat transfer coefficient $h$ and ambient temperature $T_\infty$ at the skin surface is prescribed as

$$q" = h(T(y = 0,\ 0 \le t \le\ t_c) - T_\infty)\,. \tag{2.10}$$

To analyze the impact of air cooling, the convection heat transfer coefficient $h$ is varied in the range of 50–1000 W/m$^2$ K in this study. The ambient temperature $T_\infty$ was varied in the range of 4 °C–20 °C. For Case C3, the ambient air temperature is defined as the cooling temperature.

### 2.3.3 Cooling penetration depth

In order to quantify the extent of tissue cooling during the cooling phase, the concept of the cooling penetration depth $D(t)$ is introduced, defined as

$$D(t) = y \ \text{ for which } \ \frac{T_{cp}(y,t)}{T_{ss}(y,t<0)} = 0.99\ , \tag{2.11}$$

where $T_{ss}(y)$ is the temperature distribution along a vertical line across the tissue in steady state (at the central location of the lesion, $x = 6$ mm), and $T_{cp}(y,t)$ the temperature distribution along the same line at time $t$ during the cooling phase. The duration of cooling $t_c$ is varied in this study to optimize the cooling conditions. The concept of the cooling penetration depth is illustrated in Fig. 2.3, by comparing the steady state temperature profile $T_{ss}$ with two profiles $T_{cp}(t_1)$ and $T_{cp}(t_2)$, computed at times $t_1$ and $t_2$, $t_1 < t_2 < t_c$, during the cooling phase, $0 < t < t_c$. As shown Fig. 2.3, the longer the cooling is applied, the deeper the tissue will be cooled, therefore the cooling penetration depth $D(t)$ increases with the duration of the cooling. The location with tissue temperature corresponding to 99% of the steady state temperature, is defined as the cooling penetration depth $D(t)$. These locations are displayed as full circles in Fig. 2.3 for the temperature profiles $D(t_1)$ and $D(t_2)$ at times $t_1$ and $t_2$, and they match the points where the steady state profile merges with the cooling phase profile. We can interpret $D(t)$ as the boundary of tissue region being cooled, or the depth below which the tissue is still at steady state temperature (unaffected by the cooling). The cooling penetration depth is a parameter that is helpful when quantitatively comparing the impact of the cooling methods investigated in this study.

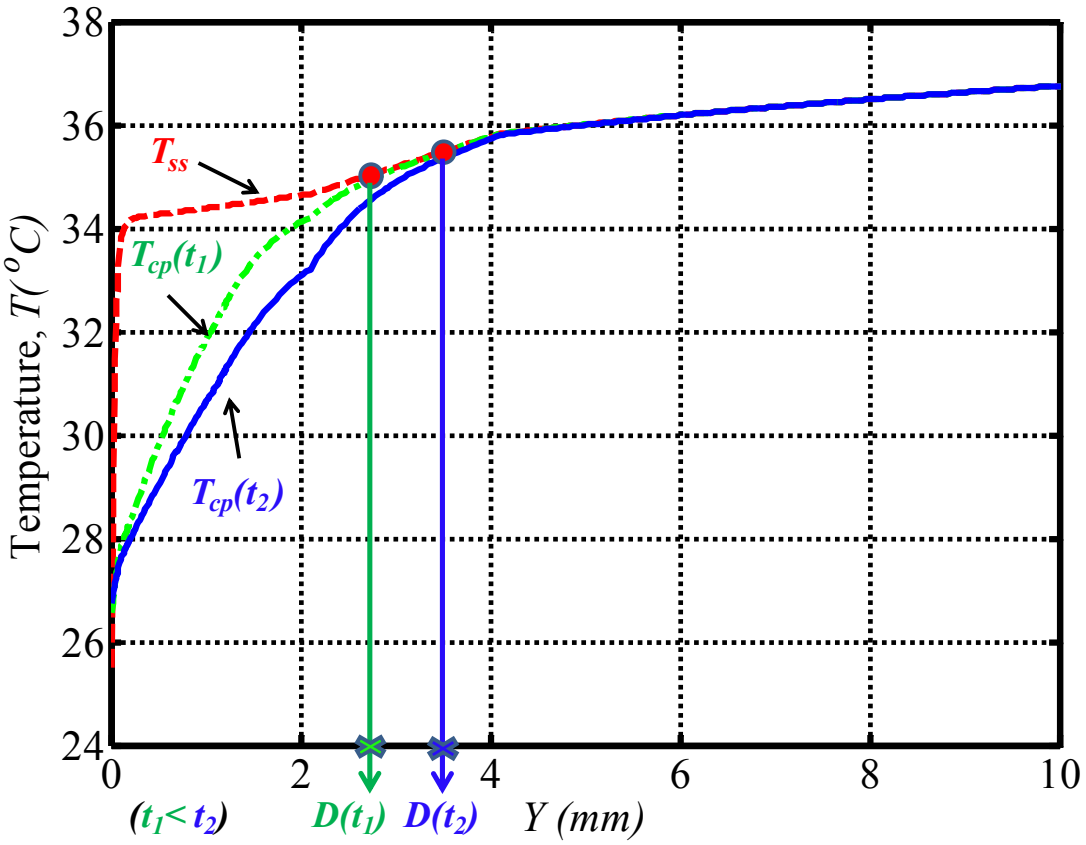


**Figure 2.3** Concept of the cooling penetration depth $D(t)$: comparison of the steady state temperature profile $T_{ss}$ and the temperature profiles at times $t_1$ and $t_2$, $T_{cp}(t_1)$ and $T_{cp}(t_2)$.

## 2.3.4 Thermal contrast during the thermal recovery phase

The goal of the cooling phase in the clinical diagnostic application that motivated this study is to cool down the skin surface sufficiently to enhance the temperature differences between healthy and diseased tissue quickly and without causing discomfort to the patient. Therefore, to evaluate the performance of various cooling methods, the temperature difference between lesion and surrounding tissue during the recovery phase is analyzed. This temperature difference is directly related to the thermal contrast visualized and measured in the thermographic images. As shown in Fig. 2.4, the temperature

difference $\Delta T(t)$ at the skin surface, between a point on the surface above the lesion $T_{lesion}(t)$ and the healthy tissue 4 mm away from the lesion center $T_{sur}(t)$, is computed in this study during the thermal recovery phase.

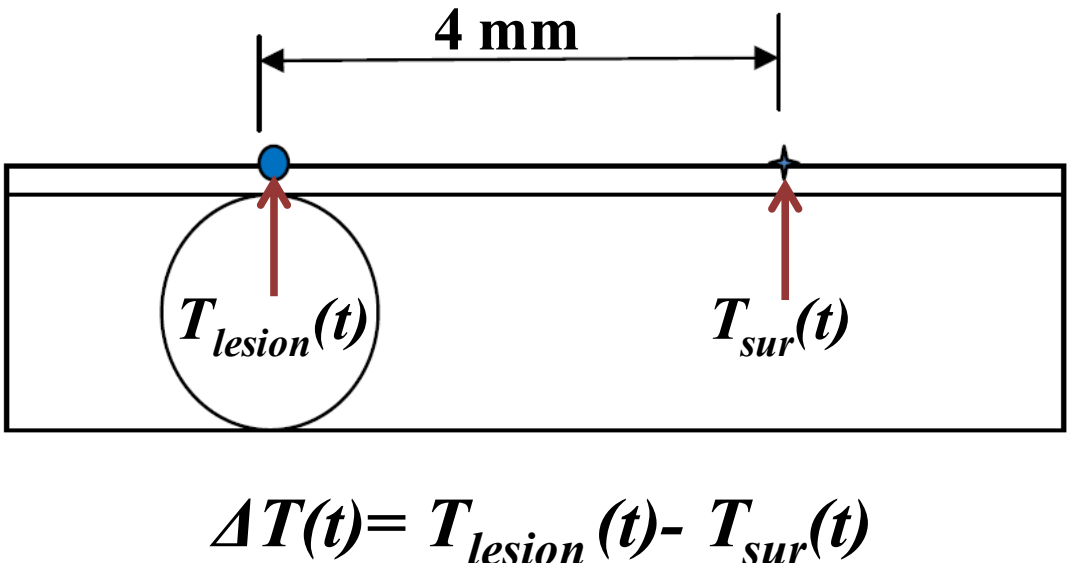


**Figure 2.4** Thermal contrast $\Delta T(t)$ as the difference between the surface temperature above the lesion center $T_{lesion}(t)$ and the surrounding tissue $T_{sur}(t)$ during the thermal recovery phase.

## 2.4 Results

In this section we discuss the results for cooling cases C1, C2 and C3, by comparing the thermal penetration depth during the cooling phase for three cooling temperatures $T_c$ = 4 °C, 12 °C and 20 °C, and the thermal contrast as a function of time during thermal recovery. Results are presented in the form of diagrams as well as numerical data organized into tables. For convective cooling, four convective heat

transfer coefficients $h$, representative of forced and natural convection using air or liquid, are considered.

### 2.4.1 Cooling penetration depth: cooling phase

Fig. 2.5 shows the cooling penetration depth $D(t)$ during the cooling phase for constant temperature cooling, Case C1, for a time interval of 30 s. Only the first 30 s of the cooling phase are displayed in the diagrams in this section, since this time interval is sufficiently long for the diagnostic applications considered in our study. The results indicate that by 30 s the cooling effect has reached the entire domain (depth) of the lesion. The five tissue layers considered are highlighted in different colors in Fig. 2.5 and the subsequent diagrams. Three representative cooling temperatures relevant for clinical applications, 4 °C, 12 °C, and 20 °C were considered, and therefore three corresponding curves are plotted in Fig. 2.5. It can be observed that, within approximately 20 s from the onset of cooling, the cooling effect penetrates to the depth of 4 mm below skin surface (depth of the fat layer) for all three cooling temperatures. During the first 5 s of the cooling phase, the cooling penetration rate and depth are very similar for the three temperatures. The impact of the cooling temperature becomes more apparent for times 5 s and longer after the onset of cooling. At the same time instant, the cooling rate and the cooling penetration depth increase with decreasing cooling temperature.

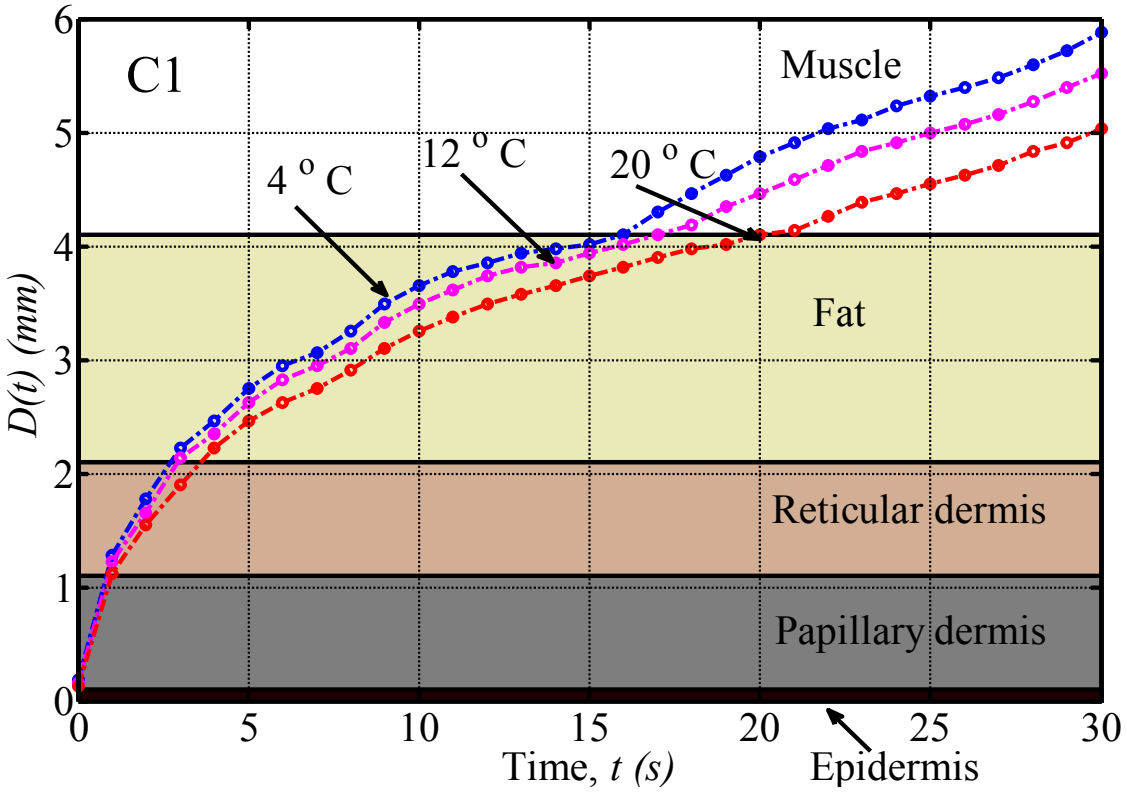


**Figure 2.5** Cooling penetration depth $D(t)$ as a function of time for Case C1 for constant temperature cooling: cooling temperatures $T_c$ = 4 °C, 12 °C and 20 °C.

The cooling penetration depth curves when applying soaked cotton cooling, Case C2, are displayed in Fig. 2.6 for the three cooling temperatures (initial water temperatures). After applying the soaked cotton to the skin surface, the temperature of the cotton patch will increase, since it is being warmed by the skin and the ambient (the heat capacity of the patch is finite, contrasted to the infinite heat capacity of Case C1). Therefore, the rate of cooling penetration for C2 is less than for C1. For cooling temperatures of 4 °C, 12 °C, and 20 °C, it takes around 19 s, 22 s, and 27 s, respectively, for the cooling effect to penetrate through the depth of the fat layer (4 mm).

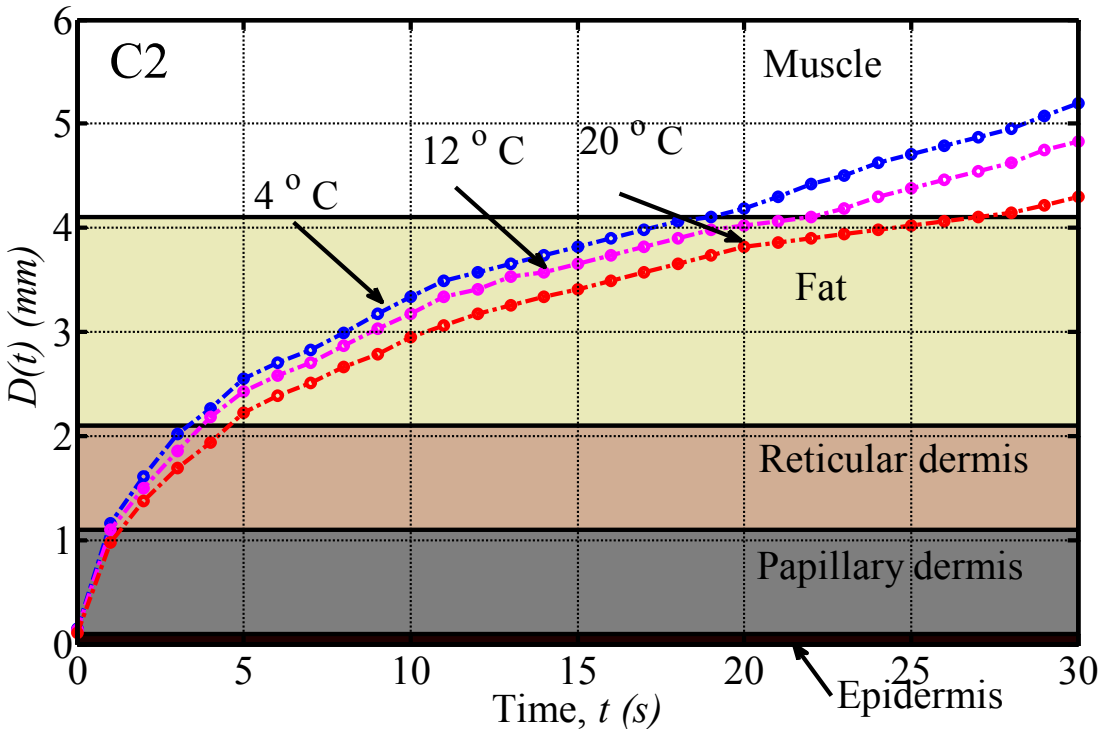


**Figure 2.6** Cooling penetration depth $D(t)$ as a function of time for Case C2 for soaked cotton cooling: cooling temperatures $T_c = 4\ ^\circ$ C, $12\ ^\circ$ C and $20\ ^\circ$ C.

Cooling penetration depth results for convective cooling (air or water cooling), Case C3, for a range of convection heat transfer coefficients $h$ are shown in Fig. 2.7. For the heat transfer coefficient $h = 50$ W/m$^2$ K, which is a typical value for forced convection in air, we observe that it takes over 30 s for the cooling effect to reach the depth of 4 mm for all three cooling temperatures used. As $h$ increases to $h = 100$ W/m$^2$ K (Fig. 2.7(b)), a value corresponding to higher air speeds, $D(t)$ approaches the depth of 4 mm within 30 s for the cooling temperatures $T_c = 4$ °C and 12 °C. For $T_c = 20$ °C it takes longer than 30 s for the cooling effect to reach the depth of 4 mm. These results suggest that air cooling will be most suitable for skin lesions with the depth less than 2 mm, if the cooling time is to be kept under 30 s. Since early detection of skin cancer is of particular diagnostic interest, this is often going to be the case in clinical applications,

whereas advanced cases are easier to diagnose using conventional methods. For deeper lesions, cooling times longer than 30 s and lower air temperatures ($T_c = 4$ °C) may be necessary.

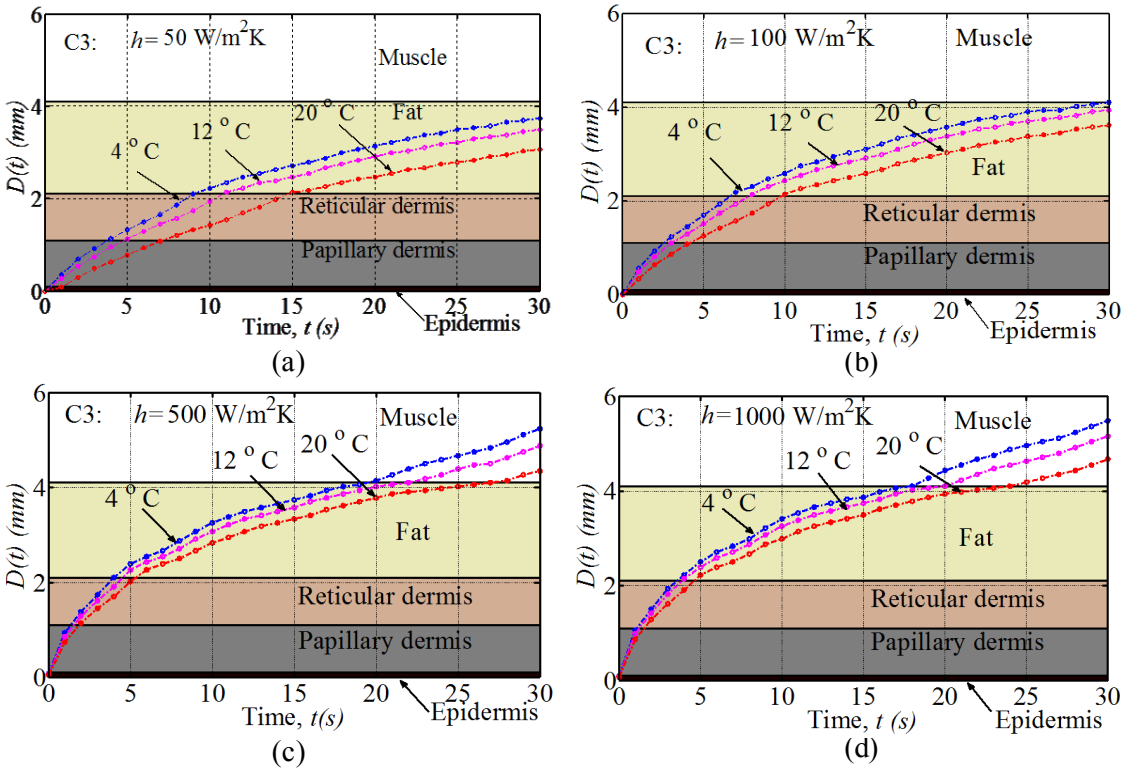


**Figure 2.7** Cooling penetration depth $D(t)$ as a function of time for Case C3 for convection cooling (air or liquid) with convection heat transfer coefficients $h$= (a) 50 W/m$^2$ K, (b) 100 W/m$^2$ K, (c) 500 W/m$^2$ K and (d) 1000 W/m$^2$ K and cooling temperatures $T_c = 4$ °C, 12 °C, and 20 °C.

However, as $h$ increases to 500 W/m$^2$ K and 1000 W/m$^2$ K (Fig. 2.7(c) and (d), Case C3), which are the values characteristic of liquid (water) cooling, the thermal penetration depths reach the magnitudes similar to the cases with constant temperature cooling (Case C1) and soaked cotton cooling (Case C2). The results in Fig. 2.7(c) and (d) show that for these higher values of $h$ the cooling effect can penetrate through the depth of fat layer within 30 s. These heat transfer coefficients and cooling temperatures can be achieved by immersing the skin into a pool of stagnant or flowing water. This cooling method is easy to apply in a clinical setting, when the lesion is located on a limb, for example.

## 2.4.2 Thermal contrasts during thermal recovery

In this section we discuss the results for the thermal contrast $\Delta T(t)$ during thermal recovery for the three cooling methods considered in this study, with the cooling temperature being $T_c = 20$ °C for all three cases.

### 2.4.2.1 Thermal contrasts, Case C1

The thermal contrast between the lesion and healthy tissue at the skin surface $\Delta T(t)$, present following the removal of constant temperature cooling (Case C1), is plotted in Fig. 2.8 as a function of recovery time $t$. The duration of cooling $t_c$ is the parameter for the family of curves shown in Fig. 2.8, with the values ranging from 5 s to 120 s. Two distinctly different responses (behavior types) can be observed during thermal recovery: one for short cooling times (0–20 s), and another for longer cooling times (>20 s). For

short cooling times, the temperature difference is the largest immediately after the removal of the cooling, and it rapidly decreases with the recovery time (type one maximum). Therefore the strongest signal will be available between 0 s and 5 s into the thermal recovery. For longer cooling times, the thermal contrast initially increases after the removal of cooling, and the maximum contrast between the lesion and healthy tissue appears at around 40 s into thermal recovery (type two maximum). This region of maximum contrast is relatively broad compared to the narrow peak developing after the application of short cooling times. After this maximum, the temperature difference $\Delta T(t)$ gradually and monotonically decreases with time.

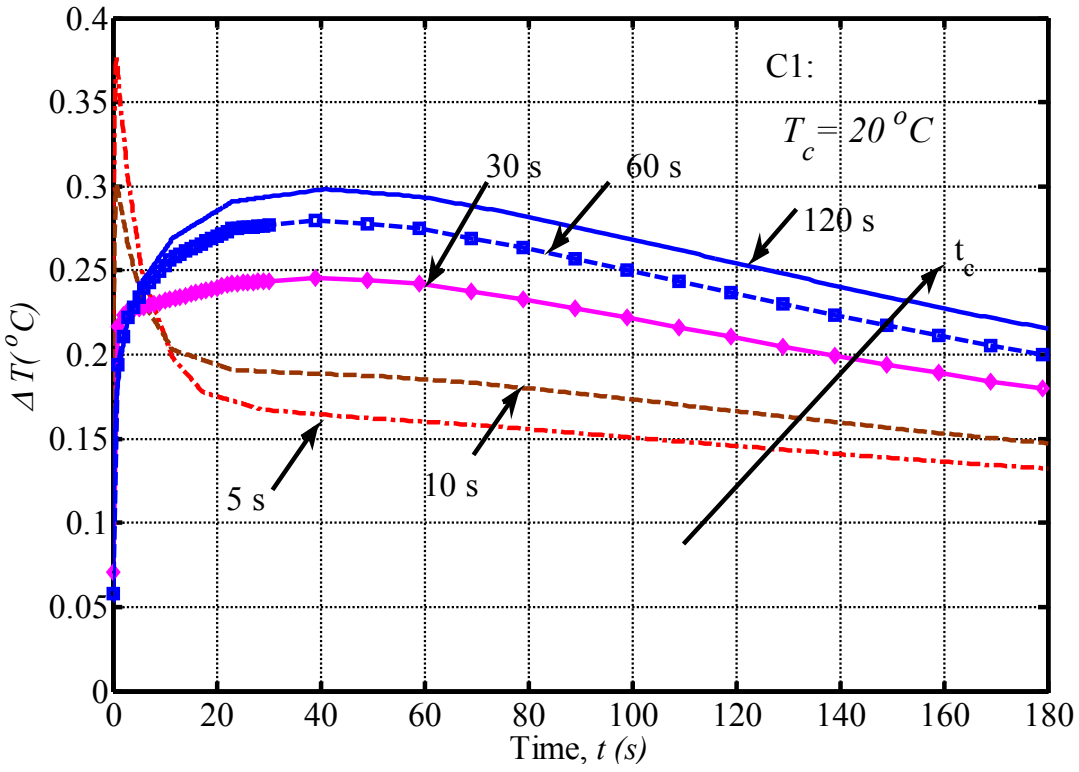


**Figure 2.8** Thermal contrast $\Delta T(t)$ as a function of time with cooling time $t_c$ as parameter (values of $t_c$ are in the range of 5–120 s) for constant temperature cooling (Case C1) with $T_c = 20$ °C.

These results are essential for the design of the measurement system for clinical diagnostic applications. They indicate that, depending on the cooling time, the maximum signal can be detected either immediately after the removal of cooling (0–5 s) or around 40 s into the thermal recovery. The duration of the infrared image sequence (movie) acquisition during thermal recovery is determined by these times. The results suggest that for small lesions imaging times up to 90 s will be sufficient, which is acceptable in clinical practice. The number of image frames to be analyzed in the image processing phase is also reasonable and it depends on the sampling rate. The cooling times as well as imaging times can be shorter for smaller and more superficial lesions.

The differences between the two types of responses during thermal recovery can be attributed to the differences between the thermophysical properties of the lesion and healthy tissue. Because of the increased heat generation within the lesion, the surrounding healthy tissue will cool down more rapidly than the lesion during the first 15 s of cooling. During this short time, the temperature decrease in the lesion is much smaller, leading to high thermal contrasts very early during the recovery. After 15 s, the heating within the lesion is overpowered by the external cooling, leading to reduced thermal contrasts. The 40 s recovery time is needed for the lesion heating effects to compensate for the external cooling, leading again to high thermal contrasts. The magnitude of the thermal contrasts for the cooling parameters considered is in the range of 0.3−0.4 °C, and these values can be easily detected by modern IR cameras. Ideally, in clinical practice, shorter cooling times are desired. However, this implies that visual access to the cooled area has to be enabled immediately after the removal of the cooling stress (the source of cooling has to

be removed quickly and imaging has to start immediately, leaving no time for focusing and adjustments of the optics).

Table 2.2 summarizes key results: the cooling penetration depth $D(t_{\max})$, the time $t_{\max}$ corresponding to $\Delta T_{\max}$, and the value of the maximum temperature difference $\Delta T_{\max}$ for various cooling times $t_c$. From the data, we can infer that when the cooling time is shorter than 20 s, the maximum temperature difference will occur within a few seconds after the cooling stress is removed, and the magnitude of the maximum decreases with increasing cooling time. However, when the cooling time is longer than 25 s, the maximum will occur approximately 40 s into the thermal recovery phase, and the magnitude of $\Delta T_{\max}$ increases with increasing cooling time $t_c$. The thermal penetration depth $D(t_{\max})$ increases from 2.5 mm for 5 s of cooling to 7.4 mm for 120 s of cooling. Therefore, cooling and measurement times can be adjusted to match the lesion depth: as expected, shorter cooling time is appropriate for superficial lesions and longer cooling time for deeper lesions.

**Table 2.2** Data for constant temperature cooling, Case C1: cooling penetration depth $D(t_{\max})$, time of maximum thermal contrast $t_{\max}$ and the corresponding $\Delta T_{\max}$ for various cooling durations $t_c$.

| Cooling Time $t_c$ (s) | Cooling Penetration Depth $D(t_{max})$ (mm) | Timing of Max. $\triangle T(t)$ $t_{max}$ (s) | Max. $\triangle T(t)$ $\triangle T_{max}$(°C ) |
|---|---|---|---|
| 5 | 2.5 | 0.7 | 0.38 |
| 10 | 3.3 | 0.7 | 0.30 |
| 20 | 4.1 | 1.4 | 0.24 |
| 25 | 4.5 | 41 | 0.235 |
| 30 | 5.0 | 41 | 0.246 |
| 60 | 7.4 | 41 | 0.28 |
| 120 | 7.4 | 41 | 0.298 |

### 2.4.2.2 Thermal contrasts, Case C2

For soaked-cotton cooling similar trends can be observed for the thermal contrast $\Delta T(t)$ as for Case C1, and they are shown in Fig. 2.9. If the cooling time is shorter than 40 s, the maximum (type one) will occur within less than 3 s after the removal of cooling. Once the cooling duration is longer than 60 s, the maximum $\Delta T_{max}$ (type two) will occur around 23 s. The maximum contrast is larger for shorter cooling times, about 0.3 °C, and it decreases to around 0.18 °C for longer cooling times.

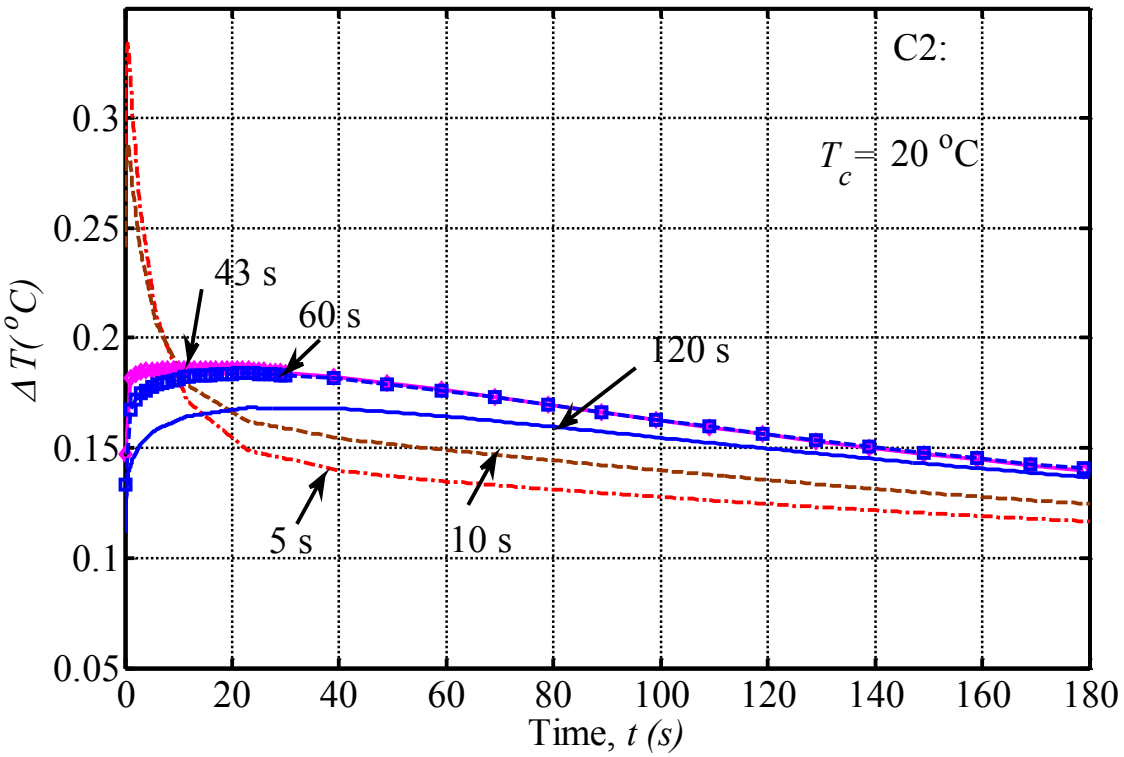


**Figure 2.9** Thermal contrast $\Delta T(t)$ as a function of time with cooling time $t_c$ as parameter ($t_c$ in the range of 5 – 120 s) for soaked cotton cooling (Case C2) with water temperature of $T_c$ = 20 ° C.

The decrease of thermal contrast with increasing cooling time can be explained by the change (increase) of the cotton temperature with time, caused by heating both by the skin and the ambient. Therefore, shorter cooling times are desirable for soaked-cotton cooling, as long as quick optical access (after the removal of the cooling) is feasible. Key results for Case C2 are summarized in Table 2.3. They suggests that, unlike the constant temperature cooling case (Case C1) in which only the second type of maximum increases with cooling times, the values $\Delta T_{\max}$ of both types of maxima decrease with cooling time. Therefore, to maximize $\Delta T_{\max}$, the cooling time should be between 40 and 60 s.

**Table 2.3** Data for soaked cotton cooling, Case C2: cooling penetration depth $D(\mathrm{t_{max}})$, time of maximum thermal contrast $t_{\max}$ and the corresponding $\Delta T_{\max}$ for various cooling durations $t_c$.

| Cooling Time $t_c$ (s) | Cooling Penetration Depth $D(t_{max})$ (mm) | Timing of Max. $\triangle T(t)$ $t_{max}$ (s) | Max. $\triangle T(t)$ $\triangle T_{max}$ (°C ) |
|---|---|---|---|
| 5 | 2.2 | 0.5 | 0.335 |
| 10 | 2.9 | 0.6 | 0.289 |
| 40 | 5.1 | 2.9 | 0.187 |
| 43 | 5.3 | 11.5 | 0.186 |
| 60 | 6.3 | 23 | 0.184 |
| 80 | 7.2 | 23.1 | 0.179 |
| 100 | 8.0 | 23.1 | 0.174 |
| 120 | 8.6 | 23.1 | 0.168 |

### 2.4.2.3 Thermal contrasts, Case C3

Thermal contrasts as a function of time for convective cooling with air are shown in Figs. 2.10(a) and (b). The convection heat transfer coefficients $h$ vary from 50 W/m$^2$ K to 100 W/m$^2$ K (typical values for forced convection in gases or free convection in liquids), and cooling times vary from 5 s to 120 s. For all cooling times in Figs. 2.10(a) and (b), the maximum temperature difference $\Delta T_{max}$ appears immediately after the cooling stress is removed (0–0.2 s into the thermal recovery phase). After the initial maximum, the thermal contrast monotonically decreases with time $t$.

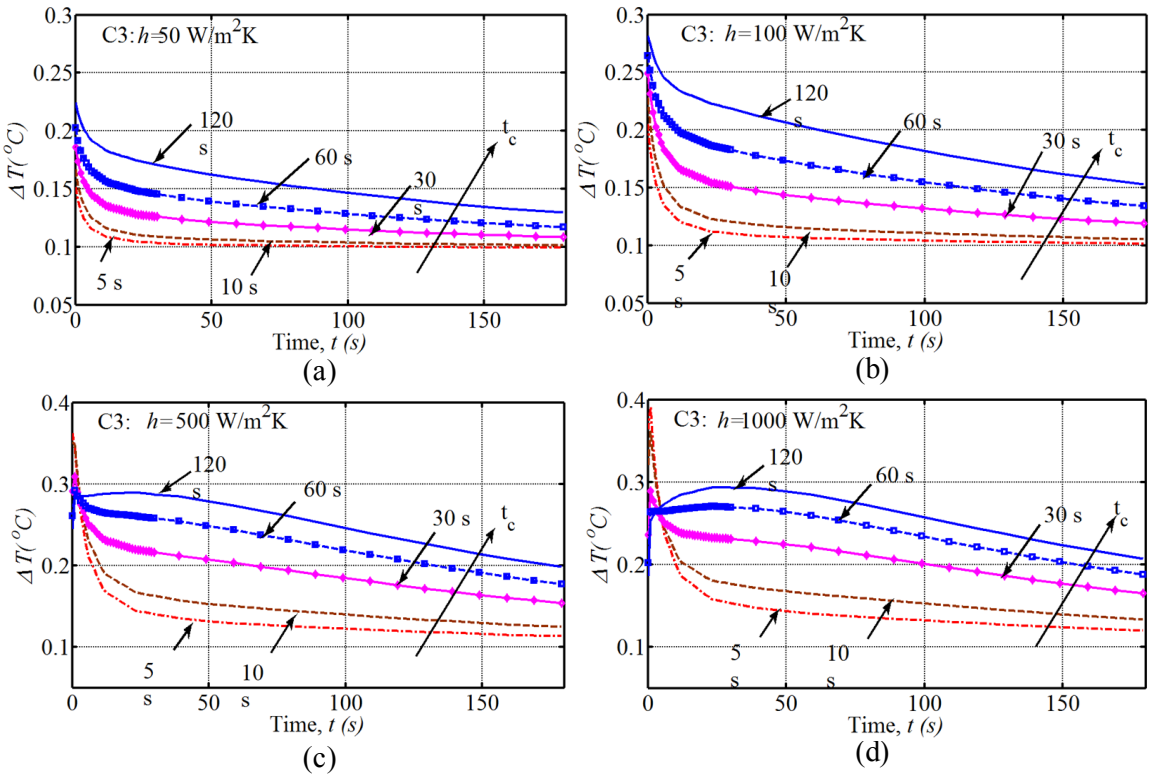


**Figure 2.10** Thermal contrast $\Delta T(t)$ as a function of time with cooling time $t_c$ as parameter ($t_c$ is in the range of 5–120 s) for convection cooling (Case C3) with $T_c$ = 20 °C and $h$ = (a) 50 W/m$^2$ K, (b) 100 W/m$^2$ K, (c) 500 W/m$^2$ K, (d) 1000 W/m$^2$ K.

The overall thermal contrast $\Delta T_{max}$ increases with increasing cooling time $t_c$. Therefore, for air cooling, longer cooling times are desirable and imaging has to commence immediately after the removal of cooling, in order to measure the maximal thermal contrast. Since the thermal contrast is relatively low in magnitude and decreases rapidly, imaging of the first 20 s of the thermal recovery with high temporal resolution is crucial. Thermal contrasts are in the range of 0.15–0.22 °C and 0.2–0.28 °C, for $h$ = 50 W/m$^2$ K and 100 W/m$^2$ K, respectively. Again, these are temperature differences that can be measured with modern infrared cameras.

However, as shown in Figs. 2.10(c) and (d), for higher heat transfer coefficients ($h$ = 500 W/m$^2$ K and 1000 W/m$^2$ K, corresponding to high-velocity air or liquid cooling), the trends change and resemble those for constant temperature (Case C1) and soaked cotton cooling (Case C2). Again, we identify two characteristic behavior types. Using shorter cooling times (below $t_c$ = 60 s for $h$ = 500 W/m$^2$ K, and 30 s for $h$ = 1000 W/m$^2$ K) the maximum thermal contrast is observed within 1 s into the thermal recovery process. The thermal contrast decreases rapidly during the first 20 s of thermal recovery, therefore rapid imaging immediately after the removal of cooling is essential to capture the maximum. $\Delta T_{max}$ is relatively large for these shorter cooling times (0.38–0.29 °C for $h$ = 500 W/m$^2$ K), and it decreases as the cooling time increases. Therefore, we can conclude that shorter cooling times (<25 s) and short imaging times (<15 s) are sufficient for lesions less than 4 mm deep.

As summarized in Table 2.4, for $h$ = 500 W/m$^2$ K, the second type of maximum $\Delta T_{max}$ is detected at 23 s into the thermal recovery for cooling times longer than 110 s. For 110 s of cooling, the cooling penetration depth $D(t_{max})$ reaches 9 mm,

therefore longer cooling times and imaging times are better suited for imaging of deeper lesions.

**Table 2.4** Data for convection cooling, Case C3: cooling penetration depth $D(t_{\max})$, time of maximum thermal contrast $t_{\max}$ and the corresponding $\Delta T_{\max}$ for various cooling times $t_c$.

| Cooling Time $t_c$ (s) | Cooling Penetration Depth $D(t_{max})$ (mm) | Timing of Max. $\triangle T(t)$ $t_{max}$ (s) | Max. $\triangle T(t)$ $\triangle T_{max}$ (°C ) |
|---|---|---|---|
| | $h$=50 W/m$^2$K | | |
| 5 | 0.8 | 0 | 0.152 |
| 10 | 1.4 | 0 | 0.166 |
| 30 | 3.1 | 0 | 0.186 |
| 60 | 4.0 | 0 | 0.203 |
| 120 | 6.4 | 0 | 0.224 |
| | $h$=100 W/m$^2$K | | |
| 5 | 1.2 | 0 | 0.205 |
| 10 | 2.1 | 0 | 0.228 |
| 30 | 3.6 | 0.1 | 0.249 |
| 60 | 5.0 | 0.2 | 0.265 |
| 120 | 7.9 | 0.2 | 0.284 |
| | $h$=500 W/m$^2$K | | |
| 5 | 2.0 | 0.2 | 0.381 |
| 10 | 2.8 | 0.3 | 0.373 |
| 30 | 4.3 | 0.5 | 0.318 |
| 60 | 6.7 | 0.7 | 0.295 |
| 120 | 9.6 | 23 | 0.289 |
| | $h$=1000 W/m$^2$K | | |
| 5 | 2.2 | 0.5 | 0.418 |
| 10 | 2.3 | 0.5 | 0.378 |
| 30 | 4.7 | 0.7 | 0.294 |
| 60 | 6.8 | 23.1 | 0.270 |
| 120 | 9.9 | 23.1 | 0.294 |

### 2.4.3 Sensitivity analysis for the variation of tissue properties

In order to investigate the influence of the variation of tissue properties on the thermal contrast, a sensitivity analysis was conducted for two model parameters: blood perfusion rate in the papillary dermis and skin layer thickness. Based on prior results [2], these two parameters were found to be the key factors leading to highest surface temperature uncertainties. The sensitivity is addressed by comparing surface temperature distributions for the ranges of the two parameters between the maximum and minimum values found in the literature [57-59] and summarized in Table 2.5.

**Table 2.5** Variation range of tissue thickness and blood perfusion rate for the sensitivity analysis.

| | Tissue Thickness (mm) | | | |
|---|---|---|---|---|
| Skin layer | T1 | M | T2 | T3 |
| Epidermis | 0.08 | 0.1 | 0.09 | 0.1 |
| Papillary dermis | 1 | 1 | 1 | 1 |
| Recticular dermis | 0.6 | 1 | 0.8 | 1 |
| Fat | 2 | 2 | 3 | 4 |
| Muscle | 8 | 8 | 8 | 8 |
| | Blood Perfusion (1/s) | | | |
| Skin layer | B1 | M | B2 | B3 |
| Epidermis | 0 | 0 | 0 | 0 |
| Papillary dermis | 0.00018 | 0.00018 | 0.002 | 0.0036 |
| Recticular dermis | 0.00018 | 0.00126 | 0.002 | 0.0036 |
| Fat | 0 | 0.00008 | 0.00009 | 0.0001 |
| Muscle | 0.0005 | 0.0027 | 0.006 | 0.01 |

Four cases were computed for each parameter of interest, respectively, while the remaining parameters (not listed in Table 2.5) were kept at their nominal values shown in Table 2.1. Case M in Table 2.5 represents the set of nominal parameters in the primary model described in Table 2.1. When considering the tissue thickness variation range indicated in the literature [57, 59], T1 represents the case with thinnest layer combination (Table 2.5), and T2 and T3 in Table 2.5 represent the medium and thickest layer combinations. Similar to this, in the analysis of blood perfusion B1 is the scenario with the lowest perfusion rate in all layers, while B2 and B3 represent scenarios of medium and high blood perfusion rates, respectively.

Constant temperature cooling (C1) using 20 °C for 60 s is applied in all the cases considered, and the results of the sensitivity analysis are displayed in Fig. 2.11. By comparing case T1 with the nominal case M in Fig. 2.11(a), we can observe that the thermal contrast is slightly higher due to the reduced thicknesses of the near-surface layers (epidermis and dermis). A similar increase of thermal contrast can also be observed for the parameter combinations T2 and T3, in which both the near-surface and deeper layers are thicker than for T1. Since the thickness increase of the insulating fat layer is larger than that of the near-surface layer, the increased thermal contrast remains in cases T2 and T3. The thermal conductivity of fat is less than half of the thermal conductivity of near surface layers. The thermal contrast therefore decreases with the increasing thickness of near-surface layers, however, it also increases with the thickness of fat layer. This result is significant, since the thickness of the fat layer can vary in a wide range. This sensitivity analysis demonstrates that the increase of its thickness won't adversely affect the diagnostic ability for near-surface lesions. The results in Fig. 2.11(a)

suggest that the timing of maximum thermal contrast does not change with the tissue thickness.

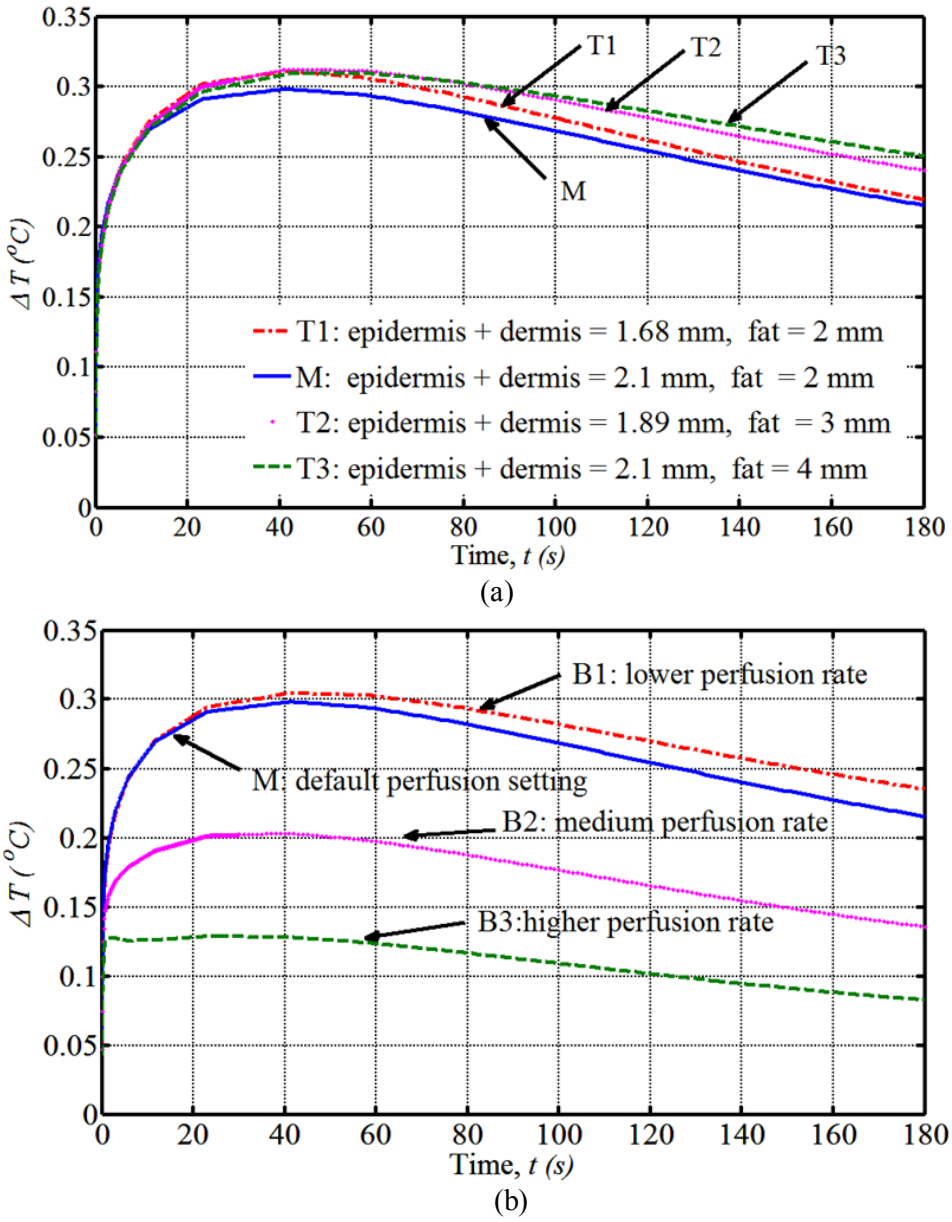


**Figure 2.11** Sensitivity of thermal contrast to (a) skin thickness variations and (b) blood perfusion variations. Properties for T1-T3 and B1–B3 are summarized in Table 2.5.

On the other hand, results in Fig. 2.11(b) indicate an obvious decrease of thermal contrast due to increased blood perfusion in skin layers. Since the perfusion rate of the lesion is kept constant in the analysis, this effect can explained by the enhanced thermal recovery rate of healthy skin, which reduces the temperature difference between the lesion and healthy skin. In addition, the timing of maximal thermal contrast is shifted to an earlier time, the difference being a few seconds. The data indicate the need to start imaging immediately after the removal of the cooling stress. Several image frames per second should be captured during the first 5–10 s. These results confirm the significance of increased blood perfusion as one of the indicators of cancer, recognized widely in the medical literature [2, 30-35, 54]. They also suggest that measuring and comparing blood perfusion rates of diseased and healthy tissue may serve as foundation for quantitative assessment of cancerous skin lesions. Further clinical studies are needed to investigate this hypothesis. The thermal contrast is sensitive to the variation of blood perfusion, however, even for the highest perfusion case (B3), its maximum value is larger than 0.1 °C, which is detectable with modern, precision IR cameras.

### 2.4.4 Sensitivity analysis for skin surface emissivity

It is a common misconception in the medical and engineering communities that the emissivity of the human skin varies in a wide range, both locally and from individual to individual, and that this variation makes thermal models inaccurate and prevents accurate temperature measurements. However, this is not the case, based on measurement data reported in the literature [65-67]. The emissivity of intact human skin, in spite of the significant differences in color and surface structure, is relatively constant, and varies in

the range of $0.98 \pm 0.01$ in the wavelength range of 2 μm – 14 μm [65-67]. In order to evaluate the effects of surface-to-ambient radiation on thermal contrast, we incorporated this effect into our skin heat transfer model as an additional thermal boundary condition on the skin surface, described by the Stefan-Boltzmann law as

$$q'' = \varepsilon\sigma(T_{sur}^4 - T_{amb}^4) \, . \tag{2.12}$$

This assumption holds, as the imaged portion of the skin surface is small compared to the surroundings (a large exam room which is typically at ambient conditions at 21 °C). In Eq. (2.12) $q''$ is the radiation heat flux to the ambient, $\varepsilon$ the skin emissivity, $\sigma$ the Stefan-Boltzmann constant, $T_{sur}$ the skin surface temperature during the thermal recovery phase, and $T_{amb}$ the ambient temperature, which is 21 °C in the simulation.

For Case C1 (60 s of constant temperature cooling) we evaluated the thermal contrast for three representative emissivity values: 0.8 (extreme low), 0.98 (typical value), and 1.00 (blackbody, extreme high) to assess the role of the emissivity. The computed thermal contrast during the thermal recovery phase for the three emissivity values and for the nominal Case C1 is plotted in Fig. 2.12. We can observe only a slight difference in thermal contrast (at later thermal recovery times which are less important in a diagnostic measurement) as a consequence of surface-to-ambient radiation, which is not going to affect the diagnostic ability of the imaging system. The change in the maximum value of the thermal contrast is less than 0.13% as a result of surface-to-ambient radiation for the range of emissivities of 0.8–1.0. Thus, since the normal emissivity variation of human

skin is much smaller, 0.98 ± 0.01, we can conclude that the sensitivity of thermal contrast measurement to skin emissivity is negligible.

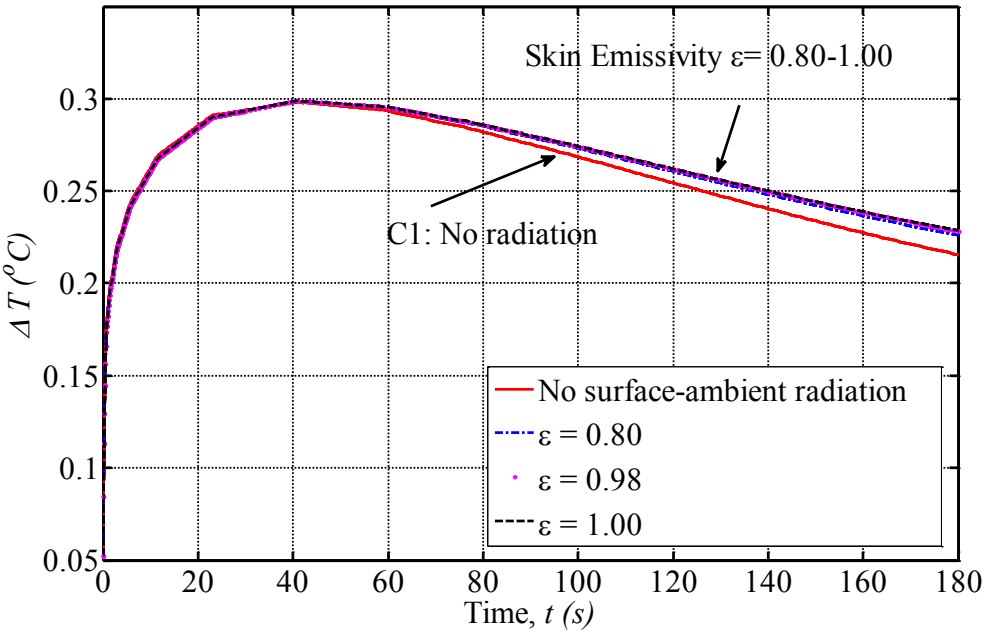


**Figure 2.12** Sensitivity of thermal contrast to the variation of skin surface emissivity.

## 2.4.5 Model validation and comparison to experimental data

To validate the numerical predictions of skin cooling and our thermal model reported in this chapter, experimental data obtained by IR imaging of a malignant melanoma lesion and the surrounding healthy skin, reported in our previous publications [4, 6] are used for comparison. The malignant melanoma lesion was classified as Clark level II (superficial spreading type), with the depth of 0.44 mm and approximate width 2 mm. The lesion is elongated and irregular in shape. In the patient study, the lesion was cooled by applying a thin gel pack for 60 s, and the temperature of the region of interest was cooled down to around 14 °C at the end of cooling phase. For more details about the lesion, experimental

technique and experimental data, the reader is referred to previous publications of our group [4, 6]

To simulate the thermal behavior during cooling and thermal recovery of this lesion, we consider a cross section of this lesion which is assumed to be elliptical in shape, with the major diameter (W) and minor diameter (P) of 2 mm and 0.5 mm, respectively (Fig. 2.2(a)). To simulate the cooling effect, in the computational model the cooling with the gel pack was approximated by the constant temperature cooling (Case C1) at 14 °C.

Measured and computed thermal recovery temperatures for the lesion and healthy skin are plotted in Fig. 2.13(a); the full line shows computed results and discrete points correspond to experimental data. Experimental results indicate a maximum thermal contrast of around 2.5 °C, which is higher than the values computed in the previous sections. Since the exact parameters and thermophysical properties of the melanoma lesion are not available from experiment or literature, we increased the blood perfusion rate of the lesion to $\omega_b = 0.045(1/s)$ in the calculations to match the magnitude of the measured thermal contrast. Our results suggest that general lesion data reported in the literature [63] probably underestimate the blood perfusion rate of the melanoma lesion. Since property data for lesions, especially very small ones, are rare or nonexistent, the uncertainties in the thermal models and results have to be addressed through an uncertainty analysis, as discussed previously by Cetingul and Herman [2]. Clearly, for accurate thermal models, accurate thermophysical property data are essential, and their noninvasive, in vivo measurement poses a continuing challenge. The remaining

parameters of the computational model (Table 2.1) remained the same for the validation analysis.

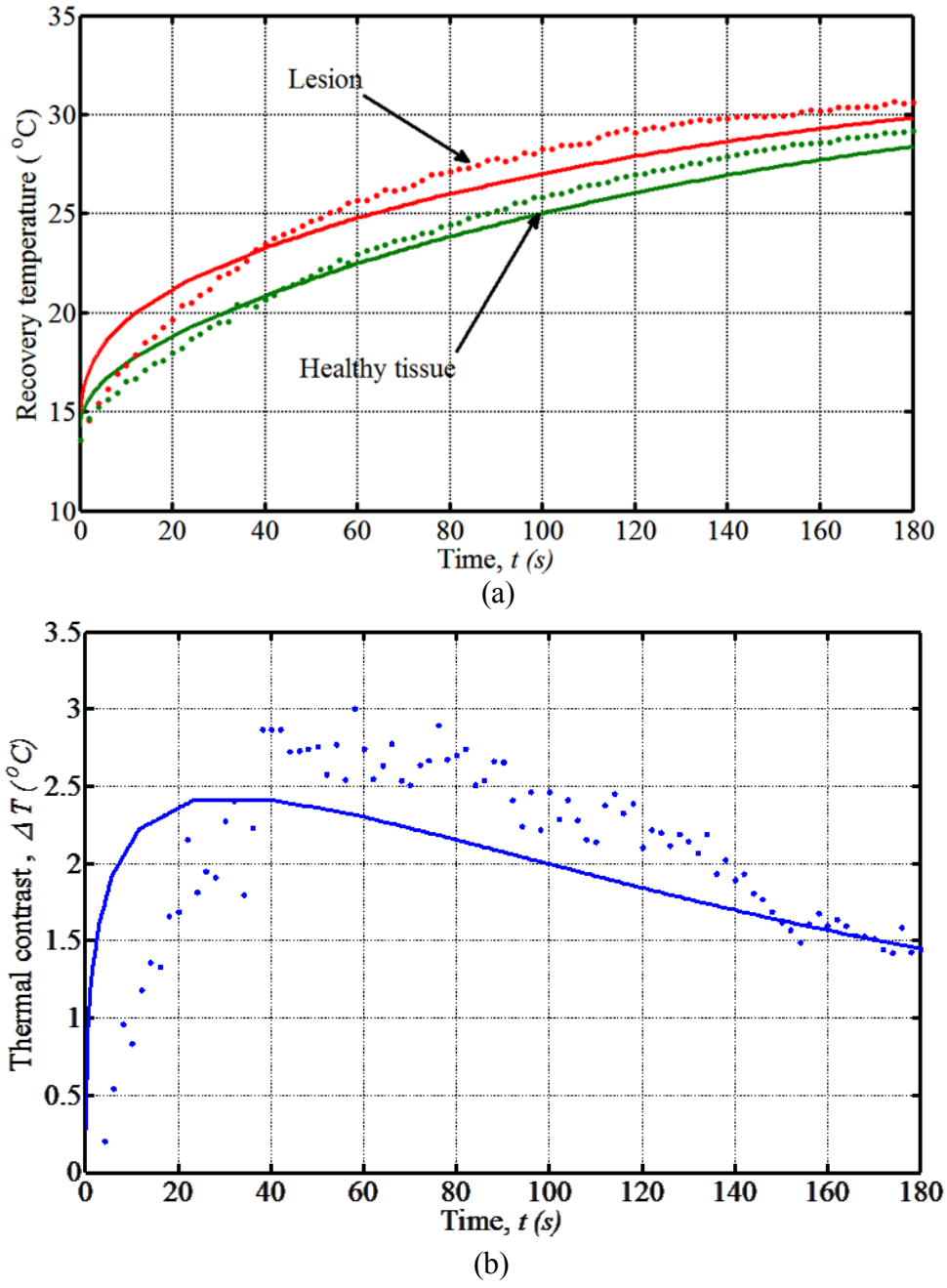


**Figure 2.13** Comparison between computed results (full line) and experimental data (discrete data points): (a) thermal recovery of the lesion and healthy skin and (b) mean value of the measured thermal contrast (nine adjacent pixels) and the computed thermal contrast.

For the experimental data in Fig. 2.13, we sampled nine adjacent pixels (arranged in a square pattern) at two selected locations (lesion and healthy tissue), and the template-based motion tracking method (to be discussed in Chapter 3) [68, 69] was applied to record the temperature at these pixels during thermal recovery. The temperature differences between each pair of lesion/healthy point data sets were computed, and the mean value of the temperature difference between lesion and healthy tissue during the thermal recovery phase is plotted in Fig. 2.13(b). It can be observed that the thermal recovery curves in both simulation and experiment are very similar. The scatter in the experimental data can be attributed to imperfect motion tracking (accounting for involuntary movements of the patient) in the infrared image sequence. In Fig. 2.13 (b), the trend of the measured thermal contrasts is very similar to that predicted by the numerical model. The maximum value occurs around 40–60 s into the thermal recovery phase both in the computed and experimental results.

# 2.5 Conclusions

The analysis of cooling penetration indicates that for constant temperature, soaked cotton and convective cooling with sufficiently high heat transfer coefficients ($\geq$500 W/m$^2$ K), it takes fewer than 30 s for the cooling effect to reach the depth of 4 mm. This is the desired cooling depth for the detection of near-surface lesions. Therefore, for the range of cooling temperatures considered in this study (4 °C – 20 °C), 30 s is an acceptable cooling time for a variety of clinical applications. The analysis of cooling penetration also suggests

that the cooling temperature of 20 °C is usually sufficient for the cooling effect to reach the desired depth within less than 1 min.

By analyzing thermal contrast for the three cooling methods, two types of thermal recovery behaviors can be identified, one for short cooling times and another for longer cooling times. When the cooling time is less than 30 s, i.e. the cooling penetration depth is less than 4 mm, an immediate maximum of thermal contrast appears within the first few seconds after the removal of cooling. Following the maximum, the thermal contrast drops rapidly within the next 20 s.

On the other hand, when the cooling time exceeds 40 s, the second type of maximum is observed around 20–45 s into the thermal recovery. The magnitude of this maximum increases with increasing cooling time for constant temperature cooling (Case C1) and convective cooling (Case C3) with high heat transfer coefficients ($\geq$500 W/m$^2$ K). For soaked cotton cooling (Case C2), however, the magnitude decreases with increasing cooling time.

For all cooling methods considered in this study, the magnitude of the maximum of the first type is higher than that of the second type. The second type of maximum is broader and easier to capture with imaging systems that have a moderate frame rate, as high thermal contrast is available longer. The second type of thermal recovery may be preferable in the clinical environment since the clinician will have sufficient time to capture the maximum thermal contrast. A shorter cooling time could be more suitable for small, superficial lesions, which can be detected with a stronger thermal contrast early in the thermal recovery phase. The dependence of thermal recovery behavior on the cooling time thus provides the basis for optimization. The choice of the cooling time, method,

and temperature will be ultimately determined by the available equipment and the characteristics of the lesion being imaged.

The results suggest that it is feasible to apply a moderate temperature of about 20 °C to achieve effective skin cooling, with an acceptable cooling duration (<2 min) in a clinical setting. This level of cooling is not likely to cause discomfort to the patient. The duration of cooling can be further adjusted by considering the characteristics of the lesion to optimize thermal contrast for better measurement data and improved clinical convenience.

# Chapter 3

# Motion tracking in infrared imaging for quantitative medical diagnostic applications

## 3.1 Overview

As discussed in Chapter 2, IR diagnostic techniques rely on the hypothesis that a distinct thermal signature associated with a medical condition can be detected and quantified using modern camera technology. The common goal in thermographic diagnostic applications is to measure skin temperature as a function of location and time with high accuracy. These measurements are complex, since the shape of the surface, the surface properties and the motion of the subject will influence the temperature data derived from signals captured by the sensor. Thus, this chapter addresses the influence of the subject's

motion on IR temperature measurements and proposes methods to compensate for the motion in order to achieve high-accuracy temperature measurements. The influence of surface shape will be discussed in Chapter 4.

## 3.2 Background

Infrared imaging can be implemented either as a static or as a dynamic technique in medical diagnostic applications. In static imaging applications a steady state situation is analyzed: the subject is typically exposed to normal ambient conditions and the spatial distribution of thermal contrasts on the body is measured and analyzed. Dynamic IR imaging detects both spatial and temporal variations of the emitted IR radiation, and this signal is related to skin temperature during post processing. Prior to image acquisition, a thermal excitation, such as cooling or heating, is applied to skin surface in dynamic IR imaging. During and following the thermal excitation a sequence of consecutive image frames is acquired, and the motion of the subject during the image acquisition poses a significant challenge for accurate surface temperature measurements. The phase after the removal of the thermal excitation is the thermal recovery process, which is frequently analyzed in medical imaging applications. By analyzing the thermal recovery of the skin temperature, with temperature variations in the range of hundreds of millikelvins, abnormalities such as the malignancy of skin lesions can be examined, quantified and potentially diagnosed (with appropriate calibration and clinical validation) [1-7].

However, during the image acquisition period, the involuntary movements of the patient are unavoidable, and such movements will undermine the accuracy of temperature

measurement for any particular location on the skin. As shown in Fig. 3.1, in clinical applications of medical IR imaging [4, 6], the patient is typically motionless, positioned on a fixed exam chair or bed, and the IR camera is oriented towards the lesion on the skin with the camera axis perpendicular to the skin surface. Since the out-of-plane movements of the patient are limited and restrained by the exam chair, they result in a predominantly linear in-plane motion in the image sequence, as illustrated in Fig. 3.2. This linear in-plane motion is considered to be the major source of motion encountered in the clinical IR image analysis.

Although such in-plane motion is relatively small and limited in range, it still hinders the successive measurement of temperature at a particular location on the skin surface in the IR image sequence. For example, early stage melanoma lesions are small (of the order of a few millimeters), and therefore movements of the order of a millimeter will hinder the localization of any subtle thermal features [3]. The measured temperature differences are often very small as well (fraction of a degree) and the feature to be analyzed (the lesion) cannot be detected directly in the IR image, prior to image processing. In static IR imaging, in which the temperature of the skin is approximately constant over time, accurate tracking can locate the lesion automatically in the IR image without the aid of a visible landmark. In dynamic IR imaging the temperature of the skin and the signal detected by the camera sensor change over the time [2, 4, 6]. In such applications motion tracking is crucial to record the temperature evolution accurately over the image sequence.

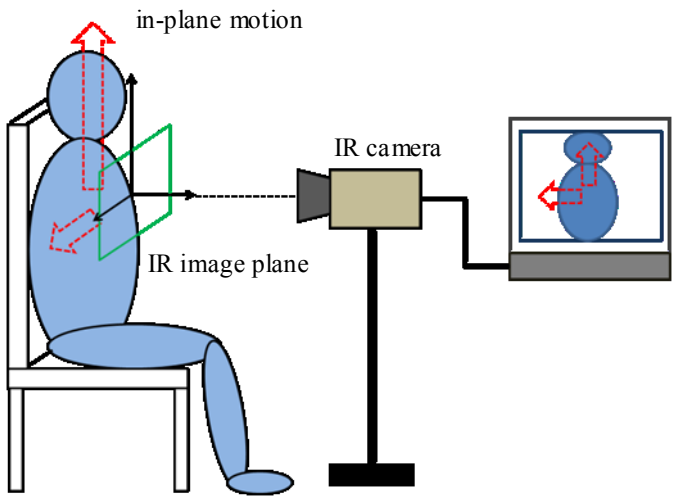


**Figure 3.1** Schematic of subject's motion due to respiration and small involuntary movements of the body and limbs in the clinical IR imaging environment with the patient positioned in the exam chair.

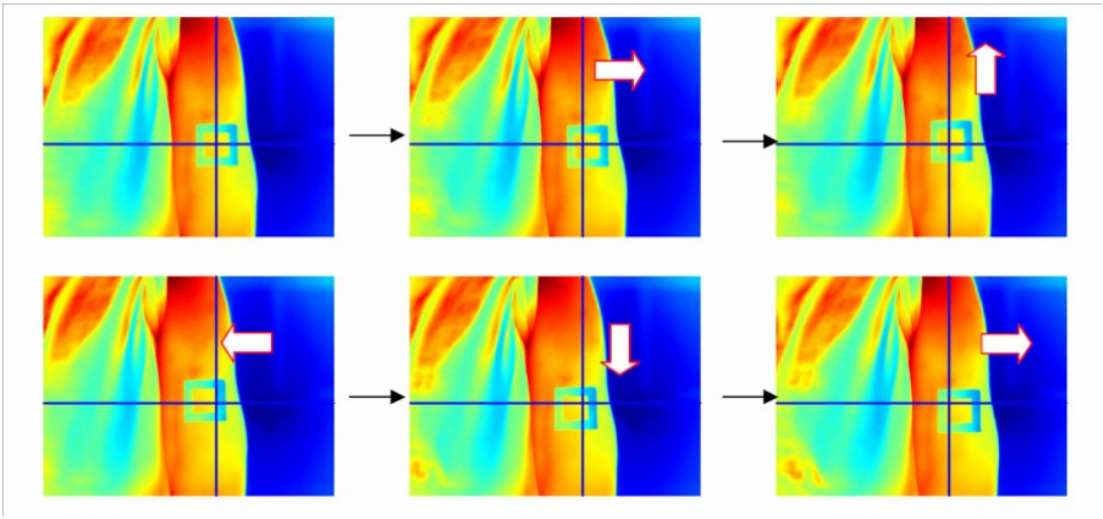

**Figure 3.2** Sample infrared images illustrating the subject's in-plane motion in the acquired IR image sequence. The white arrows show the motion direction relative the previous frame (the adjacent frame on the left hand side), the rectangle is the template of known dimensions used for matching white light and infrared images, and the crosshair indicates a particular pixel location in the image frame, originally positioned in the center of the rectangular template. The changes of the location of the rectangular template relative to the crosshair are caused by involuntary motion of the subject.

## 3.3 Literature review

Tracking a moving object in an image sequence is an active topic in civil and military applications. Initial applications were developed for white light imaging, however, motion and target tracking in IR image sequences has become the subject of increasing interest in recent years as well. Due to the lower cost and fast improvement of infrared (IR) technology, object tracking has also been widely used in IR imaging, such as pedestrian detection for surveillance purposes [70-72]. In IR surveillance applications the target typically stands out against the background, it often covers a relatively small fraction of the total image frame area, the range of motion is large and accurate temperature information is generally not of interest.

Only a few researchers have tackled the motion tracking challenge in IR imaging in medical applications [3, 7]. The key difference between surveillance and medical applications is the smaller thermal contrast between the diseased and healthy tissue, which is often not detectable without sophisticated image processing. Also, the target often covers a significant portion of the image frame. The range of motion of the subject is smaller and accurate quantitative detection of temporal as well as spatial variations is essential. Most of the past clinical applications of IR imaging focused on breast cancer detection. To enable the wide use of dynamic IR imaging in breast cancer screening [73-75], the motion artifact reduction approach using image sequence realignment was proposed [76-78] with marker-based image registration. Image registration involves transforming different data sets into one coordinate system. In medical imaging and computer vision applications registration is essential in order to allow the comparison or

integration of data obtained from different measurements and sources, in our application from white light and infrared images. In breast cancer imaging [14-16], the registration of each IR image frame is achieved by aligning 5 to 18 markers (which are directly visible in the successive images) to serve as control points in the IR image sequence. The approach can achieve accurate tracking performance in terms of signal to noise ratio (SNR).

In the Heat Transfer Lab of Johns Hopkins University, we have developed a dynamic IR imaging system for the detection of melanoma [2-7]. The system relies on thermal stimulation with external cooling and compares the transient thermal response of cancerous lesions and healthy skin. As shown by Pirtini Cetingul and Herman [3, 7], based on the quadratic motion model for landmark-based registration, a sequence of IR images acquired during the thermal recovery phase can be aligned to compensate for involuntary motion of the patient. The motion compensation enables an accurate measurement of temperature differences between lesions and healthy skin, and provides quantitative information to identify the malignancy of lesion. Without motion tracking, the measurement errors are too large to detect temperature differences that are indicative of malignancy [4-6]. Based on the experiences gained in our previous clinical studies, in this study, a template-based tracking scheme is applied for dynamic IR imaging.

In the field of computer vision, automatic methods for tracking the moving object in an image sequence fall into three main categories [79, 80]: feature-based tracking [81, 82], contour-based tracking [83, 84], and region-based tracking [85, 86]. In the absence of occlusions, region-based tracking methods perform well in terms of robustness and accuracy. Template-based tracking [87] falls into the category of region-based tracking methods. When compared with other region-based methods with non-parametric

description of the region's content [88], template-based tracking directly uses a region content of the image to track the moving object. This is accomplished by extracting a template region in the first frame and finding the best matching region in the following frames. In this way the moving object can be tracked in a video sequence.

The template-based tracking method is originally based on the assumption that the object's appearance remains constant throughout the video sequence. However, in practical IR imaging applications this assumption often holds only for a certain period of time. The appearance of the object would change significantly with time and changes in the environment, for example as the temperature of the object changes during thermal recovery in dynamic IR imaging. Considering the tracking error due to the violation of initial assumption, improvements in the tracking algorithm, including template update [89] and the inclusion of robust weighting mask for template matching [80], are proposed in this chapter. We introduce the tracking method and validate it on two characteristic classes of problems relevant for medical applications, the static and dynamic imaging of skin temperature.

## 3.4 Algorithm and methods

### 3.4.1 Template-based tracking algorithm

In clinical applications of IR imaging a marker (a rectangular shape applied to skin in our experiment, Fig. 3.3(b)) is commonly used for the registration of the skin lesion [4, 6]. This marker can simultaneously serve as the landmark of consistent appearance in the template region. The template image is a sub-region of an image which contains the object (skin lesion, for example) to be tracked in the image sequence. Template-based tracking is achieved by estimating coordinate alignment between the template image and the consecutive frames in a given video sequence. Since the involuntary movements of patient are mainly in-plane motions with a limited range, the template-based method is well suited for motion tracking in medical IR imaging. In this chapter, the method is described using the notation of Mathews et al. [89].

The alignment of images in a sequence can be parameterized as a warp function, which transforms the pixel coordinate $x$ in the template image to a new coordinate $W(x;p)$ in the subsequent image frame. In this expression $p$ denotes the transformation parameters $p=(p_1,\ldots p_n)^T$ of the warp function. In our application, a sub-region containing the object in the initial IR image frame $I_0(x)$ is extracted to be the template image $T(x)$. In a subsequent image frame $I(x)$, the template image content at pixel $x$, $T(x)$, will be warped by $W(x;p)$ and presented as $I(W(x;p))$. It would have similar content as its corresponding source region in the template image if the tracking is valid. Therefore, optimized parameters $p$ will be sought to find the best match as

$$I\big(W(x;p)\big) \approx T(x)\,. \tag{3.1}$$

In template-based tracking, the 2D affine transformation is utilized as the warp function $W(x;p)$. Linear transformations, including translation, rotation, shear mapping, and scaling, are all taken into account, and any two parallel lines will remain parallel after the transformation. The affine warp consists of 6 independent parameters $p=(p_1, p_2, p_3, p_4, p_5, p_6, )^T$ to model the transformation as

$$W(x;p) = \begin{pmatrix} 1+p_1 & p_3 & p_5 \\ p_2 & 1+p_4 & p_6 \end{pmatrix} \begin{pmatrix} x \\ y \\ 1 \end{pmatrix}, \tag{3.2}$$

where $(p_5, p_6)$ are two parameters describing translation, $(p_1, p_4)$ are two parameters for the scaling of $x$ and $y$, and $(p_2, p_3)$ describe the angular change of each axis after warping.

## 3.4.2 Lucas-Kanade approach

The first use of image alignment with a template reported in the technical literature is the Lucas-Kanade optical flow algorithm [87]. Since this work, the approach has become one of the most widely used methods in object tracking. In the remainder of this section, the notation of Baker and Matthews [90] is used to describe the algorithm. In order to search for the optimized parameters $p$ for the warp function, the objective of the Lucas-Kanade algorithm is to minimize the sum of square errors between the image content of $I(W(x;p))$ and the template $T(x)$ as

$$\sum_x [I(W(x;p)) - T(x)]^2 \ . \tag{3.3}$$

The minimization of Eq. (3.3) is a non-linear optimization problem. Based on a current estimate $p$ for the warping parameters, the Lucas-Kanade algorithm iteratively solves for an increment $\Delta p$ to update the current estimation using

$$p^{new} \leftarrow p + \Delta p . \tag{3.4}$$

Equation (3.3) can be re-written as the error function

$$\sum_x [I\big(W(x; p + \Delta p)\big) - T(x)]^2 . \tag{3.5}$$

The iteration process will continue until the estimate of $p$ converges, and the converged estimate will serve as the new set of optimized parameters $p$ for the warp function $W(x;p)$.

Furthermore, to linearize the error function (3.5), the first-order Taylor expansion is used to approximate $I(W(x;p+\Delta p))$ as

$$I\big(W(x; p + \Delta p)\big) = I\big(W(x; p)\big) + \nabla I \frac{\partial W}{\partial p} \Delta p . \tag{3.6}$$

Therefore, by substituting $I(W(x;p+\Delta p))$ described by Eq. (3.6), into (3.5), the error function can be written as [90]

$$\sum_x \left[I\big(W(x; p)\big) + \nabla I \frac{\partial W}{\partial p} \Delta p - T(x)\right]^2 , \tag{3.7}$$

where $\nabla I$ is the gradient of image $I$ evaluated when the current warp function $W(x;p)$ is applied, and $\frac{\partial W}{\partial p}$ represents the Jacobian of the warp.

The affine transformation $W(x;p)$ can be decomposed as $W(x;p)=(W_x, W_y)^T$, and the Jacobian of $W(x;p)$ is represented as

$$\frac{\partial W}{\partial p} = \begin{pmatrix} \frac{\partial W_x}{\partial p_1} & \cdots & \frac{\partial W_x}{\partial p_6} \\ \frac{\partial W_y}{\partial p_1} & \cdots & \frac{\partial W_y}{\partial p_6} \end{pmatrix} = \begin{pmatrix} x & 0 & y & 0 & 1 & 0 \\ 0 & x & 0 & y & 0 & 1 \end{pmatrix}. \tag{3.8}$$

Based on equation (3.8), to minimize the error function (3.7), we first determine its partial derivative with respect to $\Delta p$ and set it to zero. Next, the closed-form solution for the $\Delta p$ can then be obtained as [90]

$$\Delta p = H^{-1} \sum_x \left[ \nabla I \frac{\partial W}{\partial p} \right]^T [T(x) - I(W(x;p))]. \tag{3.9}$$

In Eq. (3.9) $H$ is the $n \times n$ Hessian matrix and the Gauss-Newton approximation is adopted for the Hessian matrix as

$$H = \sum_x [\nabla I \frac{\partial W}{\partial p}]^T [\nabla I \frac{\partial W}{\partial p}]. \tag{3.10}$$

### 3.4.3 The weighting function for robust tracking

Constant brightness over the entire image sequence is the primary assumption for template-based tracking. This assumption is often violated when the brightness variations are unavoidable, such as the imaging of transient processes. In our application the assumption can hold for the static IR image sequence. For the dynamic IR image sequences this assumption will be violated, since the purpose is to analyze the time-varying thermal signal of a skin lesion recovering from a cooling excitation.

Therefore, to tackle the problem of brightness variation in dynamic IR image data, the robust version of Lucas-Kanade tracking algorithm [80, 91, 92] is implemented in our application. The robust version adds a weighting mask to the template pixels in the

computation of the least square process. In this algorithm the pixels with brightness change in the template image will be treated as outliers, and their contribution will be suppressed in the computation. Furthermore, to improve the efficiency of the Lucas-Kanade algorithm, the inverse compositional algorithm [90-92] is also implemented in the robust version. In the inverse compositional algorithm the roles of the template image *T(x)* and the subsequent image *I(x)* are interchanged. Based on the notation of [91, 92], a weighing mask *M(x)* of the same dimensions as the template image is included in the least square process to replace Eq.(3.5)

$$\sum_x M(x) \cdot [I\big(W(x; p + \Delta p)\big) - T(x)]^2 \ . \tag{3.11}$$

The closed-form expressions for the increment $\Delta p$, described by Eqs. (3.9) and (3.10), will be replaced by corresponding equations in the robust version of Lucas-Kanade tracking algorithm in the form

$$\Delta p = \bar{H}^{-1} \sum_x M(x) \cdot \left[\nabla T \frac{\partial W}{\partial p}\right]^T [I\big(W(x; p)\big) - T(x)] \quad \text{and} \tag{3.12}$$

$$\bar{H} = \sum_x M(x) \cdot [\nabla T \frac{\partial W}{\partial p}]^T [\nabla T \frac{\partial W}{\partial p}] \ . \tag{3.13}$$

### 3.4.4 Infrared image acquisition

To test the tracking performance of the algorithm, a subject's left hand with deliberate random in-plane motion is imaged using an IR camera. Two types of IR image sequences were tested in this study:

A. **Steady-state IR image sequence:** in the first imaging experiment, the temperature of the skin does not change with time, therefore the basic tracking performance can be tested under the constant brightness assumption.

B. **Thermal recovery IR image sequence:** In our previous clinical application [4], the thermal recovery IR image sequence after cooling reveals critical information to detect the malignancy of melanoma lesions. Thus in the second experiment, we first applied cooling to the skin for 60 seconds, and acquired the IR video after the cooling was removed. The temperature changes cause significant changes of brightness in the IR image sequence. Using these test images, the robustness of the tracking algorithm can be tested for the situation when the skin temperature changes with time.

As shown in Fig. 3.3(a), the camera used in the experiment is a Merlin midwave (3-5 μm) infrared camera (MWIR) (FLIR Systems Inc., Wilsonville, OR), which has the temperature sensitivity of 0.025℃. A 320 × 256 pixel InSb focal plane array (FPA) is used to acquire 16 bit raw data at frame rate of 60 Hz. Each image frame has the field of view (FOV) of 22 × 16 degrees. Using the parameters obtained from black body calibration [93], the camera can generate an IR thermal image calibrated as temperature value.

### 3.4.5 Template image and the simulated lesion

In general, a skin lesion (early stage melanoma is of particular interest in the present study) is not directly identifiable in the IR image because the temperature difference between the lesion and the healthy skin is typically very small under steady state conditions, i.e. it is of the order of natural temperature fluctuations of the skin. The temperature difference increases during dynamic imaging, which imposes the need to track a particular physical location on the skin throughout an image sequence. To implement the template-based algorithm and evaluate its performance, we created two paper markers which are both visible in the IR image (Figs. 3.3 (b) and (c)). One of them is a 5 cm × 5 cm square marker, which serves as the constant feature in the template image as shown in Fig.3.3 (c). The second one is a small, round maker, which is easy to segment in the IR image, and it mimics the lesion. Using such a lesion phantom allows the assessment of the tracking results quantitatively.

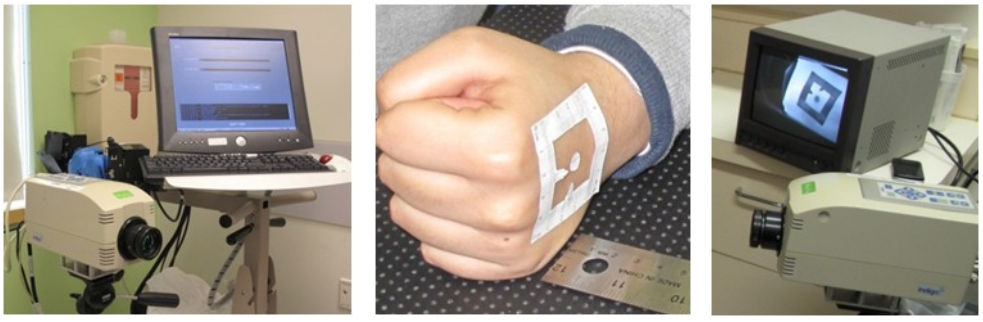

(a) (b) (c)

**Figure 3.3** (a) The Merlin midwave infrared camera and the IR image acquisition system. (b) Two paper adhesive markers: the square one serves as the tracking template and the round one represents the simulated lesion for error analysis. (c) IR image of the adhesive markers shown on the monitor connected to IR camera.

### 3.4.6 Weighting mask for the template image

As introduced in Section 3.4.3, to implement the robust version of Lucas-Kanade algorithm [80, 90-92], we used the normalized intensity of the template image as the weighting mask. In the template image, the image brightness is normalized in the range (0, 1) with respect to the lowest and the highest temperature value. This normalized image serves as the weighting mask $M(x)$ in Eq.(3.11). The weighting mask treats a pixel x as reliable if $M(x)$ =1, and a pixel x is considered an outlier if $M(x)$=0. The two weighting masks for the steady-state and thermal recovery IR image sequence are displayed in Figs. 3.4(a) and (b). It can be observed that the skin region outside the square marker, which has higher and more constant temperature throughout the IR video, will be highly weighted by the weighting mask (Fig. 3.4(b), light colored region). On the other hand, the region exposed to cooling in the thermal recovery template image (Fig.3.4(b), darker region), which has lowest temperature but highest brightness variation rate, will be suppressed as unreliable outlier pixels by the weighting mask. This example explains the reason why the normalized temperature image is taken as our weighting mask. The robust Lucas-Kanade algorithm with pixel weighting was implemented using the public domain MATLAB function shared by Dir-Jan Kroon [94].

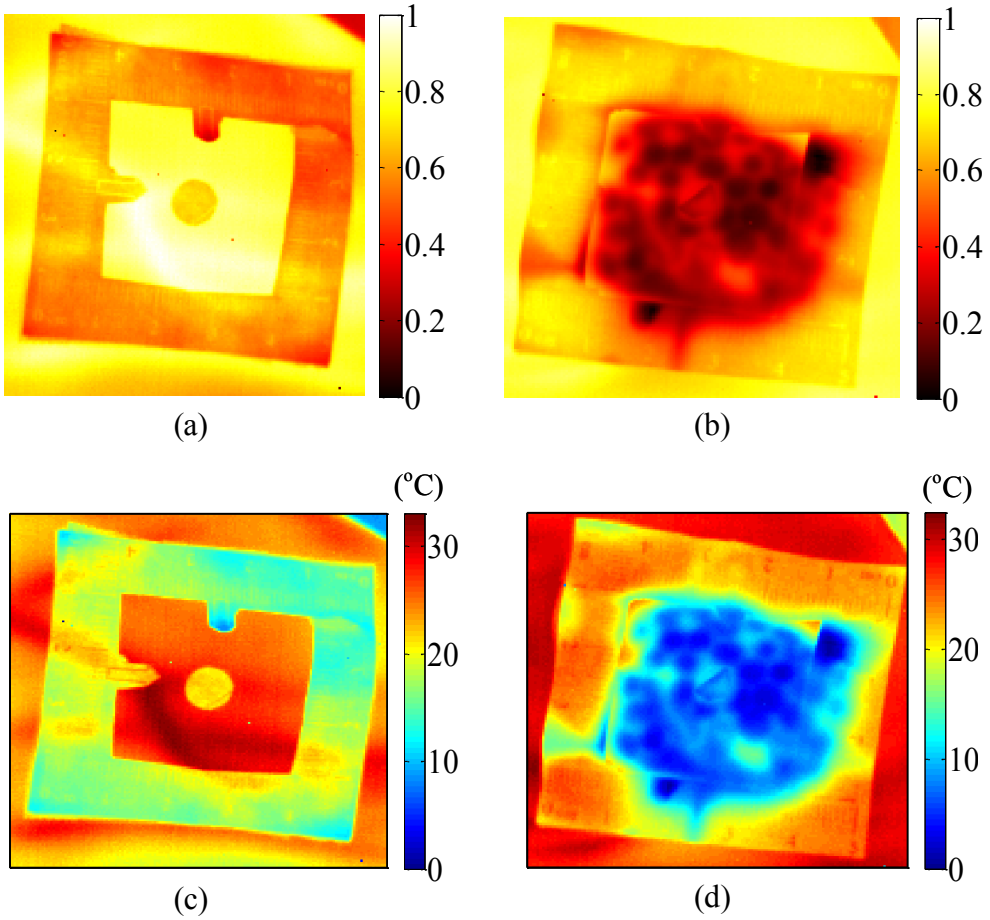


**Figure 3.4** (a) Weighting mask of the template image for the steady-state IR image sequence. (b) Weighting mask of the template image for the thermal recovery IR image sequence (created after the cooling is applied). (c) The appearance of the template images after applying the weighting masks shown in (a) for steady state analysis and (d) for the thermal recovery shown in (b).

### 3.4.7 Determining the location of the simulated lesion for tracking error analysis

In order to evaluate and quantify the tracking performance of our algorithm, we need to know the actual location of the simulated lesion (round marker) in order to be able to compare it with the estimated location determined by the motion tracking algorithm. For

this reason the simulated lesion, which is clearly visible in the IR image sequence, is used in the analysis as opposed to a real (cancerous or benign) skin lesion, which usually cannot be detected directly in the IR image. The centroid point of the simulated lesion is taken as the reference coordinate, and it is the mean value of the pixel coordinates of the marker's border. The coordinates of the border of the simulated lesion were determined using an outline segmentation algorithm – a random walk [95]. By selecting two points, one inside and one outside of the closed region of an object, the random-walk algorithm can automatically segment the object's outline. After the simulated lesion outline is delineated, its centroid location can be computed and used as the reference point.

When the tracking algorithm is applied, the centroid location (segmented in the initial frame) will be predicted in the subsequent frames based on the parameters obtained by solving Eq. (3.12). Finally, when knowing both the actual (from image segmentation) and predicted (from the tracking algorithm) centroid locations in the image sequence, the Euclidean distance between them is computed to quantify the tracking error.

In Experiment A (steady state), since no cooling is applied to the skin, the entire region of the simulated lesion is visually identifiable throughout the IR image sequence. Therefore, the outline of the simulated lesion can be directly segmented in each frame (Fig. 3.5) using the random walk algorithm.

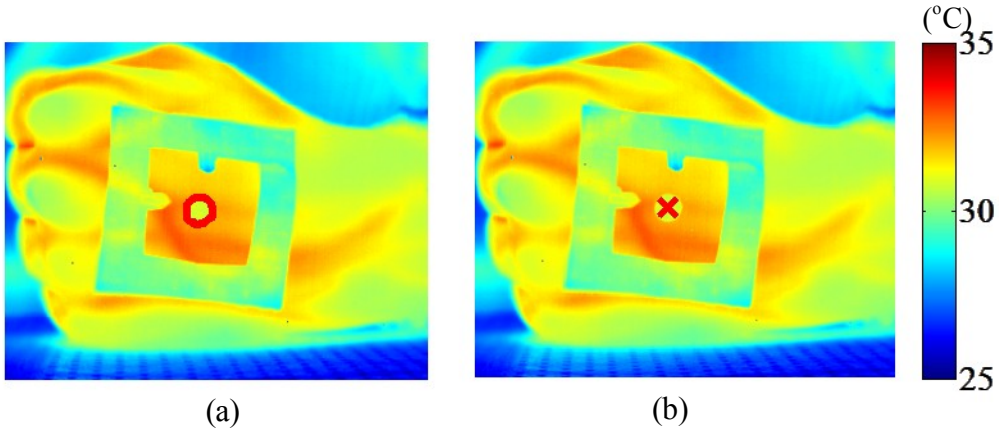


(a) (b)

**Figure 3.5** (a) Adhesive markers and the segmented outline of the simulated lesion (red circle). (b) Red cross: the centroid location of the simulated lesion.

In Experiment B (visualization of the thermal recovery) the border of the simulated lesion is obstructed (masked) by the cooling spot, therefore the region of the simulated lesion is no longer clearly visible in the IR image (Fig. 3.6(b)) and the lesion outline cannot be segmented directly. Therefore we had to apply registration between the IR images before and after cooling in order to determine the lesion outline in the thermal recovery image sequence. To accomplish this, we used the steady-state image of the simulated lesion before cooling, for which the random walk algorithm can be directly applied, to segment the outline. This lesion outline is then registered to the recovery image sequence via the location of the four corners of the square marker, which are visible in both images before and after cooling.

As shown in Fig. 3.6(a), the lesion is first segmented in the IR image before cooling. Next, by identifying the location of the four corners of the window marker in the images before and after cooling (Fig. 3.6(b)), a 2D projective transformation matrix is solved [96] based on the four corners correspondences. The identification of the four

corners can be accomplished either manually or automatically using corner-detection algorithms, such as the Harris detector [97] or the Shi & Tomasi [98] method. The registration relation between these two frames is thus established, and the lesion outline segmented in the image before cooling can be mapped into the image after cooling (Fig. 3.6(b)). By applying the registration process consecutively to individual image frames in a sequence, the actual location of the lesion centroid can be determined for each frame of the thermal recovery sequence.

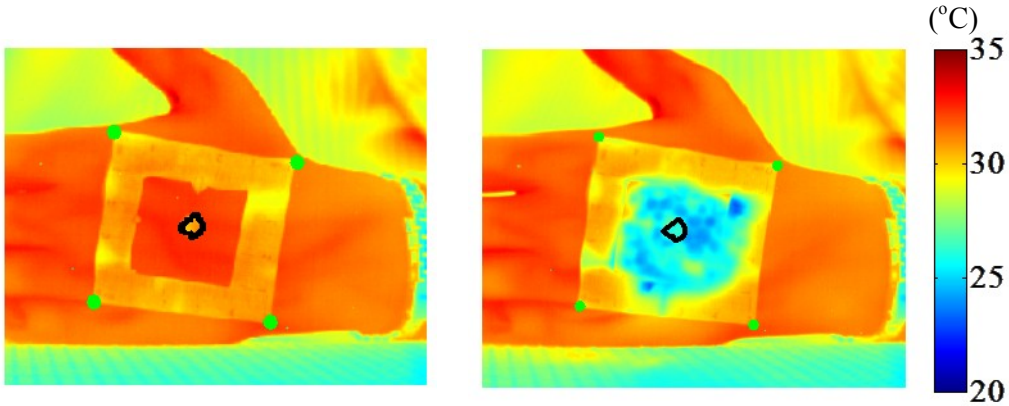


**Figure 3.6** Registration of the simulated lesion from the steady-state IR image (a) to the thermal recovery IR image (b) in Experiment B. The color change from (a) to (b) within the rectangular template is characteristic for the cooling process in dynamic IR imaging.

## 3.5 Results

### 3.5.1 Experiment A: Tracking performance for a steady-state IR image sequence

We applied the algorithm described in Section 3.4 to 23 frames of typical steady-state IR images with random in-plane motion incorporated. The tracking results, represented by 3 pairs of adjacent frames, are shown in Fig. 3.7. The magnified views of the predicted (circle) and actual (cross) locations of the simulated lesion are also shown in Fig. 3.7. As we compare the location predicted by the algorithm with the actual location measured by the segmentation, we conclude that despite the quite significant random in-plane motion, the two locations are very close to each other and the deviations are minimal.

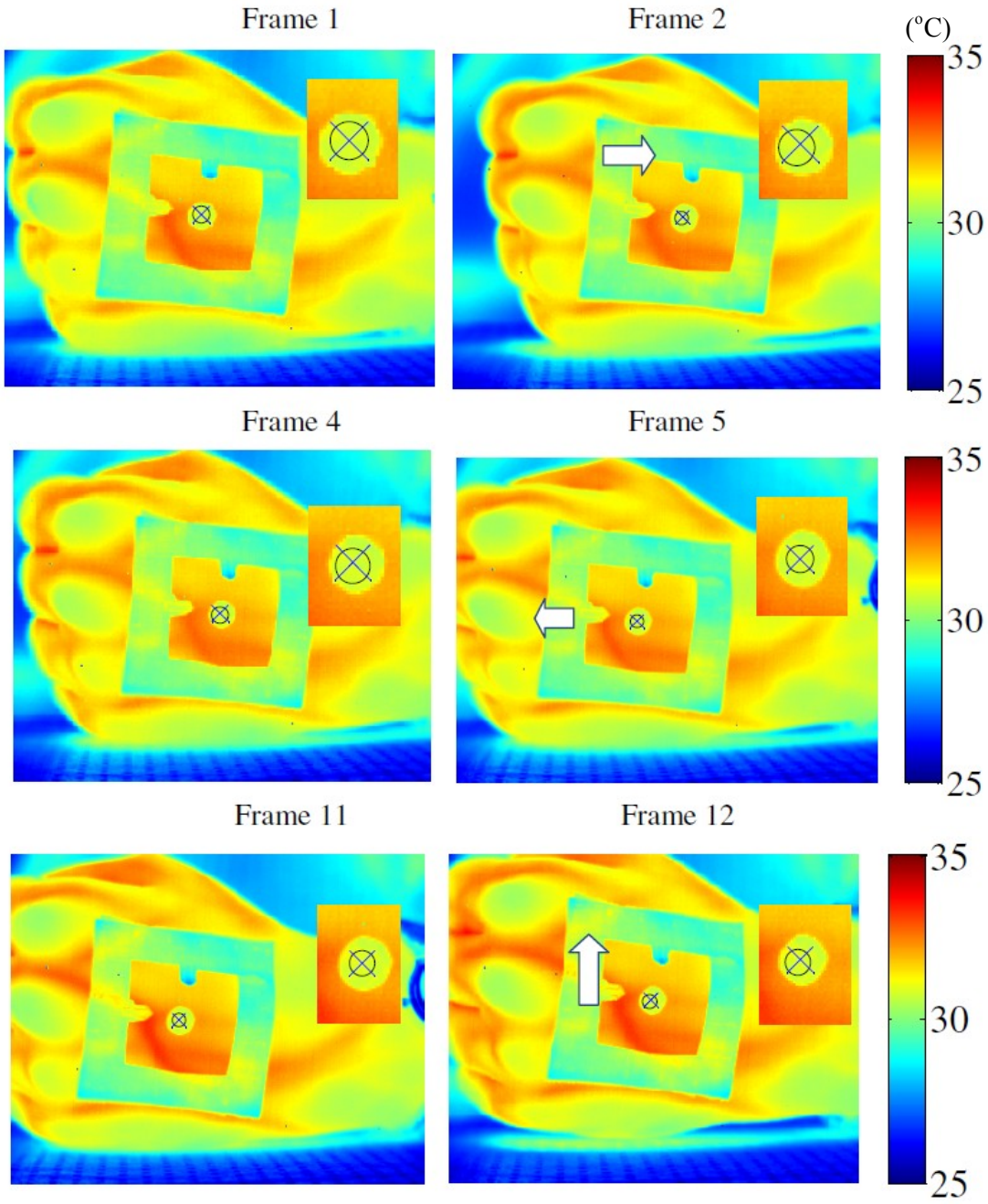


**Figure 3.7** Tracking results for Experiment A in a steady-state image sequence (circle – location of the centroid predicted by the tracking algorithm, cross – actual centroid location of the simulated lesion). The magnified view of the simulated lesion is displayed at the top right-hand corner of each image, the white arrows (right column) indicate the direction and the magnitude of the motion with respect to the previous frame (left column).

To evaluate the tracking error quantitatively, the Euclidean distance between the predicted and actual location of the lesion centroid in units of pixels is calculated for each frame, and the results are plotted as blue bars in Fig. 3.8. In addition, the displacement of the lesion centroid with resepct to the previous frame (the displacement from frame i-1 to i) is also recorded in units of pixels. As evident from Fig. 3.8, despite of the fact that the frame-to-frame displacement can exceed 35 pixels, the tracking errors over the entire image sequence are smaller than 3 pixels. This result suggests that the tracking algorithm performs very well even for relatively large in-plane motion. To translate these data into real-life dimensions, the actual size of marker is introduced: 30 mm correspond to 86 pixels in the IR image. Therefore we can infer that 1 pixel approximately corresponds to 0.35 mm on the skin surface. Using this conversion, the highest tracking errors of 3 pixels correspond to 1.05 mm in the real dimensions. The displacement of 35 pixels corresponds to approximately 11 mm motion amplitude in terms of physical dimensions, which is significant. In medical applications the motion amplitude of the subject is typically much smaller, of the order of a few millimeters. The measurement accuracy and spatial resolution can be further improved by improving the spatial resolution of the focal plane array of the camera.

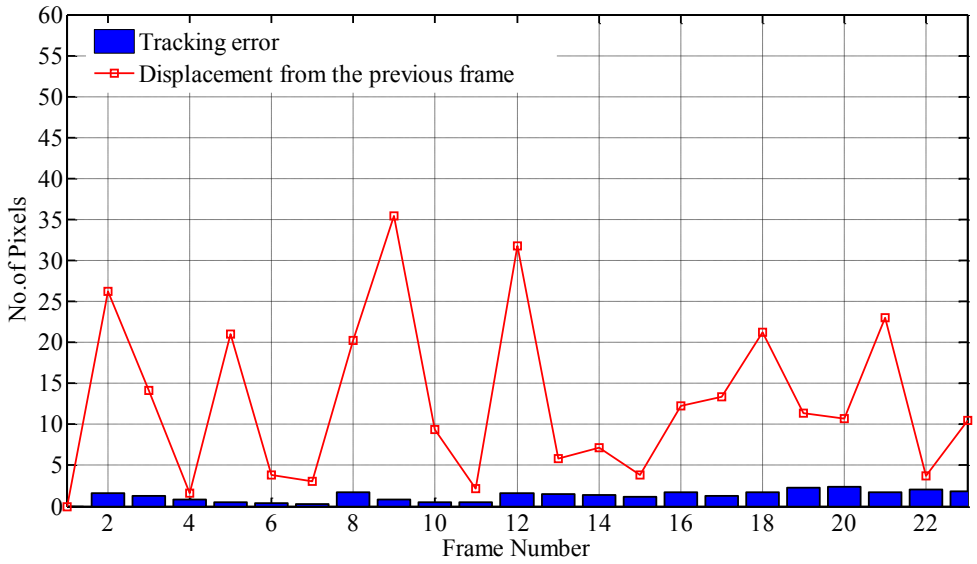


**Figure 3.8** Tracking error analysis for the steady-state image sequence in experiment A: the red line represents the frame-to-frame displacement (from frame i-1 to frame i) of the lesion centroid, and the blue bars represent the Euclidean distance between the predicted (circle center in Fig. 3.7) and actual (cross center in Fig. 3.7) location of the centroid.

### 3.5.2 Experiment B-1: Tracking performance for the thermal recovery IR image sequence (initial time interval, within 30 seconds into thermal recovery)

The tracking performance for the image sequence recovered from dynamic IR imaging with cooling is illustrated by the 3 pairs of adjacent frames in Fig. 3.9. In this trial, the first 23 IR images after the removal of the cooling excitation are considered. The frame rate is 1 frame/s, and the quantitative analysis of the tracking error at each frame is shown in Fig. 3.10. It can be observed that despite of the moderate brightness variations during thermal recovery, the lesion centroid can still be tracked with reasonable accuracy within the first 23 frames. This corresponds to 23 seconds into the thermal

recovery phase, and the highest tracking errors are smaller than 4 pixels. The results suggest that, despite of the moderate brightness variations, the template-based algorithm performs with good accuracy in the first 23 seconds into the thermal recovery sequence. This is accomplished by taking the target region in the first frame as the template image, along with its normalized image, as the weighting mask.

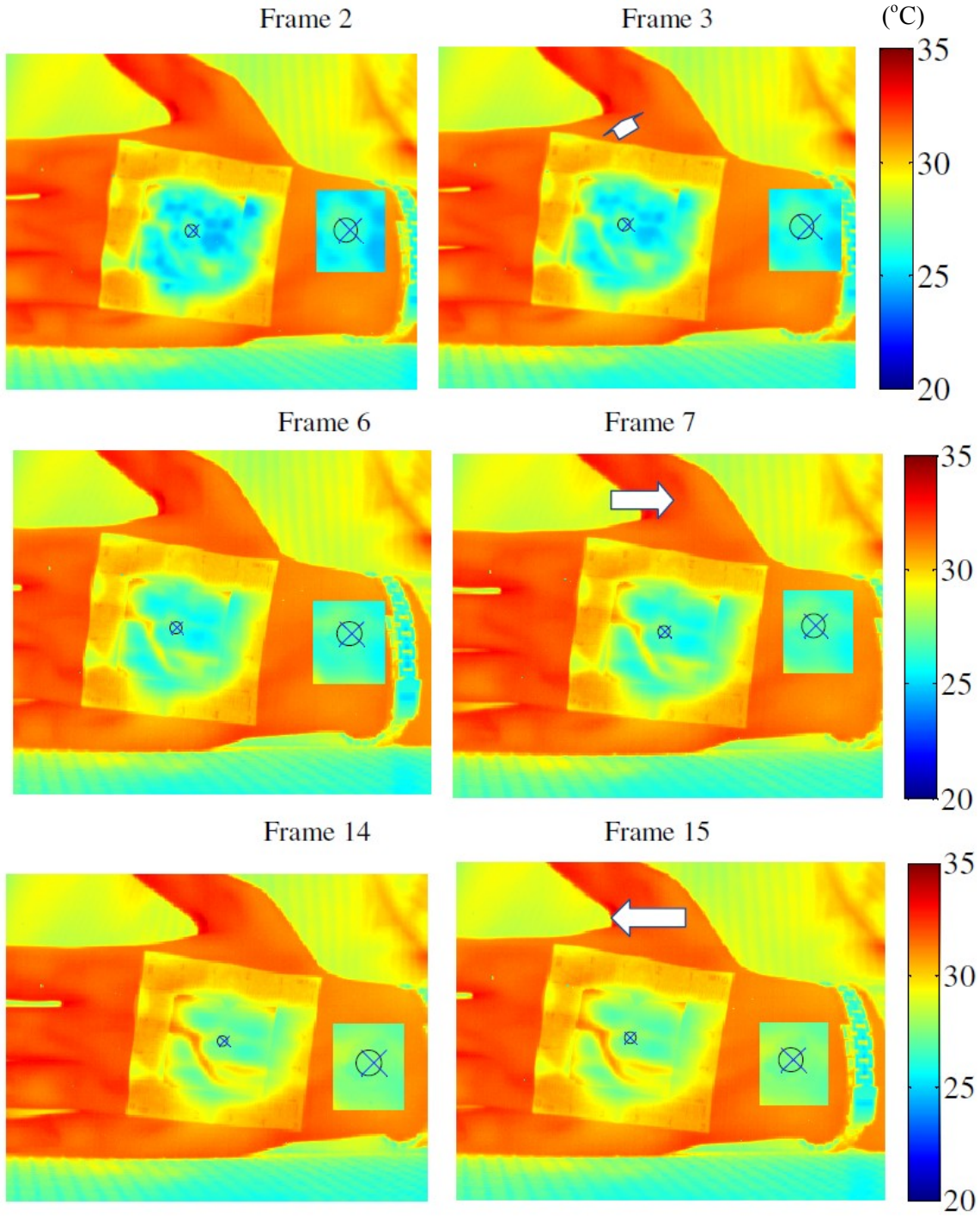


**Figure 3.9** Tracking performance of Experiment B-1 for the first 23 frames in the thermal recovery IR image sequence (circle - centroid location predicted by the tracking algorithm, cross - actual centroid location of the simulated lesion).

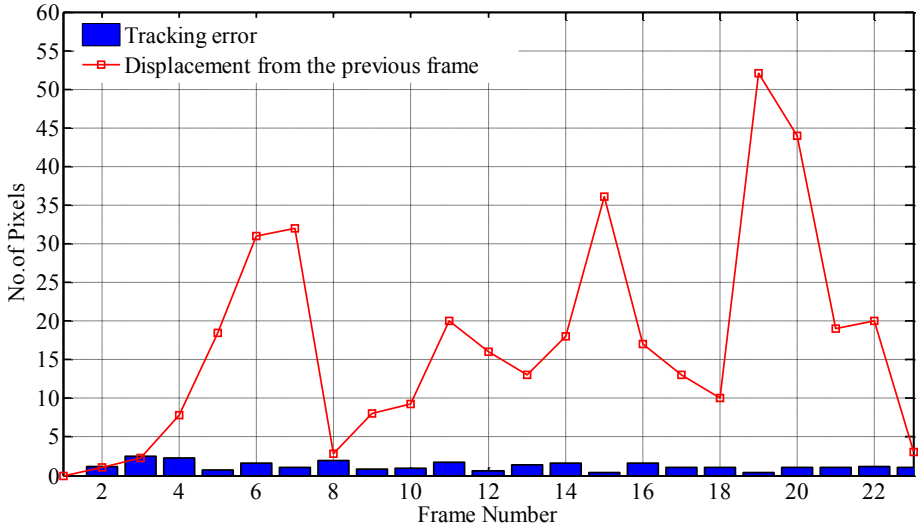


**Figure 3.10** Tracking error analysis (Experiment B-1) of the thermal recovery image sequence after the removal of cooling: the red line represents the frame-to-frame displacement (from frame i-1 to frame i) of the simulated centroid. The blue bars represent the Euclidean distance between the predicted (circle in Fig. 3.9) and actual (cross in Fig. 3.9) location of lesion centroid.

### 3.5.3 Experiment B-2: Tracking performance for the thermal recovery IR image sequence (over 30 seconds into the thermal recovery phase) without template update

As we extended the tracking test over 60 frames (1 min) in the second trial, the tracking performance of the algorithm described in Section 3.4 deteriorated. The four frames shown in Fig. 3.11(a) illustrate the dramatic changes the IR image undergoes during thermal recovery. As a consequence of these changes, the tracking algorithm gradually loses track of the simulated lesion between frames 41 and 65. The error analysis in Fig. 3.11(b) indicates a dramatic increase of tracking errors after frame 29. The significant error growth can be attributed to the brightness inconsistency beyond 30 seconds into the

thermal recovery phase and later times, when the thermal appearance of the cooled region becomes substantially different from the template image recorded at the first frame. As indicated in Fig. 3.11(b), the tracking errors exceed 5 pixels after frame 41. Therefore, to ensure the robustness the tracking method, adjustments to the template-based algorithm were needed. These adjustments are expected to deal with the brightness inconsistencies encountered during the thermal recovery.

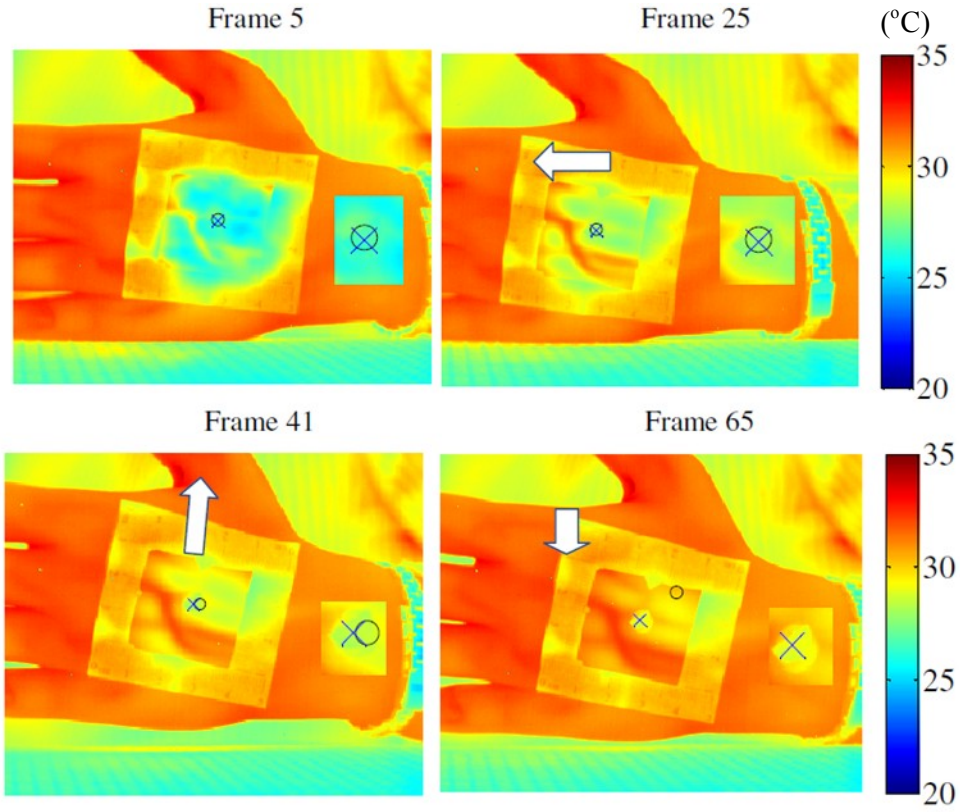


(a)

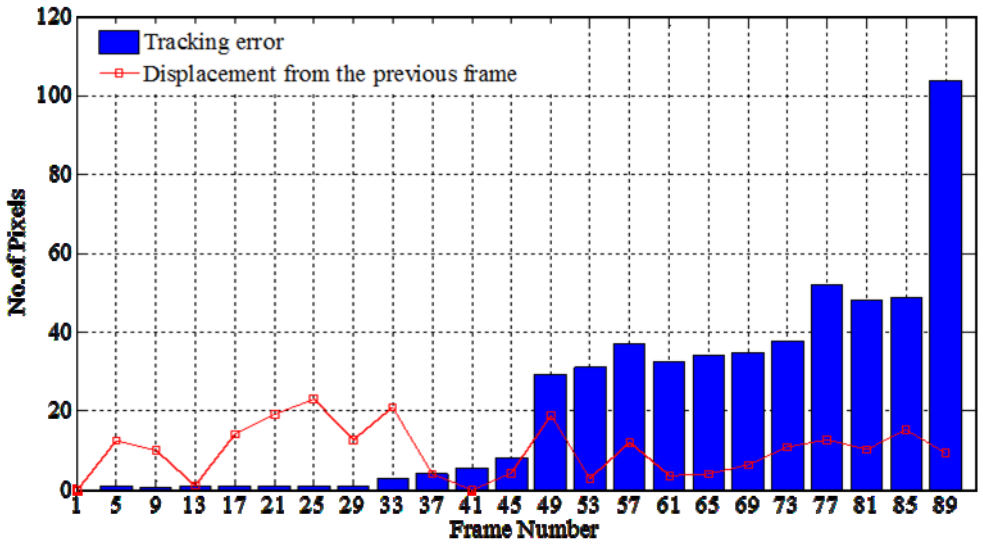


(b)

**Figure 3.11** Tracking performance for Experiment B-2 with tracking duration of 90s into the thermal recovery phase without template update. (a) Four representative image frames illustrating the differences between centroid location predicted by the algorithm and the actual lesion centroid. (b) Tracking errors and frame-to-frame displacement as a function of time.

### 3.5.4 Experiment B-3: Tracking performance of the thermal recovery IR image sequence with template update for long imaging times

To reduce the increase of tracking errors due to brightnesss inconsistency beyond 30 seconds into the thermal recovery, instead of a using single template image taken at the initial time, we update the template image and the weighting mask at frame 29 as illustrated in Fig. 3.12. Frame 29 is chosen because it is the last frame with errors smaller than 5 pixels, before significant error growth is observed in Fig. 3.11(b). This image frame has similar brightness as the rest of the frames recorded after 30 seconds. Thus the tracking procedure for longer imaging times has two stages: in the first stage the images from frames 1 to 29 are tracked using the initial template image. In the second stage, after the update at frame 29, the remaining frames are tracked using the updated template image (Fig. 3.12).

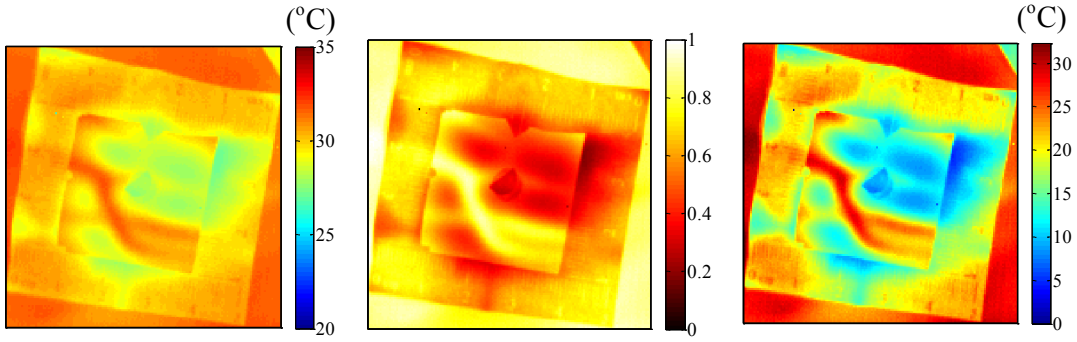


**Figure 3.12** (a) Updated template image, frame 29, (b) updated weighting mask for frame 29 and (c) resulting temperature value for the updated template image after applying the weighting mask.

The improvements achieved with the template update incorporated into the tracking algoritgm are presented in Fig. 3.13. In Fig. 3.13(a), we can observe that the simulated lesion can be tracked correctly beyond frame 30. The improved accuracy is obvious when compared with its counterpart shown in Fig. 3.11(a) (without template update). The tracking error (blue bars) and displacemnt magnitude (red line) charts for the experiment using template update are shown in Fig. 3.13(b). When compared with the data in Fig. 3.11(b), it is evident that the tracking errors are significantly reduced, under 5 pixels, thoroughout the image sequence. The results suggest that, when applying the tracking algorithm to the thermal recovery image sequence, updating the template information at one (or more) selected time instant(s) can improve the tracking robustness for longer imaging times despite the brightness inconsistencies caused by cooling.

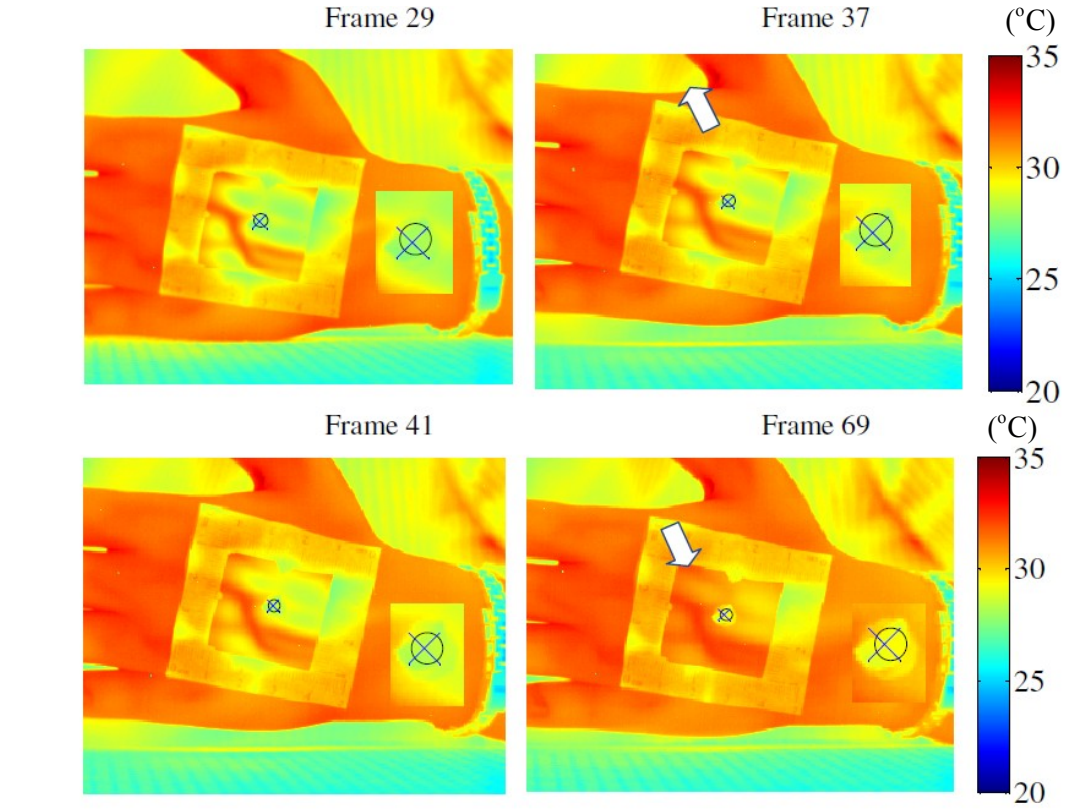


(a)

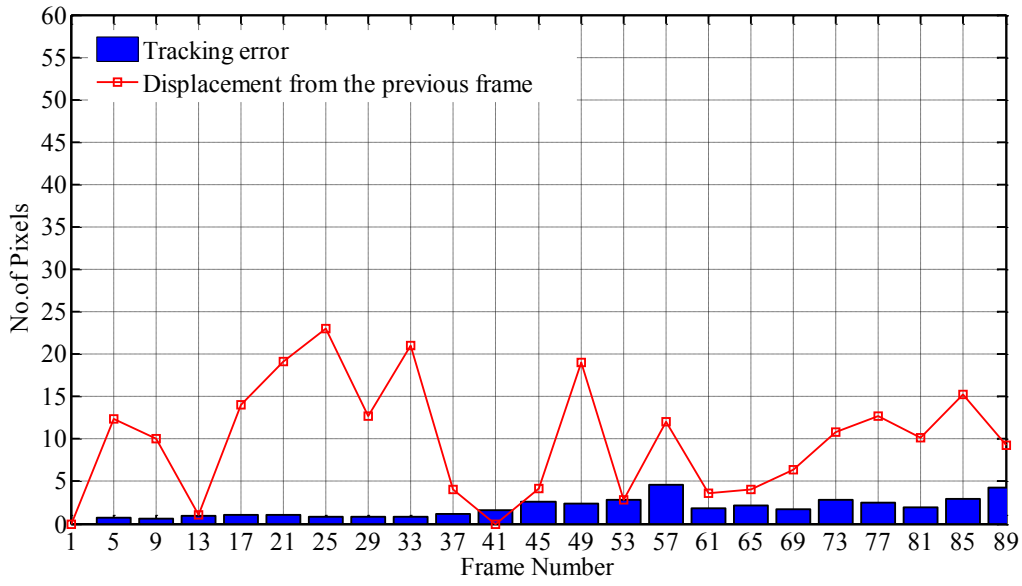


(b)

**Figure 3.13** Tracking performance of Experiment B-3 for 90 image frames with a template update carried out at frame 29: (a) Four representative frames showing the location differences between the predicted and actual lesion centroid and (b) the tracking errors at each frame along with the frame-to-frame displacement.

## 3.6 Conclusions

In this chapter, we demonstrated the feasibility of template-based algortihm for involuntary motion tracking in in-vivo infrared imaging. We demonstrated that the robust version of Lucas-Kanade algorithm can track the location of the target region in IR images sequences with good accuracy in the presence of random in-plane motion for sequences with small temperature changes (steady state). When applying the algorithm to a steady-state IR image sequence, satisfactory results were obtained when a single template information is used, detected at the first frame.

As discussed for Experiment B-1, the tracking scheme using a single template image can also achieve accurate tracking results during the first 30 seconds into the thermal recovery image sequence. The results suggest that the weighting mask, created by normalizing the template image at the initial frame, can effectively ensure the tracking robustness in the early stage of the thermal recovery phase (0-40 seconds). During this period the temporal change of skin temperature is most prominent and the thermal signaure of the lesion most pronounced [99].

As the duration of the thermal recovery exceeds 30 seconds, at later times the brightness of the cooled region differs significantly from the initial template image, which causes the tracking errors to grow significantly, as demonstrated in Experiment B-2.

From the improved tracking results obtained in Experiment B-3, we can infer that by updating the template information at the end of the early stage (around 30 seconds), tracking robustness can be ensured throughout a longer image sequence. The

approach reveals in that in dynamic IR imaging applications the template update can be an effective amendment to stabilize and improve the tracking performance of the template-based algorithm.

# Chapter 4

# Quantification of curvature-induced artifacts in infrared imaging

## 4.1 Overview

In addition to the involuntary motion of the subject discussed in Chapter 3, surface curvature can also affect the accuracy of IR surface temperature measurements. In this chapter the influence of surface curvature is studied experimentally and models for the directional emissivity are introduced. Based on experimental data, an empirical formula is derived to estimate the magnitude of the curvature artifact as a function of the viewing angle. The empirical formula as well as several models reported in the literature will be utilized to compensate for the artifacts caused by the directional emissivity in our implementation of 3D thermal mapping using IR imaging. The correction algorithm for 3D thermal mapping will be introduced and discussed in Chapter 5.

## 4.2 Background

In clinical applications, the IR camera captures infrared radiation emitted by curved skin surfaces. In spite of the relatively uniform temperature distribution over the skin surface, the curved surface will exhibit apparent temperature variations in thermography owing to the effect of skin curvature on the emissivity.

While skin emissivity, dominated by the properties of water in the infrared domain of the spectrum, is close to unity, the temperature of the surfaces oriented away from the camera axis will appear lower because of the directional properties of the emissivity. The measurement error will increase with increasing angle between the surface normal and the camera axis, the viewing angle $\theta$, and can reach several degrees Celsius, depending on imaging conditions. Therefore, one of the challenges in relating the infrared radiation emitted by the body and captured by the IR camera to temperature is the complex, three-dimensional (3D) shape of the body and its impact on the IR radiation intercepted by the focal plane array of the camera. The IR radiation captured by the focal plane array of the camera is affected by the geometry (shape and curvature), distance, skin surface properties, ambient conditions and the properties of the camera. Temperature resolution of the order of $0.1^{o}$C or better is desired in quantitative medical diagnostic applications [100], so an error of several degrees Celsius in magnitude caused by curvature artifacts is unacceptable. Therefore, in this chapter, the curvature effect is quantified experimentally, and for validation, experimental results are compared with theoretical models proposed in the literature.

## 4.3 Literature review

Due to directional properties of emissivity, curved surfaces at constant temperature (such as the skin) will exhibit apparent temperature variations in IR thermography on portions of the surface with larger viewing angles. According to the dielectric interface model, Watmough et al. [67] showed that the apparent temperature decrease due to this artifact is significant when the viewing angle exceeds 65º. The reflected radiation was taken into account in the study by Clark [101], and it showed that the measurement errors due to this artifact are likely to be proportional to the temperature difference between the skin surface and the environment. The reflected radiation is then included in the dielectric interface model by Martin and Watmough [102], which leads to better agreement between the theoretical model and experimental data. Subsequent in-vivo measurement studies [102-105] suggested that the effective emissivity reduction due to this artifact in the wavelength range of 2-5μm could be neglected when the viewing angle is smaller than 45º. The measurement error increases dramatically, reaching 2.0 -3.0 º C beyond this critical angle [102]. Hejazi and Spangler [106] developed a theoretical model of reflectivity and emissivity for human skin in the infrared wavelength range based on the non-dielectric interface assumption. This model provides an important basis to quantify the viewing angle artifact for skin in IR thermography. In view of the improved sensitivity of modern IR cameras, temperature measurement accuracy requirements for diagnostic purposes have become more rigorous: 0.1º C or better is desired for detecting skin cancer [1-8, 100]. Thus, the correction for viewing angle artifacts is crucial for the accurate quantitative diagnosis based on IR thermography standardization. To explore the

influence of the viewing angle and in order to develop tools for correcting the viewing angle artifact systematically, this chapter compares analytical results with experimental data.

## 4.4 Theory and methods

### 4.4.1 Equipment

As introduced in Section 3.4.4, the Merlin midwave (3-5 μm) infrared camera (MWIR) (FLIR Systems Inc., Wilsonville, OR) is used again in the imaging experiment (Fig. 4.1(a)). The camera is equipped with an InSb focal plane array (FPA) having dimensions of 320 × 256. It acquires 16-bit raw data at a frame rate of 60 Hz, and each image frame has the field of view (FOV) of 22 × 16 degrees. Using parameters from the flat surface black-body calibration previously conducted for the IR camera [93], the radiation intensity value in the raw image data can be converted into temperature with the sensitivity of 0.025º C. During image acquisition, the distance between the IR camera and object is set to 30 cm, same as in the black-body calibration described in [93]. The camera and data acquisition setup used in the experiment are shown in Fig. 4.1(b), and all measurements are conducted at the environment temperature of 22.6º C.

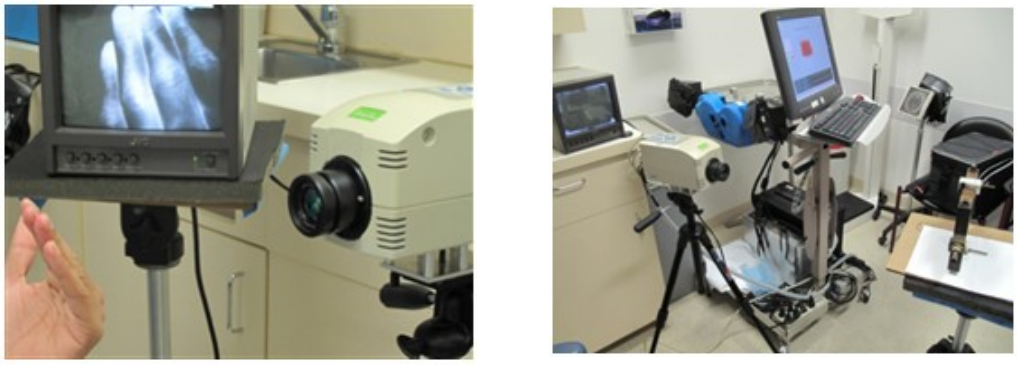

(a) (b)

**Figure 4.1** (a) The Merlin midwave infrared camera and image monitor. (b) The data acquisition setup used in the experiment**.**

(a) (b)

**Figure 4.2** (a) Copper plate used for flat surface measurements. (b) Cylindrical phantom used for curved face experiments.

### 4.4.2 Measurements on a flat surface

Before reaching the IR camera, radiation emitted by a curved surface is affected by viewing angle and travel distance, which lead to temperature variations. To investigate the influence of these two factors, a flat copper plate with dimensions 210 × 157 mm, maintained at a constant temperature of 26.4ºC with circulating water from a constant temperature water bath, is used as the imaging phantom in the first series of experiments. In the imaging session, the copper plate is first placed perpendicular with respect to the camera axis, and then rotated to capture images at five different angles in the range 10 – 60º, 10 degree increments. The rotation axis on the front surface of the flat plate is maintained at a constant distance of 30 cm from the camera. By comparing the surface temperatures measured at each rotation angle, with the distance from camera fixed, the effect of viewing angle can be isolated and presented independently. At each rotation angle, data from the central portion of the plate (rows 50 to 200 for each vertical line in the image, Fig. 4.3) are analyzed to eliminate edge effects and reduce noise. The measured 1D temperature distributions from 150 rows (along a vertical line in the image frame, with each vertical line corresponding to the same distance and same rotation angle), are averaged to yield a data point for the temperature profile along the horizontal direction. In Fig. 4.3 the temperature variation caused by the positive/negative linear distance with respect to the rotation axis is displayed.

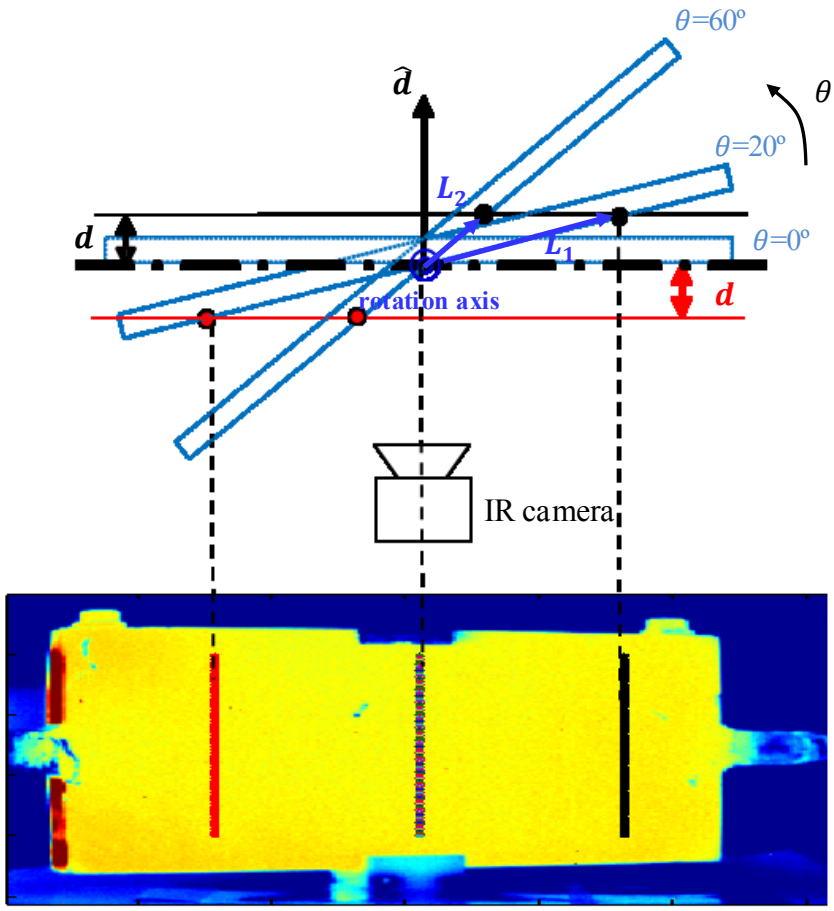


**Figure 4.3** The rotation axis of the plate and two projected vertical lines at a distance $d$ closer to (red line) and further away from (black line) from the camera in the color-coded IR image for the rotation angle of 20º. The central line is the projection of rotation axis, which lies on the plane $\hat{d} = 0$ at a distance of 30 cm away from the camera. At each rotation angle $\theta$, two lines on the phantom with fixed distance $\hat{d} = d = \pm 22.6$ mm ($\hat{d}$ taken to be positive in the direction away from the camera) are sampled for comparison, i.e. for two angles $\theta_1$ and $\theta_2$, $d$ is kept constant such that $d = L_1 sin\theta_1 = L_2 sin\theta_2$, as illustrated in the figure.

Two planes representing the distances $d = \pm$ 22.6mm (measured from the front surface of the flat plate) farther away/closer to the camera, parallel to the front surface of the flat plate (Fig. 4.3) are considered to study the effect of distance on temperature measurement accuracy. These planes are intercepted by the plate surface rotated around the rotation axis from 20º to 60º, and temperatures along the two vertical intercept lines (red and black) projected on the IR image are analyzed. Thus, by comparing the mean temperatures on these two lines with the temperature at the rotation axis for different rotation angles, the effect of distance (± 22.6mm) on temperature measurement accuracy can be isolated and examined.

### 4.4.3 Measurements on a curved surface

A cylindrical 165 mm diameter aluminum container with anodized surface (Fig. 4.2(b)) is used to investigate the curvature effect at various temperatures. During the imaging session, the container center (as shown in Fig. 4.4) is positioned on the camera axis. The viewing angle $\theta$ at any surface point is defined as the angle between its surface normal and the camera axis. The container is filled with water at temperature from 34ºC to 44ºC, and the surface image is acquired after the entire container reaches an equilibrium with the water. The temperature increment in the experiments was 2ºC.

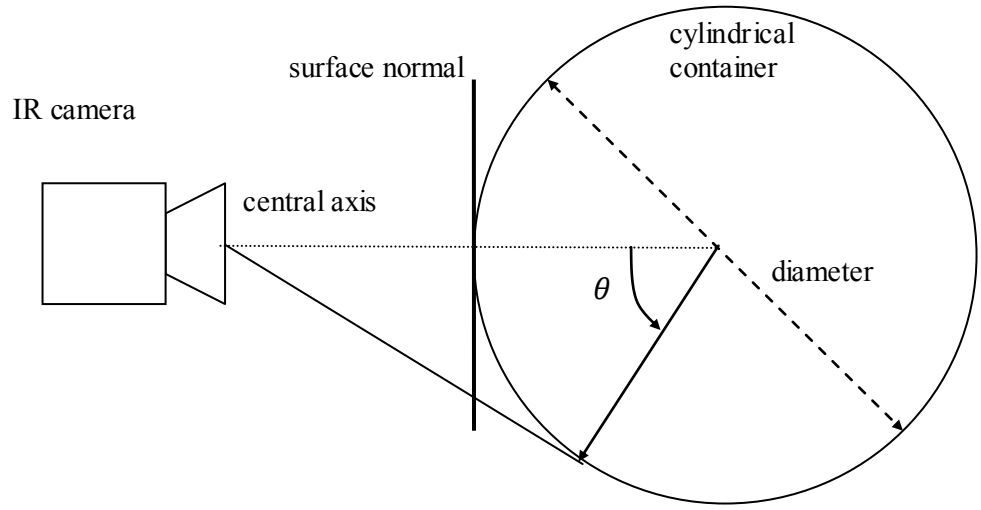


**Figure 4.4** The viewing angle $\theta$ defined for the curved surface.

### 4.4.4 Theoretical modeling of curvature effects

To better understand the behavior of directional emissivity $\varepsilon(\theta)$, we investigate the difference between our experimental results and theoretical predictions using the models of directional emissivity previously reported in Ref. [67, 106]. As addressed in Section 4.2, because of the artifact associated with directional emissivity, for any point on the curved surface, the temperature recorded by the IR detector may appear lower than the actual temperature of the surface. In the literature, there are two classical models that have been used to describe the directional emissivity of skin in the infrared spectrum, the dielectric [67] and the non-dielectric [106] models. These two models are based on different assumptions for the electromagnetic properties of skin. They provide an analytical basis to estimate skin emissivity as a function of the viewing angle $\varepsilon(\theta)$. The viewing angle $\theta$

is again defined as the angle between the surface normal and the axis of the IR camera (Fig.4.4).

### 4.4.5 The dielectric and non-dielectric models of directional emissivity

Using the index of refraction $n_s$ of a material, Watmough et al. [67] derived the expression for the directional emissivity $\varepsilon(\theta)$ as a function of viewing angle $\theta$ as

$$\varepsilon(\theta) = 1\text{-}0.5\left(\frac{\beta-\cos\theta}{\beta+\cos\theta}\right)^2 \cdot \left[1+\left(\frac{\beta cos\theta-\sin^2\theta}{\beta cos\theta+\sin^2\theta}\right)^2\right] , \quad (4.1)$$

with

$$\beta = \sqrt{{n_s}^2-\sin^2\theta} \quad . \quad (4.2)$$

Based on this model, the skin can be modeled as a dielectric material having a real component of index of refraction greater than unity with respect to air.

The non-dielectric model of directional emissivity was developed by Hejazi and Spangler [106]. In this model, skin is treated as a lossy dielectric material, and instead of the real index of refraction used for a dielectric material, the index of refraction for a non-dielectric material is modeled as a complex function

$$\boldsymbol{n_s} = n_s + jk_s, \ \boldsymbol{n_a} = n_a \ , \quad (4.3)$$

where $n_s$ and $n_a$ represent the index of refraction for skin and air, respectively. In Eq.4.3 $n_s$ and $n_a$ are the real parts, and $k_s$ is the attenuation coefficient. According to the derivation reported by Siegel and Howell [107], the directional emissivity $\varepsilon(\theta)$, which is

a function of viewing angle $\theta$, is related to the refraction indices, $n_s$ and $n_a$, and the attenuation, $k_s$ , as

$$\varepsilon(\theta) = 1 - \rho(\theta) \tag{4.4}$$

where

$$\rho(\theta) = \frac{\rho_{\parallel}(\theta)+\rho_{\perp}(\theta)}{2} \quad . \tag{4.5}$$

As shown by Hajazi and Spangler [106], the numerator in Eq.4.5 can be expressed as

$$\rho_{\perp}(\theta) = \frac{(q-n_a\cos(\theta))^2+p^2}{(q+n_a\cos(\theta))^2+p^2} \qquad \text{and} \tag{4.6}$$

$$\rho_{\parallel}(\theta) = \frac{[(n_s^2-k_s^2)cos\theta-n_a q]^2+[2n_s k_s cos\theta-n_a p]^2}{[(n_s^2-k_s^2)cos\theta+n_a q]^2+[2n_s k_s cos\theta+n_a p]^2} \quad , \tag{4.7}$$

where

$$p^2 = \frac{1}{2}[-n_s^2 + k_s^2 + n_a^2 sin^2\theta] + \frac{1}{2}\sqrt{4n_s^2k_s^2 + (n_s^2 - k_s^2 - n_a^2 sin^2\theta)^2} \tag{4.8}$$

$$q^2 = \frac{1}{2}[n_s^2 - k_s^2 - n_a^2 sin^2\theta] + \frac{1}{2}\sqrt{4n_s^2k_s^2 + (n_s^2 - k_s^2 - n_a^2 sin^2\theta)^2} \tag{4.9}$$

## 4.4.6 Modeling of the directional emissivity of skin

When the skin surface is normal to the camera axis with a viewing angle $\theta = 0^{\circ}$, the skin emissivity $\varepsilon_0$ is in the range of $0.98 \pm 0.01$ in the infrared spectrum range of 2-14 μm [65-

67]. By adopting this as the nominal value of emissivity $\varepsilon_0$ along with the optical properties of skin from Ref. [106], we can model the directional emissivity of the skin using the two models introduced in Sec.4.4.4. In addition, we modeled the directional emissivity $\varepsilon(\theta)$ using the cosine function as $\varepsilon(\theta) = \varepsilon_0 \cos\theta$ for reference. This simplified expression is commonly used to describe the directional emissivity of an object when adequate, more accurate models are unavailable. The parameters used for these three models are summarized in Table 4.1, and the resulting directional emissivity plots are contrasted in Fig.4.5.

**Table 4.1** Parameters used for modeling the directional emissivity of skin

| | |
|---|---|
| Dielectric model [67] | $n_s = 1.33$ |
| Non-dielectric model [106] | $n_s = 1.33,\ k_s = 0.25,\ n_a$=1 |
| Cosine model[65-67] | $\varepsilon_0 = 0.98$ |

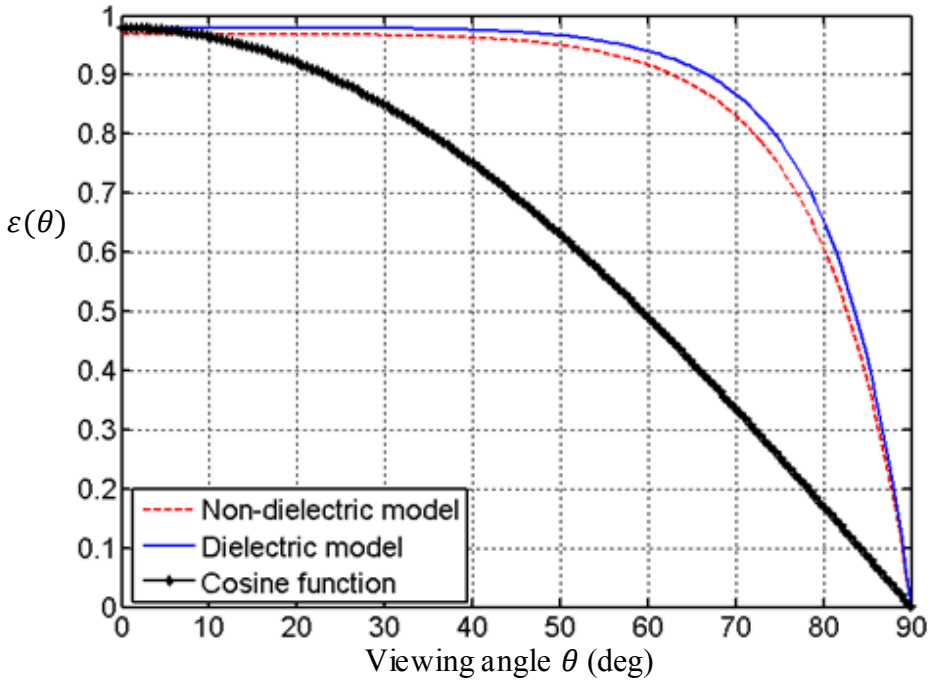


(a)

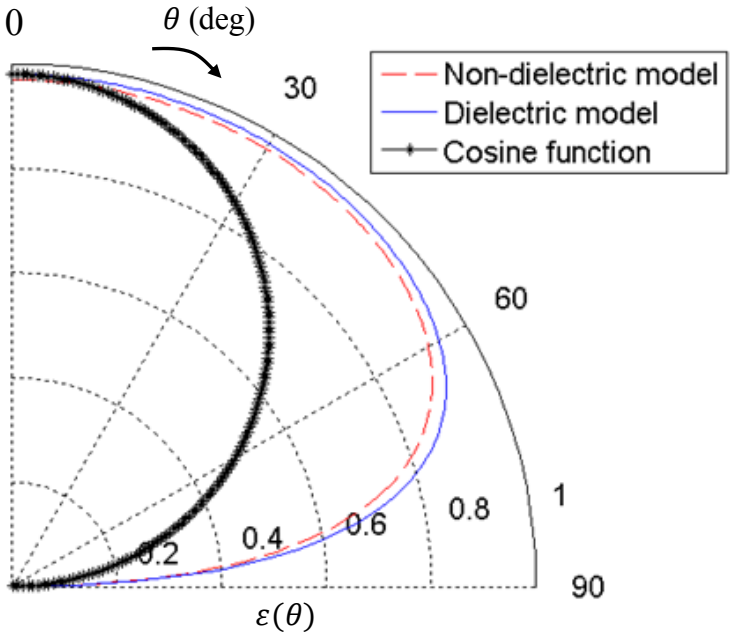


(b)

**Figure 4.5** Directional emissivity of the skin $\varepsilon(\theta)$ plotted as a function of the viewing angle using the dielectric model [67], the non-dielectric model [106], and the cosine function: (a) Cartesian plot and (b) polar plot.

### 4.4.7 Model validation for the directional emissivity of skin

Considering the fact that the optical properties of skin in the infrared spectrum are dominated by pure water, we used the wavelength-dependent refractive index of pure water at 310 K (body temperature) to validate directional emissivity values of skin computed by the dielectric and non-dielectric models in the previous section. We acquired refractive index [$n_\lambda$ , $k_\lambda$] data in two wavelength ranges, : $\lambda$ = 3-5 μm and $\lambda$=7.5-13.5 μm, which match the spectral ranges detected by the two IR cameras used in this thesis (see Sections 4.4.1 and 5.3.1 for details). The refractive index at each wavelength is obtained using the classical oscillator model developed by The Johns Hopkins University Applied Physics Laboratory (APL) [108, 109] and the optical properties of pure water in Ref. [110] . The values of the refractive index [$n_\lambda$ , $k_\lambda$] at each wavelength $\lambda$ were then taken as [$n_s$ , $k_s$] in the non-dielectric model [106]. Multiple plots of the directional emissivity function, for pure water $\varepsilon_\lambda(\theta)$ were generated, one for each wavelength within the wavelength range of interest, as presented by the green curves in Figs. 4.6(a) and (b). The directional emissivities of skin computed by the dielectric and non-dielectric models (Fig.4.5 and Table 4.1) are also plotted in Figs.4.6 (a) and (b) for comparison. Figs. 4.6 (a) and (b) demonstrate that the directional emissivity of skin computed by both dielectric and non-dielectric models agrees well with that of pure water in these two spectral ranges.

The validation suggests that under conditions (temperature and wavelength) characteristic of our applications, both dielectric and non-dielectric models can provide reasonable approximation for the directional emissivity of the skin.

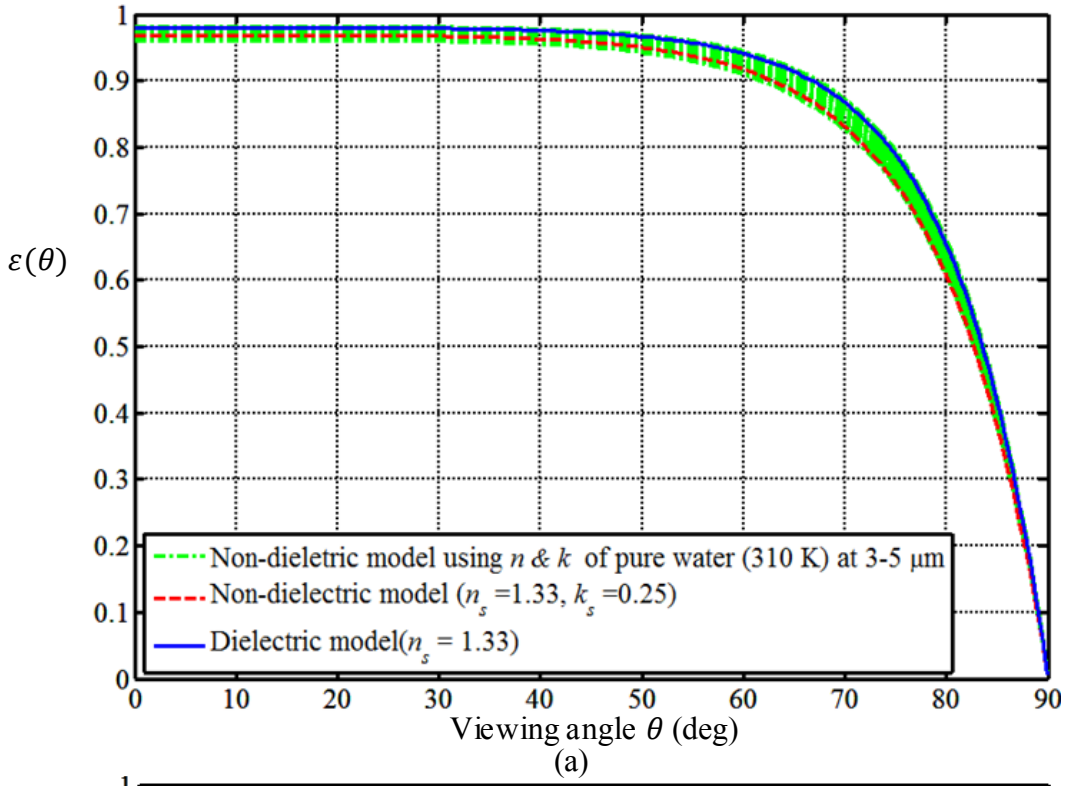


(a)

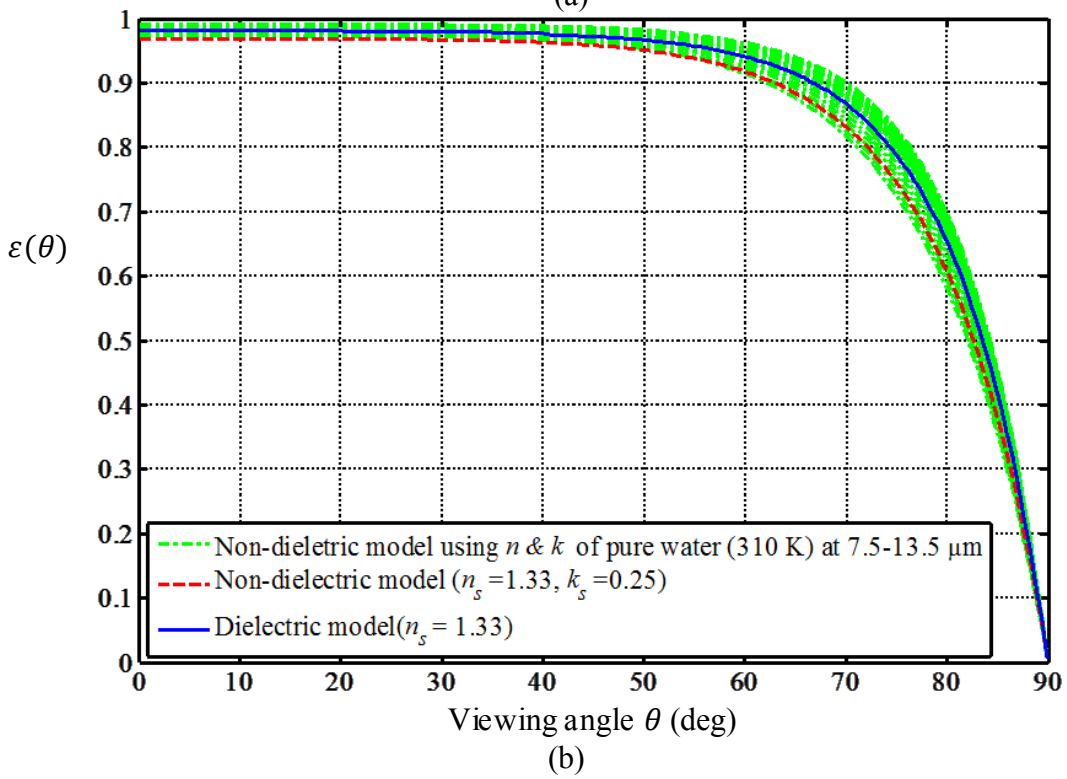


(b)

**Figure 4.6** Directional emissivity of skin computed by the dielectric/non-dielectric models (blue and red curves) and for pure water at 310 K (using appropriate wavelength-dependent refractive index values and the non-dielectric model) for two infrared spectral ranges: (a) 3-5 μm and (b) 7.5-13.5 μm.

### 4.4.8 Directional emissivity of anodized aluminum

To compare the experimental results (Sec.4.4.3) with theoretical predictions, we computed the directional emissivity of the anodized aluminum surface used in our experiment by the two models introduced in Sec.4.4.4 using the optical properties of anodized aluminum[111]. In the dielectric model, we set $n_s$=2.84, which leads to the nominal emissivity $\varepsilon_0$ =0.77 [111] of anodized aluminum at normal orientation ($\theta$= 0). In the non-dielectric model, the nominal emissivity of $\varepsilon_0$ =0.77 is used again, and the values $n_s$=2.84 and $k_s$ =0.0003 were assumed based on the Ref. [112]. The refractive index of air $n_a$ is set to 1. The computed results for anodized aluminum are presented with the experimental data in Sec.4.5.2.

## 4.5 Experimental results

### 4.5.1 Imaging experiments with the flat- surface phantom

Fig. 4.7 displays averaged temperatures along the rotation axis at rotation angles from 0º to 60º. It can be observed that the temperature decrease due to viewing angle effect is not noticeable until the angle reaches 40º. A more pronounced decrease of around 0.2 ºC can be observed for viewing angles of 40º to 60º, and this phenomenon is in agreement with the results published previously [102, 113].

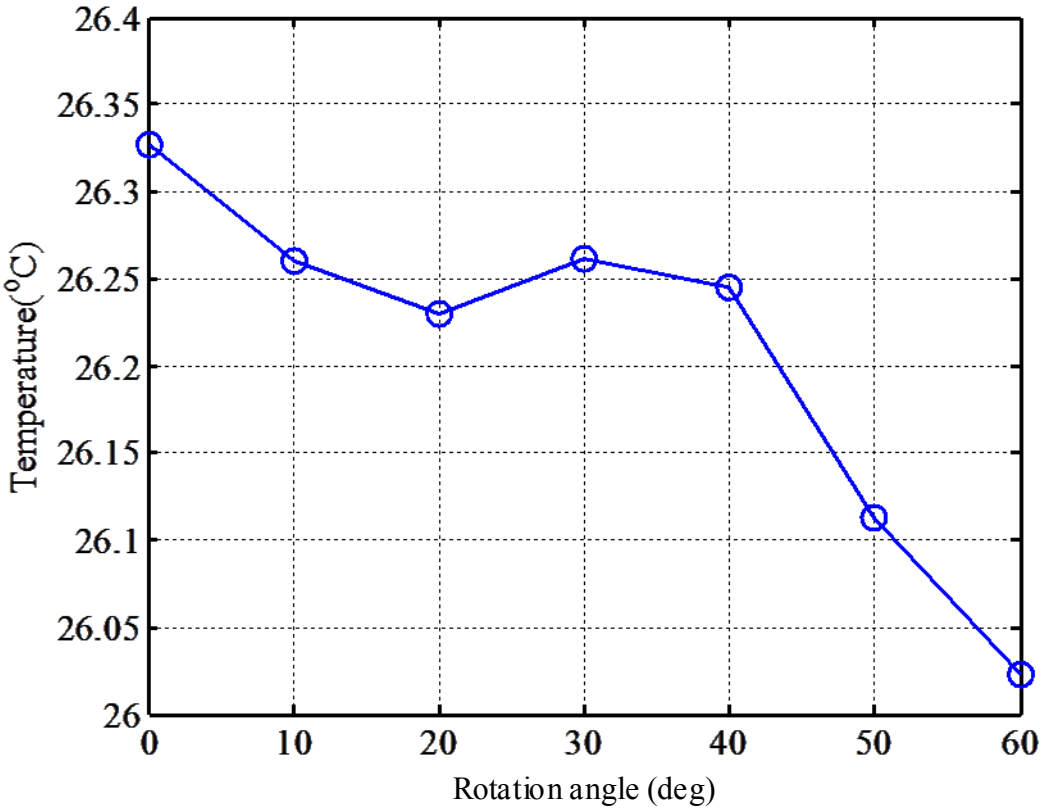


**Figure 4.7** The averaged temperature on the flat surface along the rotation axis for rotation angles from 0º to 60 º.

Averaged temperature profiles along a line perpendicular to the rotation axis at rotation angles of 30º, 40º, 50º and 60º are illustrated in Fig. 4.8. In these plots, the effect of travel distance can be demonstrated for each viewing angle. The results demonstrate that temperature differences caused by the distance shift become more prominent when the angle exceeds 50º. The temperature appears higher on the left hand side portion of the plate, which is closer to the camera, and lower towards the right hand side, for larger distances from the camera. The measured temperature difference between the left and right end of the plate is 0.12 ºC for 60º rotation angle.

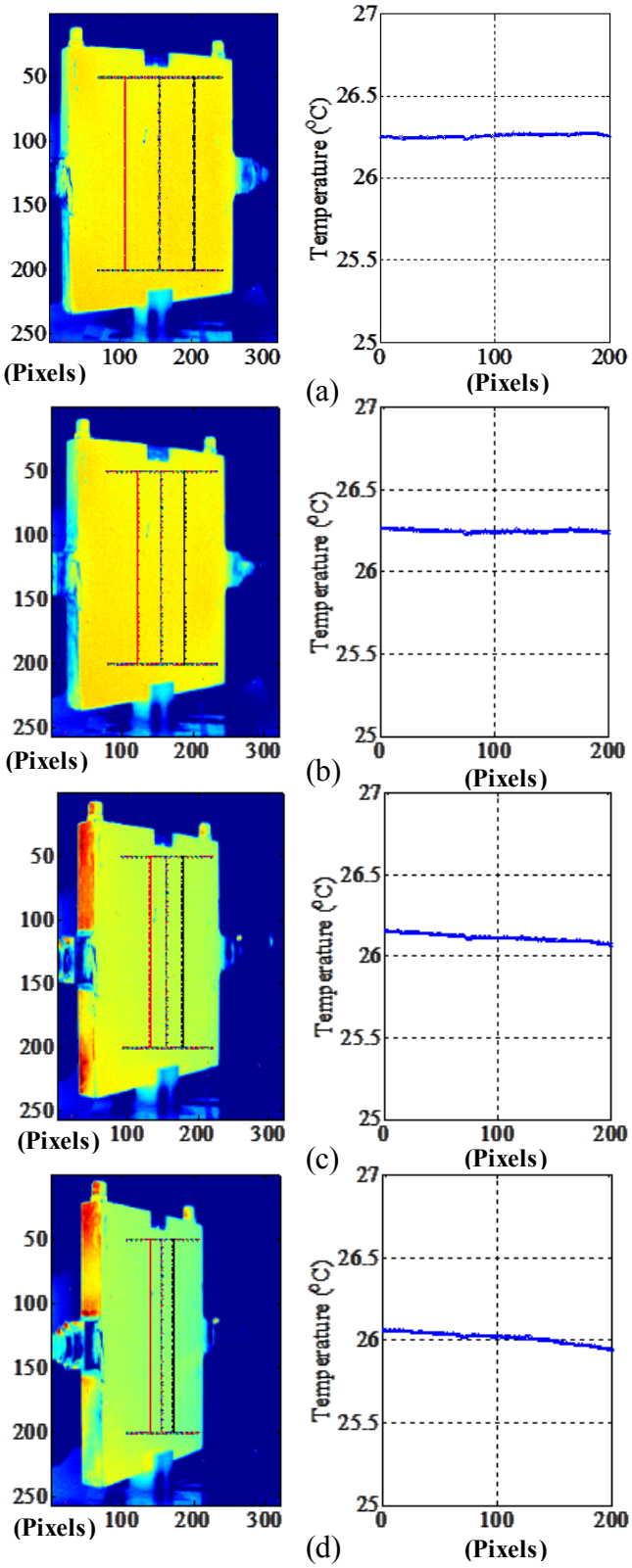


**Figure 4.8** Color-coded infrared image of the flat plate and average temperature along a line perpendicular to the rotation axis on the flat surface rotated by (a) 30 ° , (b) 40 ° , (c) 50 ° and (d) 60 °.

Considering both viewing angle and distance factors simultaneously, the temperature as a function of the viewing angle is plotted in Fig.4.9. The three curves represent the mean temperature along the three vertical lines (black, blue, red) at different travel distances of 30+2.26 cm ($d$=22.6 mm), 30 cm ($d$=0) , and 30-2.26 cm ($d$= −22.6 mm), respectively.

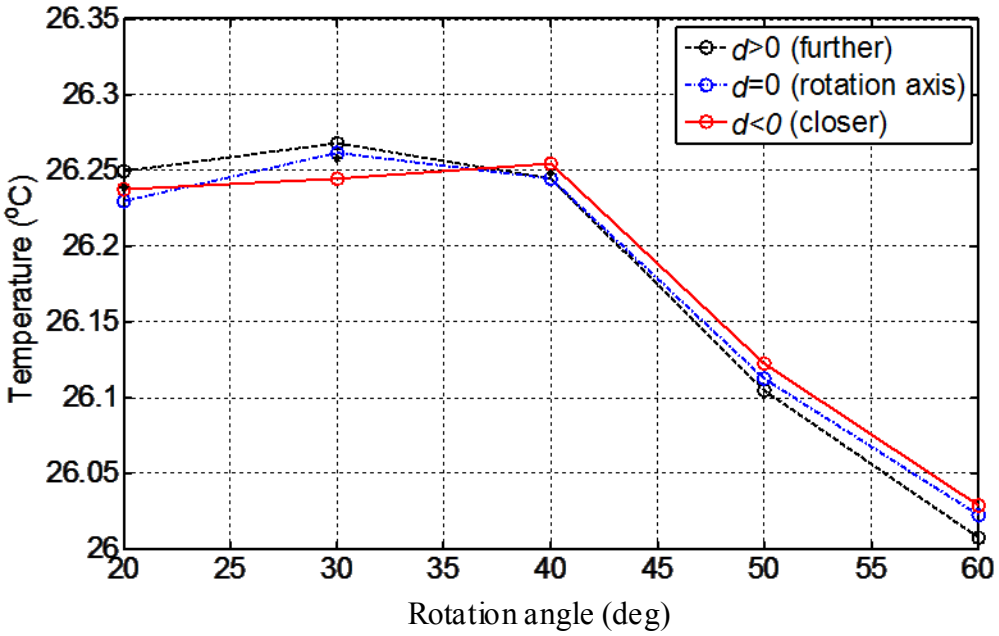


**Figure 4.9** Influence of the rotation angle on the temperature at three fixed travel distances relative to the rotation axis (black, $d$ =22.6 mm >0 further away from the camera than the rotation axis; blue, $d$=0, the rotation axis; red, $d$ =−22.6mm <0, closer to the camera than the rotation axis)

It can be inferred that neither the rotation angle nor the travel distance influence the temperature measurement significantly for rotation angles below 40º. Once the rotation angle exceeds 40º, the temperature variation due to both factors is more pronounced. At angle 60º, a clearer divergence due to distance shift (further/closer) can be observed among the three curves. The temperature deviation is in the range of 0.05º C.

### 4.5.2 Imaging experiments for the phantom with curved surface

Color coded IR images of the metal cylinder filled with warm water are shown in Fig. 4.10(a). The margins of the area sampled for analysis are marked by four lines; the two lines on the left and right hand sides indicate the range for which viewing angle is considered. The top and bottom lines encompass the horizontal region for averaging. The variation caused by viewing angle is shown in Fig. 4.10(b) for various surface temperatures. It can be observed that the temperature begins to drop slightly when the viewing angle is between 40º and 60º. However, when the viewing angle is larger than 60º, the temperature drop becomes more significant, and the trend is consistent for all temperatures. These results agree with the theoretical prediction by Martin and Watmough [102].

As proposed by Clark [101], if we take the temperature difference between the curved surface and the environment into account, at the shorter wavelengths, the measurement error of object temperature due to its directional emissivity can be estimated by the linearized relation for small temperature intervals [101] as

$$\Delta T^c \equiv \frac{T_s - T(\theta)}{T_s - T_a} = \frac{\Delta T}{T_s - T_a} = C(1 - \varepsilon(\theta)) , \qquad (4.10)$$

where $\Delta T^c$ is the dimensionless form (in the range 0-1) of the temperature decrease detected in IR image. In Eq. 4.10 $\Delta T$ is the temperature difference between the actual temperature of the surface $T_s$ and the measured temperature at the viewing angle $\theta$, $T(\theta)$. $\Delta T^c$ is calculated by normalizing $\Delta T$ with respect to the difference between the actual

temperature, $T_s$ and the ambient temperature of the imaging environment $T_a$. On the right hand side of Eq. (4.10), $\varepsilon(\theta)$ is the directional emissivity at viewing angle $\theta$, and $C$ is the constant representing the linear relation between $\Delta T^c$ and $(1-\varepsilon(\theta))$. As shown in Eq. (4.10), Clark [101] indicated that the measurement error $\Delta T$ is proportional to two factors: 1. the temperature difference between the surface and ambient, and 2. the deviation of emissivity from unity. In the cylindrical phantom experiment using anodized aluminum, we assume that the water temperature (34ºC - 44ºC) corresponds to the surface temperature $T_s$, and $T_a$ = 22.63ºC. With the measured temperature, $T(\theta)$, in the IR image, we can obtain $\Delta T^c = T_s - T(\theta)/T_s - T_a$ for the six water temperatures used in the experiment, and the results are plotted with respect to the viewing angle $\theta$ in Fig.4.11 (a).

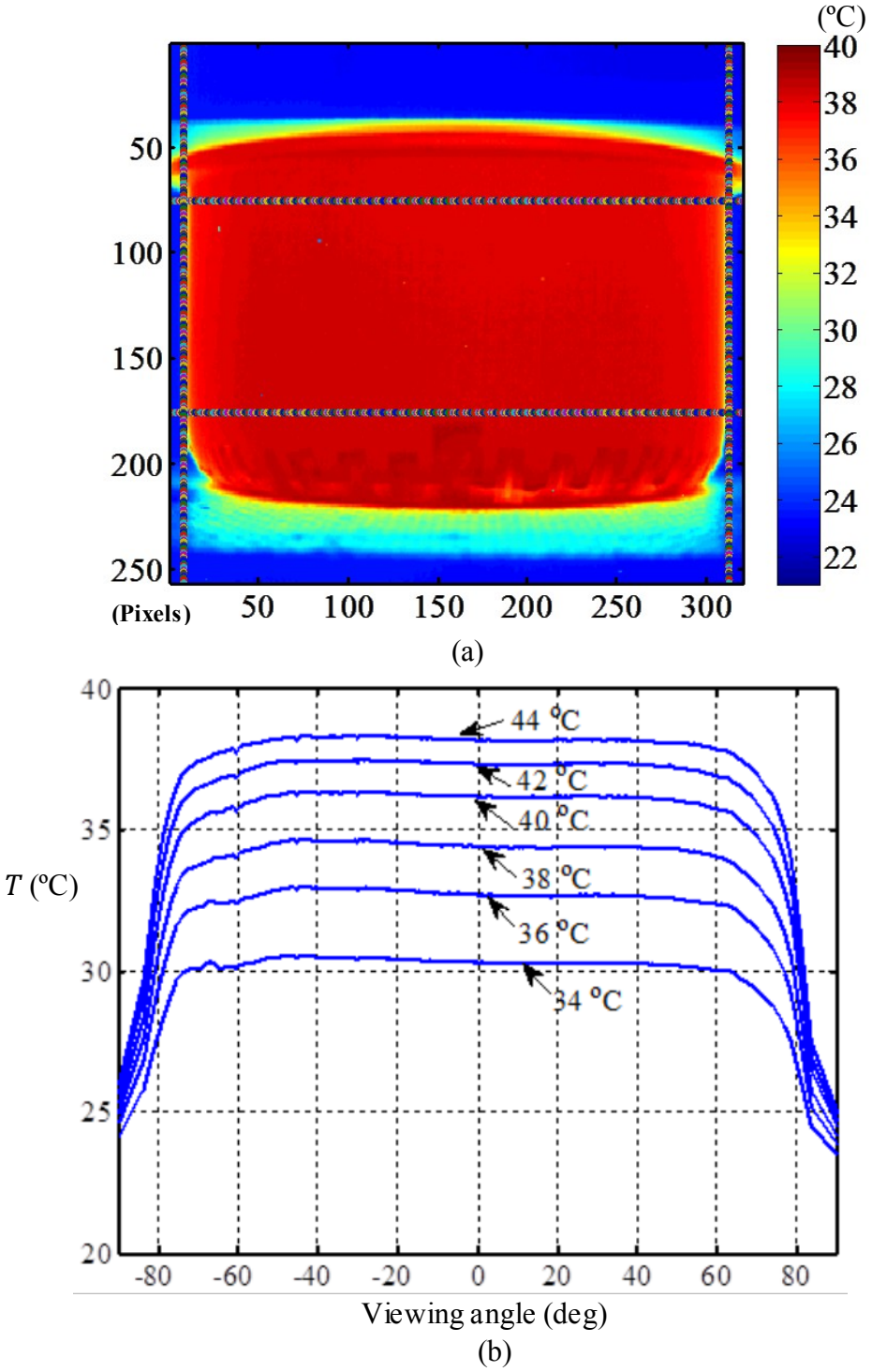


**Figure 4.10** (a) Color-coded IR image of the cylindrical curved surface (water temperature = 44ºC) with marked margins indicating the region for analysis. (b) Averaged temperature (in the region enclosed by the upper and bottom lines) as function of the viewing angle for angles from 0º to ±90º and 6 surface temperatures.

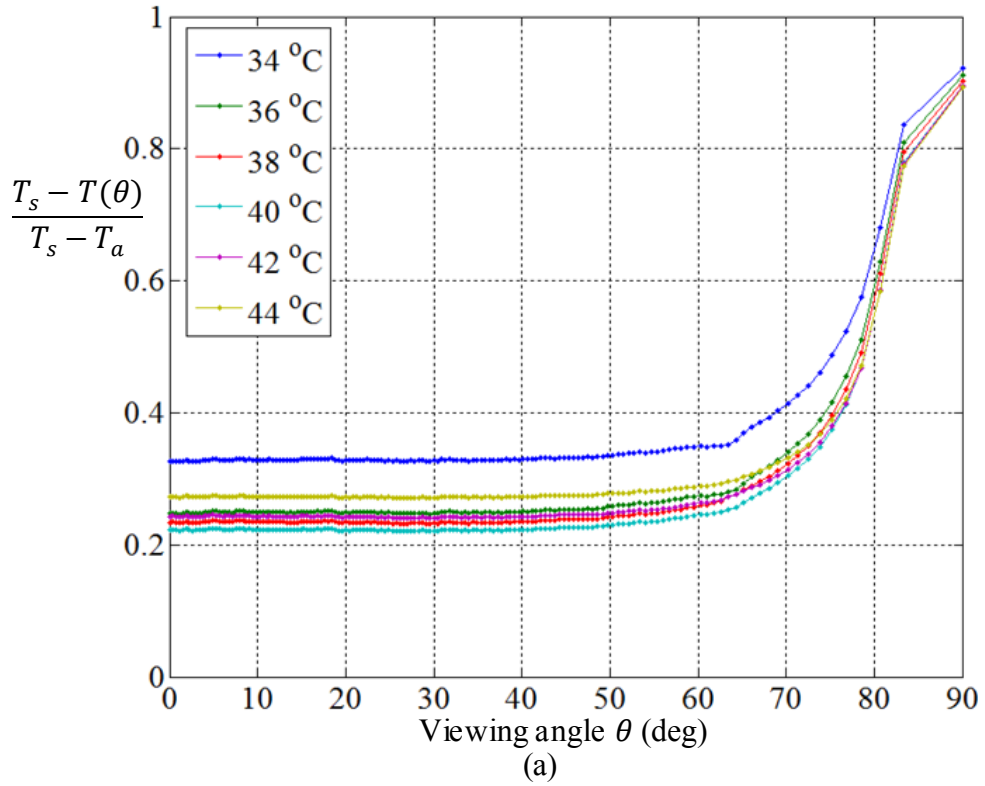


(a)

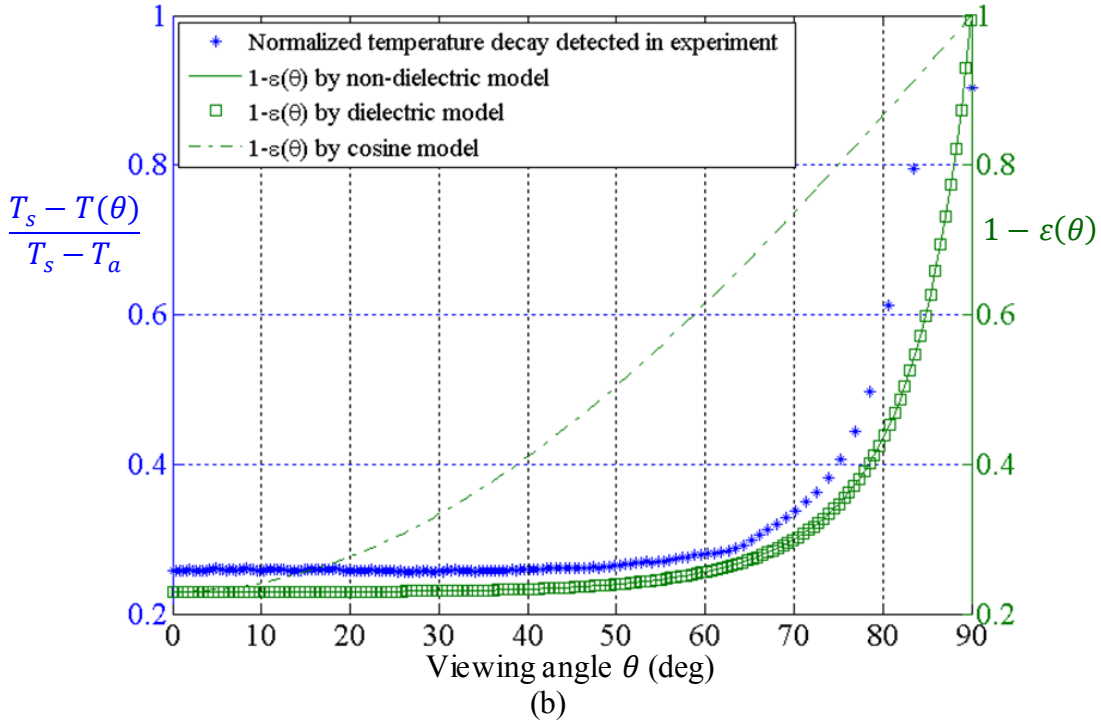


(b)

**Figure 4.11** (a) Dimensionless measurement error defined by equation (4.10) as function of the viewing angle for six water temperatures. (b) Mean value of the measurement error for the six temperatures (left axis) used in curved-surface phantom experiment and the computed value of $1 - \varepsilon(\theta)$ (right axis) as function of the viewing angle.

To validate the relation proposed by Clark [101], Eq.(4.10), we computed the mean value of $\Delta T^c = T_s - T(\theta)/T_s - T_a$ for the six temperatures considered in this study and plot the results in Fig.4.11(b). In the same plot, the values $1 - \varepsilon(\theta)$ computed using the three models for directional emissivity $\varepsilon(\theta)$ (dielectric, non-dielectric, and cosine models), are also plotted in Fig.4.11(b) for comparison.

The combined results in Fig.4.11(b) suggest that the mean value of $\Delta T^c$ (blue data points) matches very well the theoretical prediction for $1 - \varepsilon(\theta)$ computed using the dielectric and non-dielectric models. The plots obtained using the dielectric and non-dielectric models are nearly identical when the optical properties of anodized aluminum are used in the model. Therefore, the observed agreement between experimental $\Delta T^c$ and $1 - \varepsilon(\theta)$ predicted by dielectric and non-dielectric models supports the linear approximation proposed by Clark [101] (Eq. (4.10)). In contrast, such agreement cannot be observed between $\Delta T^c$ and the $1 - \varepsilon(\theta)$ that is predicted by the cosine model. For $\theta$ greater than 10 degrees the cosine substantially overestimates the decrease of emissivity caused by viewing angle, as shown in Fig.4.11(b),.

If we replace the surface temperature $T_s$ with the temperature measured using IR imaging viewed normal in Eq.(4.10) instead of the water temperature used in the previous analysis, the measurement error over the curved surface can be normalized in the range (0,1) as

$$\Delta T^* = \frac{T_n - T(\theta)}{T_n - T_a} . \tag{4.11}$$

In Eq.(4.11), $T_n$ is the measured temperature viewed normal to the surface, i.e., the measured value at the central point of the curved surface where the viewing angle with respect to the camera axis is 0º. The normalized measurement error from these experiments is plotted in Fig. 4.12.

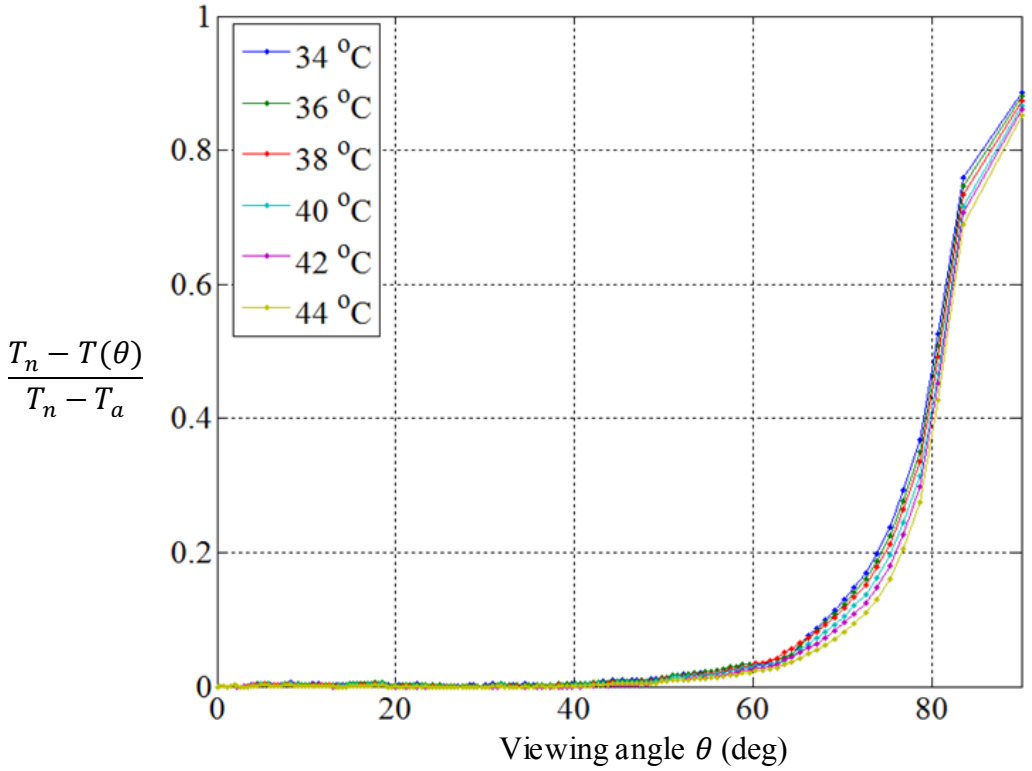


**Figure 4.12** The normalized temperature error $\Delta T^*$ over the viewing angle: 0º to 90º at 6 surface temperatures.

The results in Fig.4.12 indicate that $\Delta T^*$ deviates from 0 at 40º, and the six curves rapidly converge when the angle is greater than 80º. A similar dependence of $\Delta T^*$ on the viewing angle for these six temperatures is observed. We can also conclude that viewing angles between 65º and 80º are most sensitive to the difference between surface and ambient temperature.

### 4.5.3 Derivation of empirical formula for temperature correction

To quantify the relationship between the temperature detected in the IR image and the directional emissivity, we derive a mathematical model based on Eq.(4.11) [101]. Based on the similarity between computational results (Eq.(4.10)) and experiment (Fig.4.11(b)), with the constant *C* assumed to be 1 in Eq.(4.10), we formulate the similarity relationship as

$$\Delta T^c \equiv \frac{T_s - T(\theta)}{T_s - T_a} = \frac{\Delta T}{T_s - T_a} \sim 1 - \varepsilon(\theta) \ , \tag{4.12}$$

where $\Delta T = T_s - T(\theta)$ denotes the difference between the actual and detected temperatures at the viewing angle $\theta$. The experimental results for $\Delta T$ and $\Delta T^c$ as a function of the viewing angle $\theta$ are plotted in Figures 4.13 (a) and (b), respectively. Thus, using the approximation described by Eq. (4.10), we can derive an empirical correlation to estimate the temperature measurement error, $\Delta T$. By knowing the directional emissivity $\varepsilon(\theta)$, the temperature $T(\theta)$ detected in the IR image, and the difference between the actual temperature $T_s$ and the ambient temperature $T_a$, $\Delta T$ can be estimated as

$$\Delta T \equiv T_s - T(\theta) \approx \big(1 - \varepsilon(\theta)\big)(T_s - T_a) \, . \tag{4.13}$$

Therefore, given the directional emissivity $\varepsilon(\theta)$ that can be expressed analytically using the emissivity models [67] [106] presented in Section 4.4.4, without the loss of generality, we can continue the derivation by assuming the equivalence between the two

sides of Eq.(4.13). The actual temperature, $T_s(\theta)$, can be expressed in terms of $T(\theta), T_a$, and $\varepsilon(\theta)$ as

$$T_s(\theta) - T(\theta) = \big(1 - \varepsilon(\theta)\big)(T_s(\theta) - T_a)$$

$$T_s(\theta) = \frac{T(\theta) - \big(1 - \varepsilon(\theta)\big)T_a}{\varepsilon(\theta)} \quad . \tag{4.14}$$

Eq.(4.14) is the first step of the correction algorithm, which recovers the actual temperature $T_s(\theta)$ from the value $T(\theta)$ measured by IR imaging.

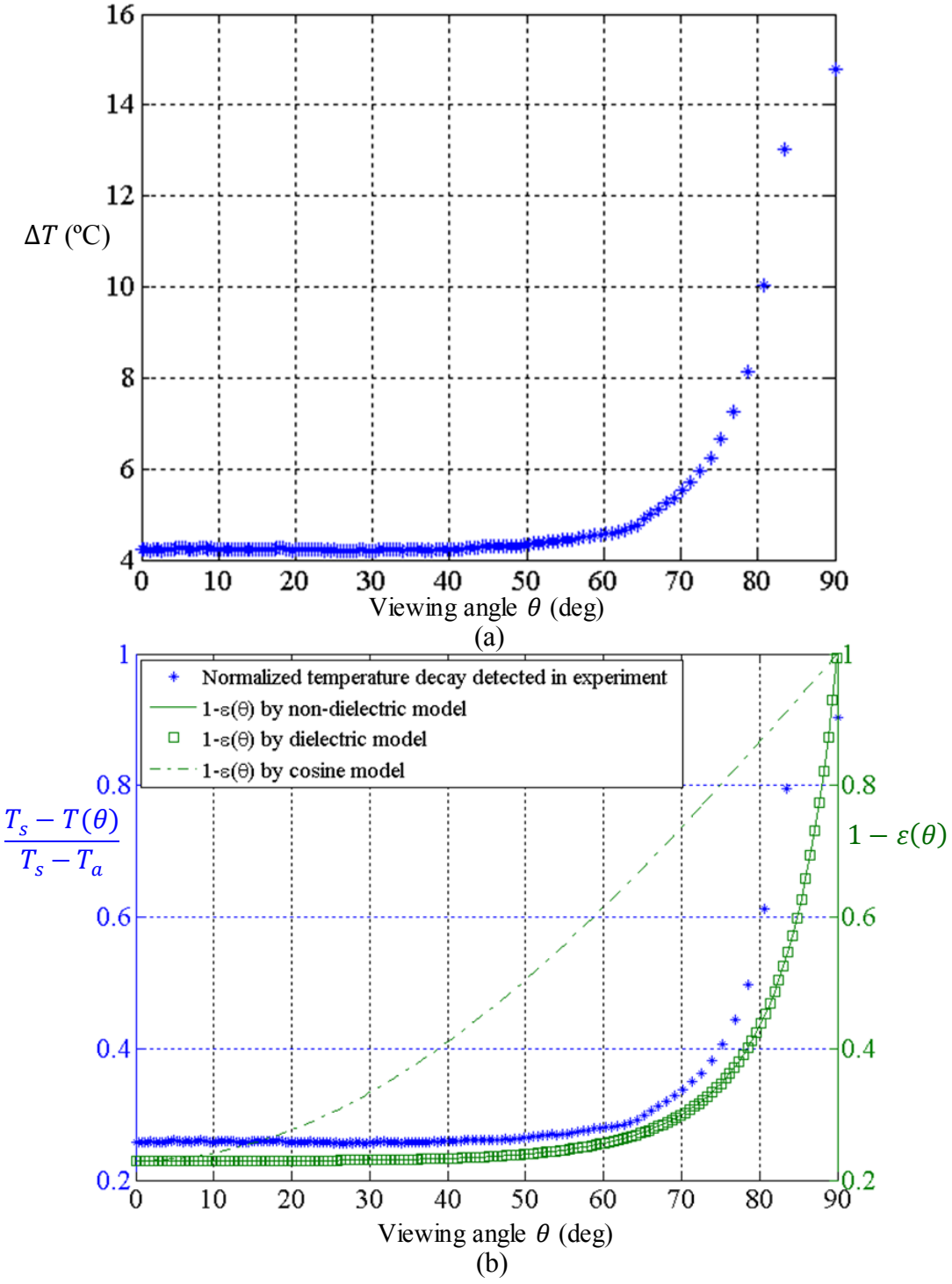


**Figure 4.13** (a) Average value of $\Delta T = T_s - T(\theta)$ for the six temperatures considered in the cylindrical phantom experiment. (b) Temperature measurement error (left axis) and computed value of 1- $\varepsilon(\theta)$ (right axis) as a function of the viewing angle $\theta$. $\varepsilon(\theta)$ is the directional emissivity computed using the dielectric, non-dielectric, and cosine models.

Due to the imperfect emissivity models for $T_s(\theta)$, Eq.(4.14) may still contain the unknown bias in which the variation of surface curvature is not taken into account. Therefore, in the second step of the correction algorithm, the quantity $T_s(\theta)$ is calibrated with respect to an unbiased temperature measurement sampled from the region of the IR image where the curvature-induced artifact is absent. The unbiased temperature is sampled at the location with zero viewing angle $T_0 = T(\theta = 0)$ in the IR image to minimize the artifact induced by the viewing angle. The biased temperature prediction obtained using Eq.(4.14), $T_s^0 = T_s(\theta = 0)$, is also computed at the same location. By taking the ratio of $T_s^0$ and $T_0$, we find the scaling factor

$$S = \frac{T_0}{T_s^0} = \frac{T(\theta=0)}{T_s(\theta=0)} \tag{4.15}$$

that can be used to calibrate $T_s^0$ to determine the unbiased temperature observation $T_0$. We can then utilize $S$ to calibrate the biased temperature value $T_s(\theta)$ (from Eq.(4.14)) at all locations (for a range of viewing angles $\theta$) in the same IR image. The accurate temperature $T_s^*(\theta)$ after calibration and accounting for the curvature induced artifacts can be found as

$$T_s^*(\theta) = S \cdot T_s(\theta) \quad . \tag{4.16}$$

For validation purposes, we applied the correction procedures described by Eqs.(4.14)-(4.16) to the IR image acquired in the cylindrical phantom experiment (Section 4.5.2). The image on the left hand side of Fig.4.14 (a) is the color-coded IR image of the cylindrical phantom before applying the described correction algorithm. The surface of phantom is isothermal in the experiment, and the viewing angle $\theta$ increases symmetrically toward the perimeter of phantom.

According to Eq.(4.14), we first applied the non-dielectric model [106] to compute the directional emissivity of the cylindrical phantom using the optical properties described in Section 4.4.5. In the second step, the average temperature along the central vertical line on the phantom surface (the vertical black line in Fig.4.14(a)), where the viewing angle $\theta = 0$, was taken as the unbiased observation $T_0$ in Eq.(4.15) to determine the scaling factor $S$. Finally, the scaling factor $S$ is used to multiply the predicted temperature $T_s(\theta)$ obtained using Eq.(4.14) at all other locations. The resulting phantom image after applying the three-step correction algorithm is shown on the right hand side of Fig.4.14(a). To quantify the temperature distribution before and after the correction, the 1D temperature profiles along the horizontal direction are plotted in Fig. 4.14(b) as a function of the viewing angle. As the viewing angle exceeds 40º we can clearly observe a temperature drop towards the sides of phantom surface prior to the correction. The temperature profile becomes more uniform after correction (right hand side plot of Fig.4.14(b)). We observe that in the range of 40 º to 60 º, the temperature decrease associated with the directional emissivity is uniformly rectified. Since the phantom surface is isothermal, the recovered uniformity of the temperature profile after correction validates the correction procedure described by Eqs.(4.14)-(4.16).

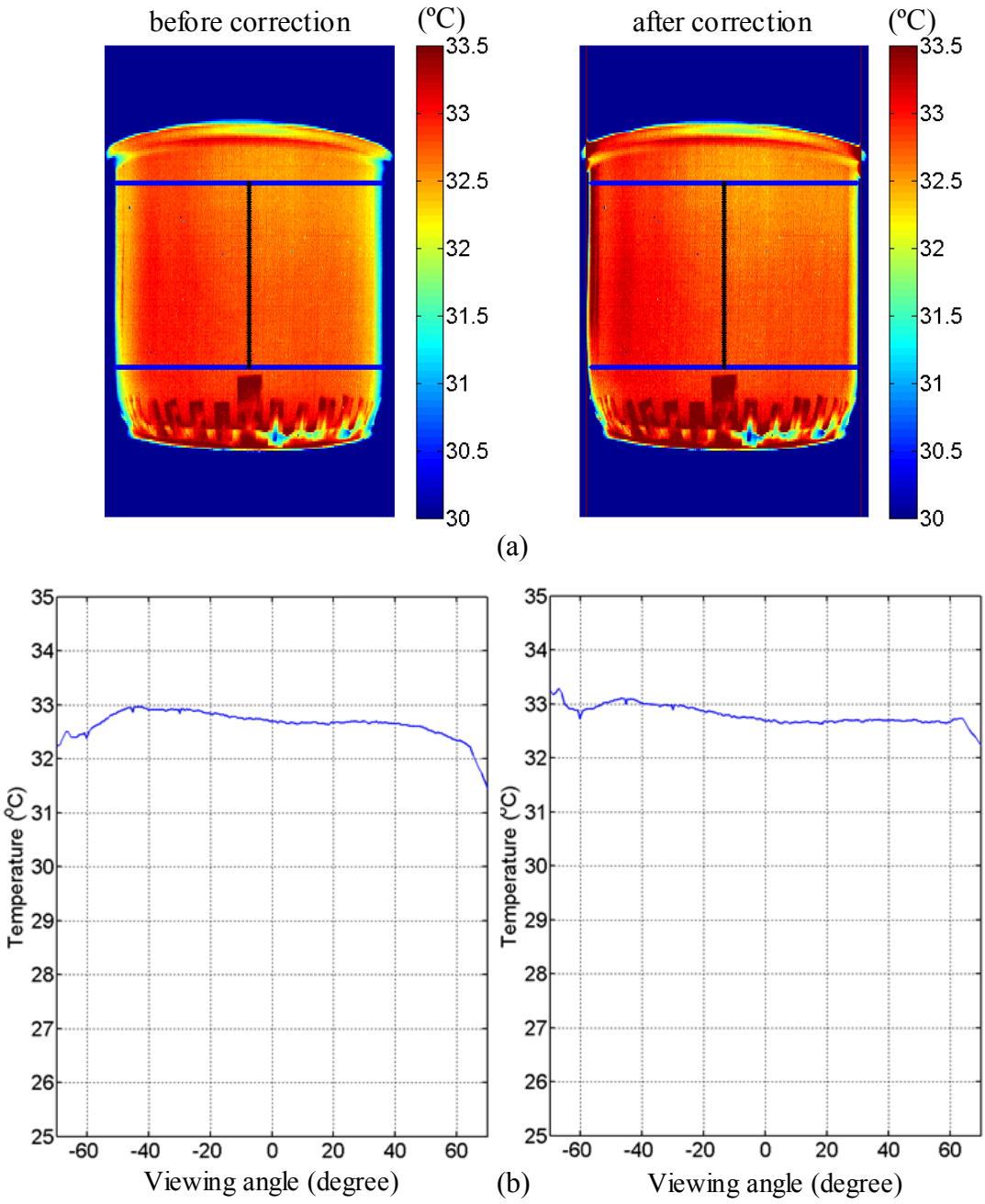


**Figure 4.14** Results of applying the three-step correction algorithm (ambient temperature $T_a = 23°C$) to the IR images of the cylindrical phantom: (a) Color-coded IR images before (left) and after (right) correction. The mean temperature along the central vertical line (black line) is taken as the unbiased observation for calibration (Eq.4.15). Mean value of the temperature as a function of the viewing angle before (left) and after (right) correction (temperature is averaged vertically within the rectangular region bordered by two horizontal blue lines in (a)).

## 4.6 Conclusions

Based on results shown in Fig.4.7, it can be inferred that the influences of viewing angle as well as travel distance (both associated with the curvature effect) are negligible when the viewing angle is less than 40º. As the viewing angle increases beyond 40º, we observe that both two factors cause a gradual apparent decrease of temperature detected in the IR image (Fig.4.9), resulting in a systematic measurement error. The effect associated with travel distance is of the order of 0.05ºC for path differences of the order of few centimeters. This effect is relatively minor compared to the effect of the viewing angle, which produces a temperature decrease of around 0.2ºC.

When the viewing angle exceeds 60º, as described in the cylindrical phantom experiment in Section 4.5.2, the temperature drops significantly with the increase of viewing angle. In the range of 70º - 80º (Fig.4.10), the resulting temperature decrease can be in excess of 2ºC compared to the central location with zero viewing angle.

By comparing measurement errors with the computed directional emissivity found using the three models (Fig. 4.11), we conclude that the linear relationship (Eq.4.10) proposed by Clark [101], along with the dielectric [67] or non-dielectric [106] models, is a valid approximation of the measurement errors associated with the directional emissivity. The analysis of normalized measurement error $\Delta T^*$ (Fig.4.12) indicates that the six curves obtained for various temperatures display consistent dependence on the viewing angle. The dependence of the measurement error on temperature is minor.

Using optical properties of pure water, in Section 4.4.7 we validated the theoretical predictions of the directional emissivity of skin using the dielectric and non-dielectric models. This allows us to correct for the systematic errors arising in temperature measurements of the skin when a significant surface curvature is present. However, the liquid contained in skin tissue is actually a saline solution rather than pure water, which may lead to differences in the optical and radiative properties. The optical and radiative properties of saline solutions in the infrared domain of the spectrum are not well known and would require further study. Furthermore, the models used in this study neglect the heterogeneous composition of material and scattering properties of surface, and a more accurate and complete model would have to account for these as well. To model the directional emissivity of skin with better fidelity, more fundamental studies are necessary to account for the identified in this section.

The validation conducted using the cylindrical phantom (Fig.4.13) demonstrates the feasibility of the three-step correction algorithm proposed in this thesis. Therefore, given the viewing angle distribution as well as the 2D IR temperature map of the human body, the correction can be applied to estimate the measurement errors caused by the directional emissivity. More importantly, the systematic errors owing to the surface curvature can be corrected for, leading to an accurate temperature measurement. The association between the viewing angle distribution and the temperature map relies on an accurate 3D imaging mapping of the skin surface geometry, which is the topic to be presented in Chapter 5.

# Chapter 5

# Three-dimensional quantitative thermal mapping of the human body

## 5.1 Overview

The aim of this chapter is to develop methodologies to accurately map 2D temperature distributions measured by an infrared camera onto 3D surfaces to enable quantitative medical diagnostic applications. For this purpose we devised an imaging system that combines the Microsoft Kinect imager with a high-accuracy IR camera to generate 3D IR thermal maps. Using appropriate software tools, an algorithm was developed to map the 2D IR radiation information captured by a sensitive, high-resolution 2D infrared imager onto the 3D shape data captured by Kinect. The viewing angle distribution over the 3D surface was incorporated using the models and empirical formulas introduced in Chapter 4, to compensate for the artifact of directional emissivity. We evaluated the feasibility of

the 3D thermal mapping system and the measurement accuracy improvement achieved by the correction formula by analyzing several test cases.

## 5.2 Introduction and literature review

3D imaging solutions are becoming increasingly popular in science, engineering and in everyday life; some of the progress being driven by the growing market for interactive gaming applications. During the past decade low cost 3D imaging solutions have reached the market. 3D imaging sensors can be classified into active and passive sensors. An active sensor first projects electromagnetic radiation onto the object, and the transmitted or reflected signal from the object is recorded. Laser triangulation, structured light, time of flight, holographic interferometry and holographic techniques fall into this class of methods [114]. A passive sensor records the electromagnetic energy naturally emanating from the object, such as in stereo vision and photogrammetry [114]. In indoor 3D mapping applications, such as robotics and surveillance, low-cost sensors are more popular than expensive laser scanners [115]. One of the most popular, consumer-grade sensors developed in recent years is the Microsoft Kinect imager. It was originally designed for gaming applications, however, in recent years this sensor has revolutionized and driven research in 3D mapping in the indoor environment. Related applications are reviewed in the study of Henry et al. [116] .

Incorporating temperature data captured by a 2D IR camera into the 3D depth map generated by a 3D imager, adds a new layer of complexity to the original 3D imaging problem. There are three major classes of systems used to generate 3D IR

images. The first class comprises two IR cameras, which acquire two thermographic images of the same object [117, 118]. Based on point-pairs registration between the images acquired by the two IR cameras, the 3D surface of object can be inferred using the stereo vision method. The second class of systems consists of two digital cameras and one IR camera [12]. The 3D surface of the object is measured by the binocular subsystem of the digital camera pair, and the IR camera acquires 2D thermographic images of the object. 3D thermal map is then achieved by mapping the 2D temperature texture onto the 3D surface. The 3D surface maps computed by these two methods are based on stereo vision algorithms, which rely on the clear detection of feature points in color or IR images. Therefore, the accuracy of the 3D data depends on the texture of surface: for an object with well-defined feature points it performs with better accuracy. Often the natural feature points on the human body are not sufficient for an accurate 3D reconstruction, and artificial feature points have to be applied to improve measurement accuracy of the 3D structure.

The third class of systems that uses the structured light scanning technique to obtain accurate 3D surface data [119-121] is not dependent on the surface texture. Such a system usually includes a source that projects structured light (a grid pattern) onto the surface and one or more cameras that record the pattern formed on the surface. The 3D shape of the surface is computed from the deformation of the regular grid pattern. When compared with stereo vision systems, the system based on structured light has higher data acquisition rates and it is less computationally expensive [114].

The Microsoft Kinect is a low-cost and convenient option to implement structured light 3D imaging. It projects structured IR light onto the surface, and neither this light nor

the projected pattern are detectable by the human eye. Therefore this form of imaging is comfortable to the patient in medical applications [122]. Another advantage is that Microsoft Kinect can generate depth maps at a relatively high frame rate of 30 fps with a resolution of 640×480 [115]. These features enable the device to capture the patient's motion in real-time [123]. Therefore the Kinect-based system developed for the present study holds the potential to enable dynamic 3D IR thermal map (measure 3D temperature evolution as a function of time) [124] with real-time motion tracking.

Over the past few years the Kinect imager has also become popular in a variety of scientific and technical imaging applications. Volumetric measurements achieved by the Microsoft Kinect are gaining attention in the medical community for breast cancer treatment evaluation [125] and lymphedema detection [126]. Thus, in addition to correcting for the viewing angle artifacts in 3D IR thermal map, implementations by Kinect can provide volumetric information to supplement the thermal signal, which can lead to more comprehensive data collection for medical diagnostic purposes.

To solve the measurement challenge caused by directional emissivity artifacts, researchers integrated 3D spatial information with IR thermal map to improve measurement accuracy. This combination of imaging techniques was used in engineering applications, such as in a wind tunnel experiment [127], for reconstruction of water waves [117], and for tracking and recognition of moving objects [128]. However, only a few researchers have tackled this issue in medical applications. Aksenov et al. [11] used thermal stereoscopy to characterize inflammation. Ju et al. [12] developed 3D thermographic imaging techniques to rectify the viewing angle artifact based on a heat flux model for the diagnosis of inflammation. They standardized face thermal mapping

by a 3D facial shape template. The shortfall of this approach is that the heat flux model is not based on the fundamental behavior of the directional emissivity, and the angular variation was simplified by using the cosine function, which can lead to significant error. Very few studies have been reported that used the directional emissivity of skin to correct for the viewing angle artifact in in-vivo IR thermography using the 3D imaging technique [12] [11]. The objective of this chapter is to introduce a versatile 3D IR imaging system relying on the inexpensive and popular Microsoft Kinect sensor that allows transient 3D temperature measurements of the human body suitable for quantitative medical diagnostic applications.

# 5.3 Materials and methods

## 5.3.1 Imaging system and data acquisition

In this study, we introduce the 3D infrared imaging system shown in Figure 5.1. It consists of the Kinect for Windows® (Microsoft Corporation) 3D imager (top), and the infrared camera- Med Cam® (Hurley IR, Mt Airy, MD) (bottom), which contains the IR detector- THERMAL-EYE SERIES 17-640® (L-3 Communications Corporation, Dallas, TX).

The Kinect device has a field of view (FOV) of $57^{o}\times43^{o}$ (Horizontal ×Vertical), and acquires a RGB and depth image streams with a frame rate of 30 fps. The resolution of the RGB image is 1280×960, and the resolution of the depth image is 640×480. To reconstruct the 3D surface data for the human body, we used the Kinect device along with open-source software – ReconstructMe[129]. ReconstructMe can achieve real-time

3D reconstruction by scanning the human body from multiple directions, and the reconstructed 3D surface grid is stored in the format of polygon (.ply).


**Figure 5.1** The 3D infrared imaging system developed at the Heat Transfer Lab of JHU combining the Kinect imager (top) and the infrared camera (bottom).

The infrared camera detects electromagnetic radiation in infrared spectrum of 7.5-13.5 μm with FOV of $57^{o}\times43^{o}$ (Horizontal ×Vertical). The camera is equipped with an uncooled amorphous silicon microbolometer focal plane array (FPA) having dimensions of 640×480. It acquires 16-bit raw data with resolution of 632×476 at a frame rate of 30 fps, and the IR camera has temperature sensitivity of 0.0315 $^{o}$ K. It is controlled by a PC using PCI Express Card - PIXCI® EB1, and IR images are acquired using a LabVIEW®-based software (version: 11.0.1, National Instruments Corporation, Austin, TX).

The 2D thermal image of the human body is acquired by the IR camera. Prior to image acquisition, we conducted black-body calibration to obtain the conversion between radiance detected by IR camera and the corresponding temperature. The radiance-

temperature relationship is modeled by a fourth order polynomial as shown in Eq.5.1, similar to the IR camera used in Chapter 2 and Chapter 3 [93]. Within the range of temperatures used in the calibration, the infrared camera can generate the 2D thermal maps presented as temperature data, $T(℃)$, based on the polynomial of pixel intensity $g$:

$$T(℃) = -3.459387 \times 10^5 + 56.540702g - 0.003469g^2 + 9.470542 \times 10^{-8}g^3 - 9.699380 \times 10^{-13}g^4 \ . \quad (5.1)$$

In the wavelength range of 2 - 14 μm, the emissivity of human skin is in the range of 0.98±0.01[65-67]. Therefore, the relative temperature measurements obtained using the parameters from the black-body calibration can easily be corrected for absolute values, as needed. On the other hand, the temperature difference between two measurement samples (two locations from the same image or data from different images recorded by the same camera) will be accurate without the need for correction. In quantitative diagnostic applications, temperature differences (local temperature increase for cancer [1-8, 100] or inflammation [41], and temperature decrease for ischemia [41], for example) between healthy and diseased regions of the body are of particular interest. To validate the thermal mapping measured by IR camera, we also measured the temperature at selected locations on the skin with thermocouples. The thermocouple measurement was conducted using a USB-based data acquisition card (NI USB-9211®, National Instruments Corporation, Austin, TX).

### 5.3.2 The workflow of 3D IR imaging

Using the imaging system described in section 5.3.1, the work flow leading to 3D thermal mapping with temperature correction can be summarized in four major steps: (1) system calibration, (2) 3D to 2D information mapping, (3) 2D to 3D information mapping and (4) curvature-induced artifact correction. The flowchart showing these three steps, along with their detailed algorithms is illustrated in Figure 5.2.

The objective of Step (1) - system calibration - is to determine the imaging system parameters to achieve the 3D-2D coordinate transformation between Kinect and the IR camera. This step is necessary, since the 2D (IR image) to 3D (Kinect coordinates) transformation is not unique. Therefore the 3D Kinect data are mapped into the 2D IR image first, in an intermediate step, followed by the stretching or the 2D thermal map into the 3D Kinect surface to generate the 3D raw thermal map. The camera parameters from Step (1) enable the 3D-2D information mapping in Step (2), in which the 3D spatial data acquired by Kinect are related to temperature in the 2D IR image. In Step (3) the combined Kinect-IR 2D data are stretched backed onto the 3D Kinect surface, by mapping pixel-by-pixel the IR temperature data onto the corresponding Kinect pixel data to generate the raw 3D thermal map. The empirical formula developed in Chapter 4 is applied to the raw 3D thermal map in Step (4), the curvature-induced artifacts correction, to compensate for the temperature errors (apparent temperature decrease) due to the directional emissivity of skin. The details of each step are explained in the following sections.

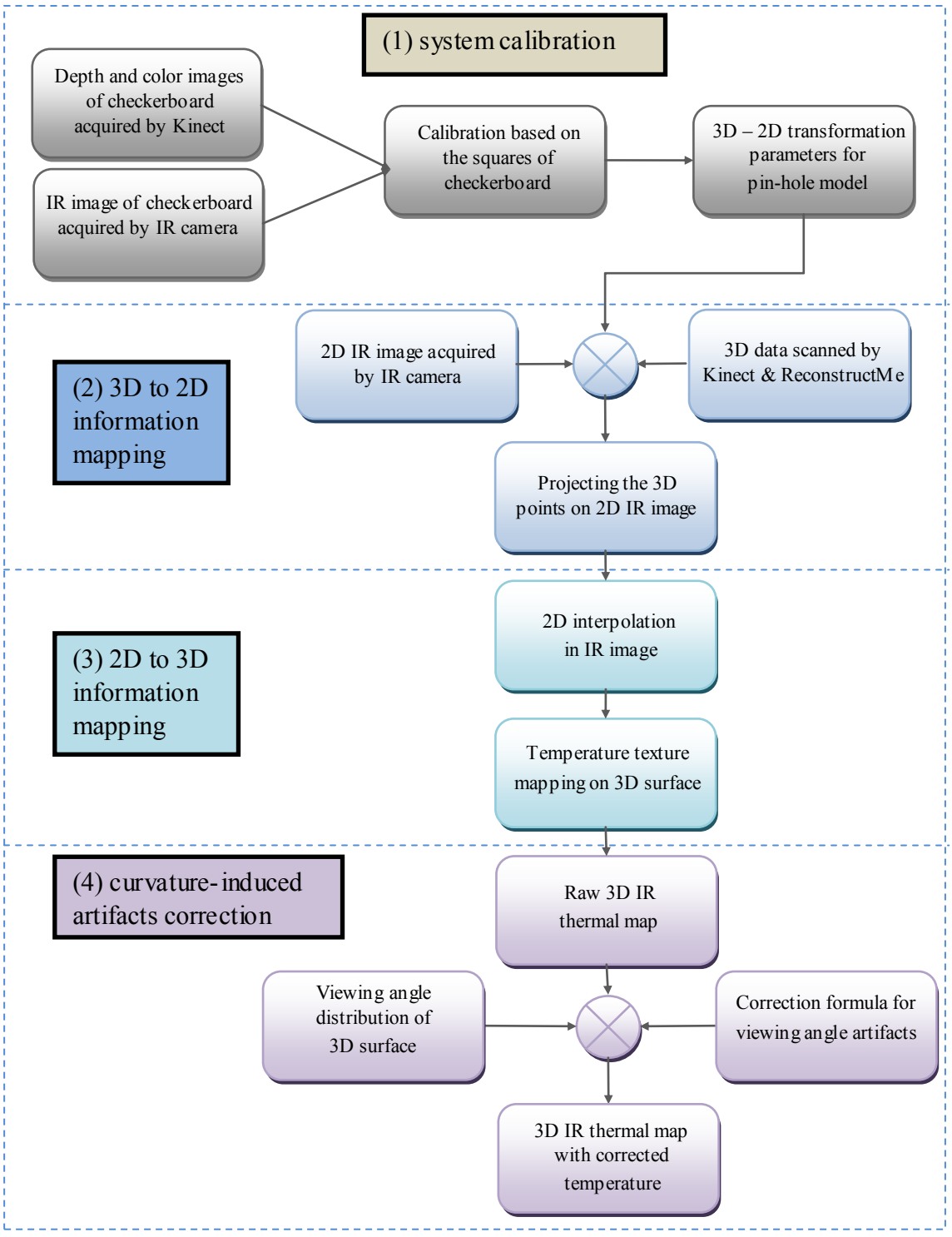


**Figure 5.2** Flowchart of 3D thermal mapping with curvature correction, which includes four major steps: (1) system calibration, (2) 3D to 2D information mapping, (3) 2D to 3D information mapping, (4) curvature-induced artifacts correction.

### 5.3.3 System calibration

Mapping the thermal texture to 3D surface data relies on an accurate coordinate transformation between Kinect and IR cameras. The necessary transformation parameters are obtained via system calibration. In this study, we adopted the method and the MATLAB toolbox developed by Herrera et al. [130, 131] to determine the system parameters.

The calibration toolbox is based on the pinhole camera model developed by Heikkila[132], which consists of a perspective projection model and a correction model for lens distortion. We also utilized the MATLAB toolbox developed by Herrera et al. [130, 131]. The toolbox provides an established platform capable of simultaneously calibrating the external and internal parameters of the three cameras: the color camera and depth cameras of Kinect (the two Kinect cameras are mounted into the same housing, Fig. 5.1, top), and the IR camera (Fig. 5.1, bottom). The instrumentation steps, including image acquisition, calibration computation, and image processing, are all implemented using MATLAB 2013 (MathWorks Inc., Natick, MA).

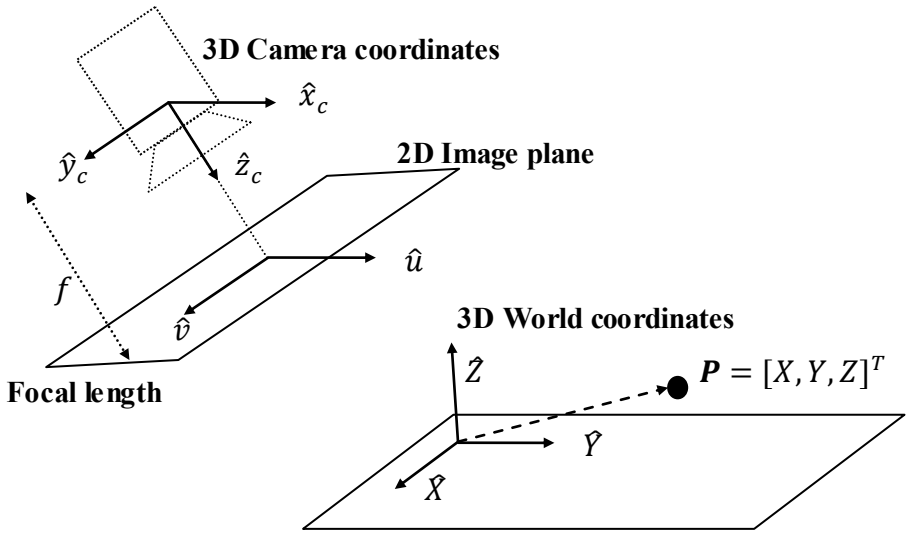


**Figure 5.3** Schematic of the pinhole camera model used in imaging system calibration

### 5.3.3.1 Camera model for system calibration

By adopting a notation similar to that used in the literature [121, 127, 130], the schematic of the pinhole camera model [132] is illustrated in Figure 5.3. This schematic illustrates the linear transformation between the 3D world coordinates and the 2D image plane.

Given a point $\boldsymbol{P} = [X, Y, Z]^T$ in 3D world coordinates, and letting $\boldsymbol{p} = [u, v]^T$ be the corresponding coordinates in the 2D image plane, the linear transformation between these two points can be formulated as

$$\begin{bmatrix} u \\ v \\ 1 \end{bmatrix} \propto \boldsymbol{KT} \begin{bmatrix} X \\ Y \\ Z \\ 1 \end{bmatrix} \quad . \tag{5.2}$$

In Eq. 5.2 $\boldsymbol{T}$ denotes the transformation between the 3D world coordinates and the 3D camera coordinates. $\boldsymbol{T}$ contains the external parameters, the rotation matrix $\boldsymbol{R}$ and the translation vector $\boldsymbol{t}$, described as

$$\boldsymbol{T} = \begin{bmatrix} \boldsymbol{R} & \boldsymbol{t} \\ 0 & 1 \end{bmatrix} \quad . \tag{5.3}$$

The term $\boldsymbol{K}$ in Eq. 5.2 is the matrix containing the internal parameters of camera, and it describes the projection from 3D camera coordinates to the 2D image plane as

$$\boldsymbol{K} = \begin{bmatrix} \alpha f & 0 & u_{0c} & 0 \\ 0 & f & v_{0c} & 0 \\ 0 & 0 & 1 & 0 \end{bmatrix} \quad . \tag{5.4}$$

In Eq. 5.4 $\alpha$ is the pixel aspect ratio of the image plane, $f$ is the focal length of the camera, i.e. the distance between the projection center and the image plane. $[u_{0c}, v_{0c}]^T$ is the principal point, which is defined as the pixel coordinate for the center of image plane.

Using the linear projection described by Eqs. 5.2-5.4, given a point $\boldsymbol{P} = [X, Y, Z]^T$ in 3D world coordinates, we can first compute the corresponding coordinate $\boldsymbol{p_c} = [x_c, y_c, z_c]^T$ in 3D camera coordinates. According to the model of perspective projection in homogenous coordinates [96], by dividing the first two components of $\boldsymbol{p_c}$, $[x_c, y_c]^T$, with its third component $z_c$, we obtain the linear projection $[x_u, y_u]^T$ on the 2D image plane of the camera as

$$\begin{bmatrix} x_u \\ y_u \end{bmatrix} = \frac{1}{z_c} \begin{bmatrix} x_c \\ y_c \end{bmatrix} \quad . \tag{5.5}$$

In Eq. 5.5 $[x_u, y_u]^T$ is the ideal projection of $\boldsymbol{p_c}$ without considering the non-linear effects arising in practice. The pinhole model developed by Heikkila [132] also accounts for the

radial and tangential distortion introduced by the lens. Using the undistorted projection $[x_u, y_u]^T$, the distorted projection $[x_d, y_d]^T$ on the image plane is modeled as

$$\begin{bmatrix} x_d \\ y_d \end{bmatrix} = (1 + k_1 r^2 + k_2 r^4 + + k_5 r^6) \begin{bmatrix} x_u \\ y_u \end{bmatrix} + d_x \tag{5.6}$$

$$d_x = \begin{bmatrix} 2k_3 x_u y_u + k_4 (r^2 + 2x_u^2) \\ k_3 (r^2 + 2y_u^2) + 2k_4 x_u y_u \end{bmatrix} . \tag{5.7}$$

In Eqs. 5.6 and 5.7 the terms $r^2 = x_u^2 + y_u^2$ and $[k_1, k_2, k_3, k_4, k_5]$ represent the distortion coefficients of the camera. Consequently, the distorted pixel location $[u_d, v_d]^T$ in the acquired 2D image is computed based on $[x_d, y_d]^T$ as

$$\begin{bmatrix} u_d \\ v_d \end{bmatrix} = \begin{bmatrix} \alpha f & 0 \\ 0 & f \end{bmatrix} \begin{bmatrix} x_d \\ y_d \end{bmatrix} + \begin{bmatrix} u_{0c} \\ v_{0c} \end{bmatrix} . \tag{5.8}$$

In Eq. 5.8 $\alpha$ is the pixel aspect ratio in the 2D image, $f$ is the focal length of the camera, and $[u_{0c}, v_{0c}]^T$ is the principal point of 2D image plane, as described in Eq. 5.4.

### 5.3.3.2 Imaging setup for system calibration

To determine the external and internal parameters of the system, the imaging setup for system calibration is illustrated in Figure 5.4. The coordinate systems of the three cameras, the color and depth cameras of Kinect, and of the IR camera are denoted by {C}, {D}, and {I}, respectively. A planar checkerboard with $8 \times 8$ squares, shown in Fig. 5.5(a), is used to generate the 3D world coordinates for the pinhole model. For calibration purposes, the images of the planar checkerboard are simultaneously acquired by the three cameras. In order to mark the locations of the square corners detectable in the IR image,

we inserted metal drawing pins at each corner of checkerboard squares, as shown in Fig. 5.5(b). The emissivity difference between the metal pins and the surface of the checkerboard creates a contrast in the IR image. The contrast enables us to identify the location of these corners in the IR image. During the image acquisition, we also tried to enhance the contrast of the metal pins and background by reflecting the thermal radiation from surrounding heat sources (such as human body and lighting) on an ad hoc basis.

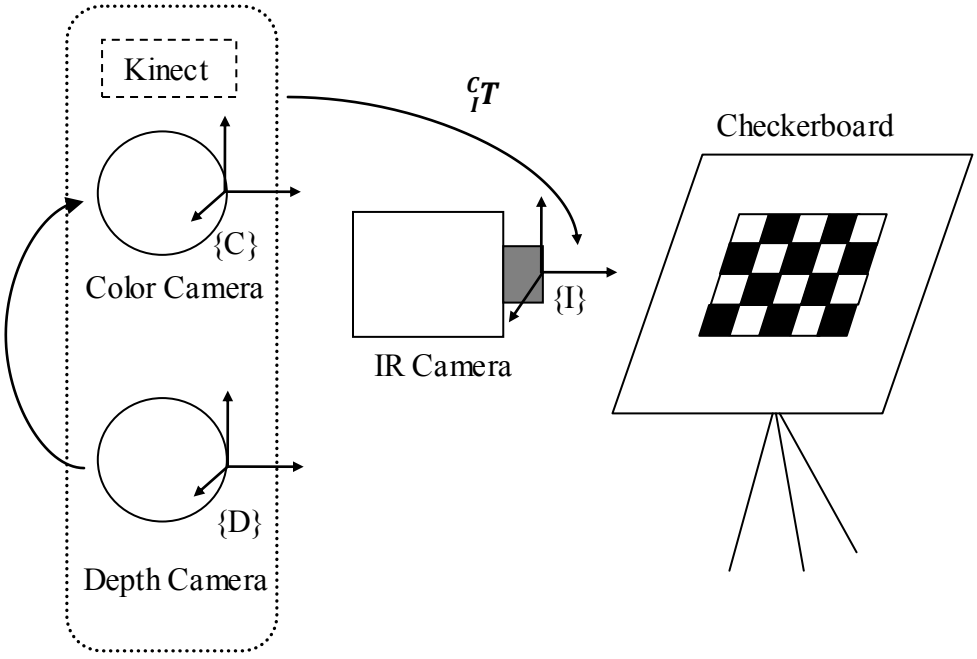


**Figure 5.4** Schematic of the imaging setup for system calibration with 3D camera coordinates used in calibration: color camera {C} and depth camera {D} of Kinect, and the IR camera {I}.

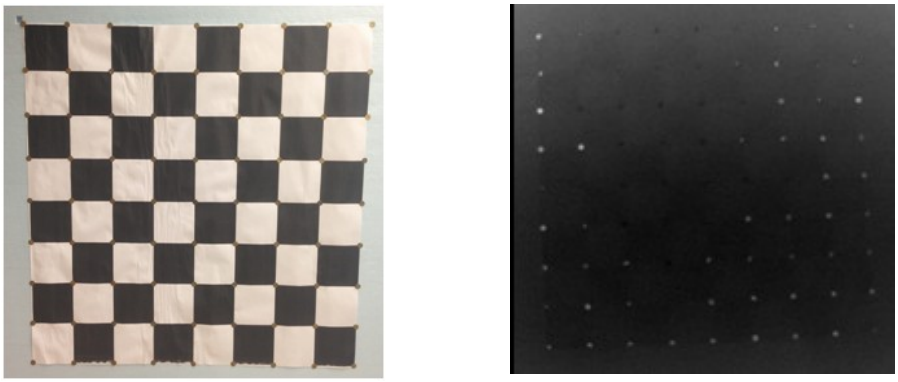

(a) (b)

**Figure 5.5** (a) Checkerboard for camera calibration and (b) the IR image of the checkerboard with metal pins located at the corners of each square.

According to the calibration methodology developed by Herrera et al. [130, 131], we acquired three sets of checkerboard images with the three cameras: a color image, a depth image, and an IR image. In addition, the checkerboard was positioned with three orientations for each camera, as illustrated in Fig. 5.6. At each orientation, the distance between the checkerboard and the cameras was also varied, and images with the three cameras were acquired simultaneously at each combination of orientation/distance. Images were acquired at 8 distances with three orientations, thereby leading to 24 images per camera. In the acquired image datasets, we manually selected the locations of the checkerboard corners in both color and IR image datasets (the corner locations in the IR image are pinpointed by the metal pins), and the locations of checkerboard edges were selected in the depth image datasets. Via the relation of location correspondence provided by these control points, the camera parameters were iteratively optimized using the Levenberg-Marquardt algorithm, as described in [130].

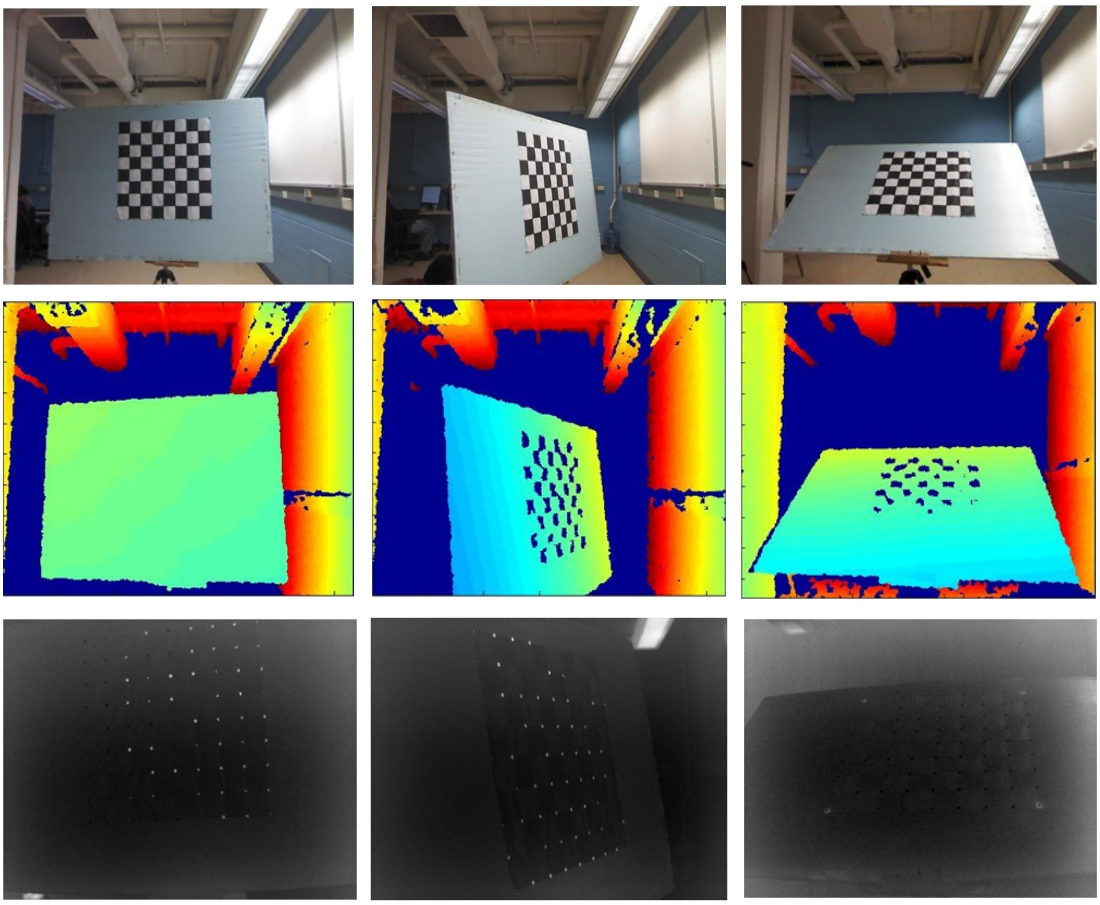

**Figure 5.6** In system calibration, three image sets of the checkerboard with three orientations were acquired: color images acquired by Kinect (top row), depth images acquired by Kinect (middle row), and IR images acquired by the infrared camera (bottom row).

### 5.3.4 3D - 2D information mapping

The next step in obtaining the 3D thermal map is the mapping of the depth information into 2D, to associate depth data to the corresponding temperature in the IR image. The camera parameters obtained from system calibration enable an accurate coordinate transformation from the Kinect device to the IR camera. In our application, the transformation from the depth camera to the IR camera is of particular interest, so that the 3D spatial information can be associated with the 2D thermal mapping in the IR image.

We can achieve the transformation using the matrices: ${}^{D}_{C}\boldsymbol{T}$ and ${}^{C}_{I}\boldsymbol{T}$ as indicated in Fig. 5.4, in which ${}^{D}_{C}\boldsymbol{T}$ represents the transformation between the depth camera and the color camera, and ${}^{C}_{I}\boldsymbol{T}$ represents the transformation between the color camera and the IR camera. These two matrices are obtained in the procedure of system calibration. According to Eq.5.3, the 3D coordinate $\boldsymbol{x_d}$ in the depth camera frame {D} can be transformed to the coordinate $\boldsymbol{x_c}$ in the color camera frame {C} using the matrix

$$ {}^{D}_{C}\boldsymbol{T} = \left\{ {}^{D}_{C}\boldsymbol{R}, {}^{D}_{C}\boldsymbol{t} \right\} , \tag{5.9} $$

where ${}^{D}_{C}\boldsymbol{R}$ and ${}^{D}_{C}\boldsymbol{t}$ represent the rotation matrix and the translation vector in ${}^{D}_{C}\boldsymbol{T}$. The color camera coordinate $\boldsymbol{x_c}$ is determined as

$$ \boldsymbol{x_c} = {}^{D}_{C}\boldsymbol{R}\boldsymbol{x_d} + {}^{D}_{C}\boldsymbol{t} \ . \tag{5.10} $$

Next, via $\boldsymbol{x_d}$ and the transformation between the IR camera and color camera

$$ {}^{C}_{I}\boldsymbol{T} = \left\{ {}^{C}_{I}\boldsymbol{R}, {}^{C}_{I}\boldsymbol{t} \right\} , \tag{5.11} $$

the corresponding point $\boldsymbol{x_i}$ in the IR camera frame {I} can be computed as

$$ \boldsymbol{x_i} = {}^{C}_{I}\boldsymbol{R}\boldsymbol{x_c} + {}^{C}_{I}\boldsymbol{t} \ . \tag{5.12} $$

In this way, any 3D point located in the Kinect depth camera frame can be projected to the corresponding 2D coordinates in the IR image to allow the association of depth and temperature information. Since the reference coordinates of ReconstructMe correspond to those of the depth camera of Kinect, any 3D point $\boldsymbol{x_d}$ scanned by ReconstructMe can be transformed from the depth camera to the corresponding point $\boldsymbol{x_i}$ in the IR camera by consecutively applying Eqs. 5.9-5.12.

After the 3D data are transformed from the depth camera to the IR camera, the corresponding 2D pixel coordinate in the IR image can be computed based on the internal parameters of the IR camera and Eqs. 5.5-5.8. This step completes the 3D-2D mapping using the parameters obtained from the system calibration.

### 5.3.5 2D - 3D information mapping

The next step in the generation of the 3D thermal map is the stretching of the 2D information onto the 3D depth map to generate the raw 3D thermal map. In this step the 2D IR image is overlaid with the point projected from the 3D data. Since there are more data points on the 3D surface than in the 2D infrared image, linear 2D interpolation is used to generate the missing temperature data. The raw thermal map on the 3D surface was generated based on the 2D temperature texture acquired in the IR image.

### 5.3.6 Curvature-induced artifact correction

As addressed in Chapter 4, the temperature measured by the IR detector in regions of large viewing angles appears lower than the actual surface temperature because of the artifact associated with directional emissivity. According to the theory introduced in Chapter 4 (Section 4.5.3), the raw 3D thermal map generated by the IR camera can be corrected using the three-step approach described by Eqs. 4.14–4.16. This is accomplished using the analytical expression for the directional emissivity $\varepsilon(\theta)$ of the object and the viewing angle distribution $\theta$ *(x,y,z)* on the surface.

After mapping the temperature texture from IR image to the 3D surface as described in Section 5.3.5, we apply the three expressions for the directional emissivity

$\varepsilon(\theta)$to the resulting 3D raw thermal map based on the three emissivity models introduced in Chapter 4, the dielectric [67], non-dielectric [106], and cosine models. To correct for the directional emissivity of the skin $\varepsilon(\theta)$, the viewing angle $\theta$ distribution on the 3D surface is first computed using the normal vector for each unit area as

$$\theta = cos^{-1}\left|\frac{\vec{Z}\cdot\vec{n}}{|\vec{Z}|}\right| \quad . \tag{5.13}$$

In Eq.5.13 $\vec{Z}$ is the 3D vector of the axis of the IR camera, $[0,0,1]^T$ in our coordinate system, and $\vec{n}$ is the normal vector of a unit area of the surface being imaged.

# 5.4 Results

## 5.4.1 The workflow of image processing

Based on the procedures described in previous sections, Fig. 5.7 illustrates the flowchart of the image processing steps along with the corresponding image data generated in each step. In this section, the content of the image data processed at each step will be described in detail, and the correction results discussed. According to the flowchart in Fig.5.7, we first acquired the images of the human body using Kinect and the IR camera, as illustrated by the procedure following Step (1). The 3D-2D transformation parameters from Step (1) were applied to Step (2) to achieve the 3D to 2D mapping. By applying the 2D interpolation and 2D-3D mapping, the raw 3D IR thermal map was generated in Step (3). Finally, the curvature-induced artifacts were corrected for to generate the final accurate 3D thermal map in Step (4).

### 5.4.2 Three dimensional surface reconstruction and the validation of camera parameters

To illustrate Steps.(1)-(4) in Figure 5.7, the images acquired by the depth camera and IR camera are shown in Figure 5.8. The 3D surface was reconstructed using ReconstructMe (v1.1.74) [129] as shown in Fig. 5.8(a), and Fig. 5.8(b) shows the color coded 2D temperature distribution of the body surface acquired by the IR camera. Using the transformation parameters obtained from the system calibration, the coordinates of the 3D grid of surface (Fig. 5.8(a)) were transformed to the 2D image coordinates as shown in Fig. 5.8(c). Next, the 2D IR image is overlaid with the points projected from the 3D data, as shown in Fig.5.8(d). The alignment between the 2D projection and the underlying IR image is used to validate the parameters from system calibration.

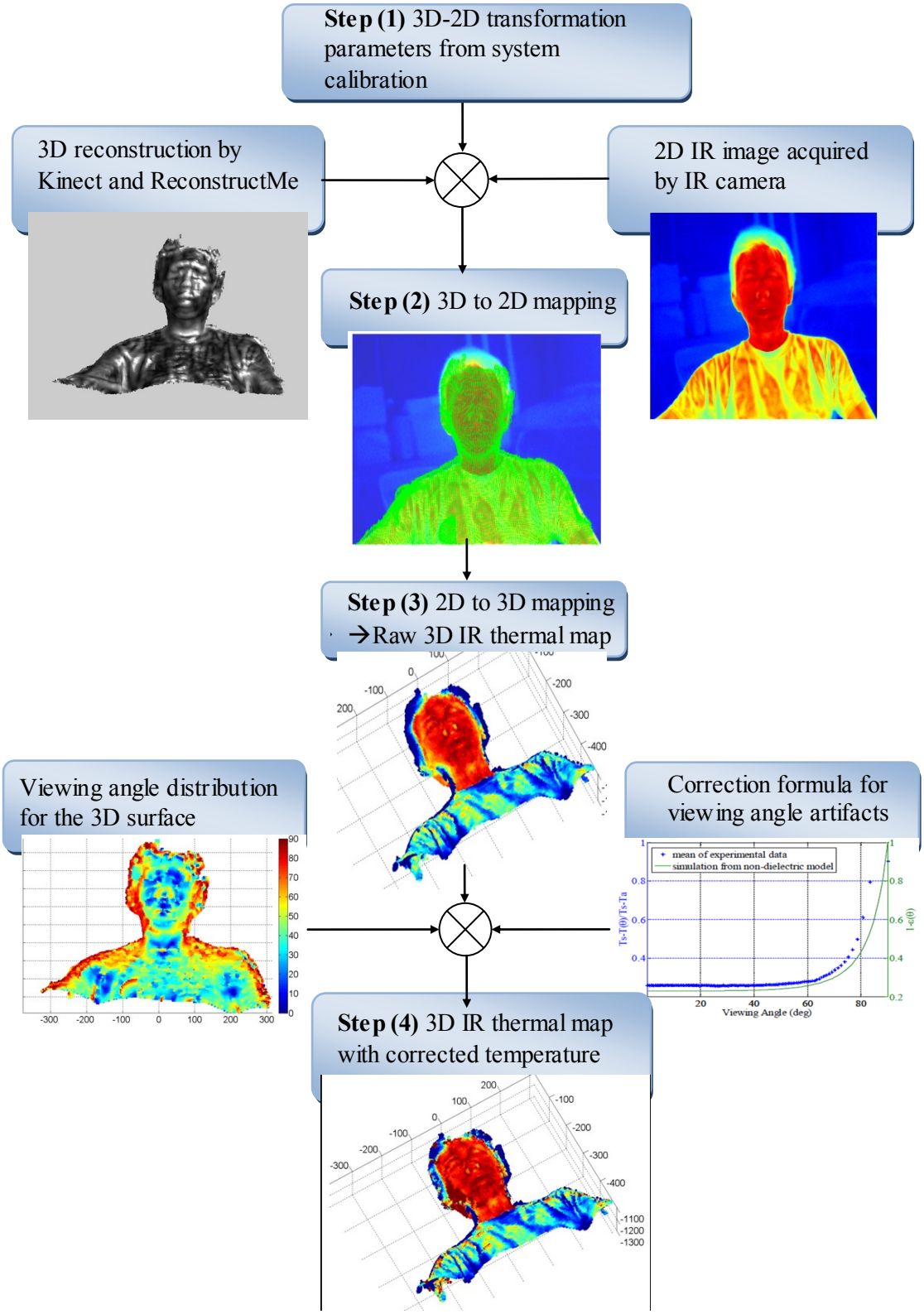


**Figure 5.7** Flowchart with image data generated at each step leading to the accurate 3D IR thermal map with viewing angle artifact correction.

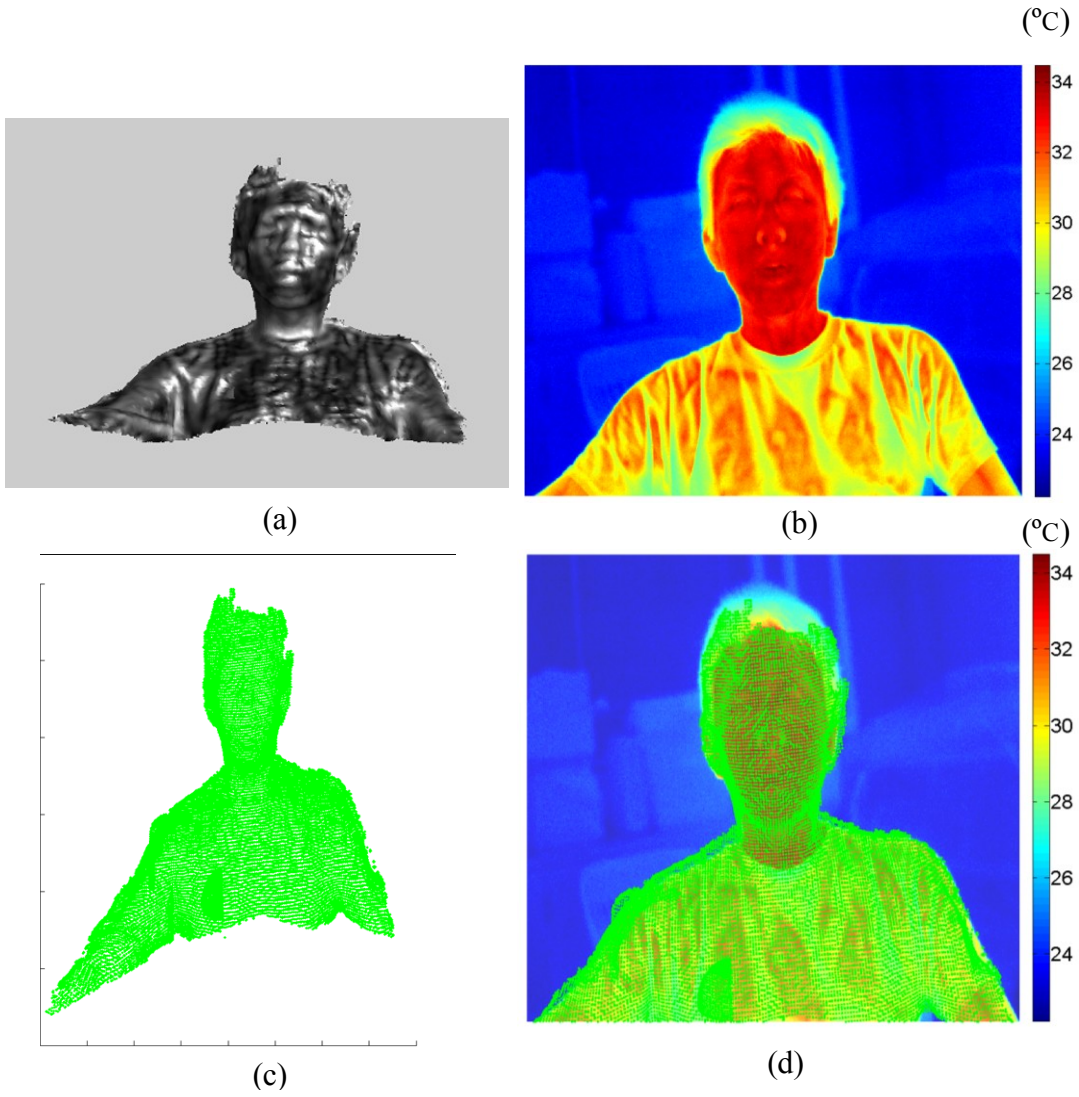


**Figure 5.8** (a) 3D surface of human body captured by Kinect and reconstructed using ReconstructMe. (b) Color coded 2D thermal map acquired by the IR camera. (c) 2D projection of the reconstructed 3D surface grid in IR image coordinates. (d) Overlay of the 2D IR thermal map from (a) and the 2D projection of surface grid (green dots) from (c).

## 5.4.3 Reconstruction of the 3D IR image

To achieve the 2D-3D transformation demonstrated in the flowchart shown in Fig. 5.7, for each point on the reconstructed 3D surface grid, we determine the corresponding temperature by interpolation using the neighboring pixels in the IR image (Fig. 5.8(d)).

The interpolated temperature value is then back-mapped to the point on the 3D grid, leading to the raw 3D IR thermal map displayed in Fig. 5.9.

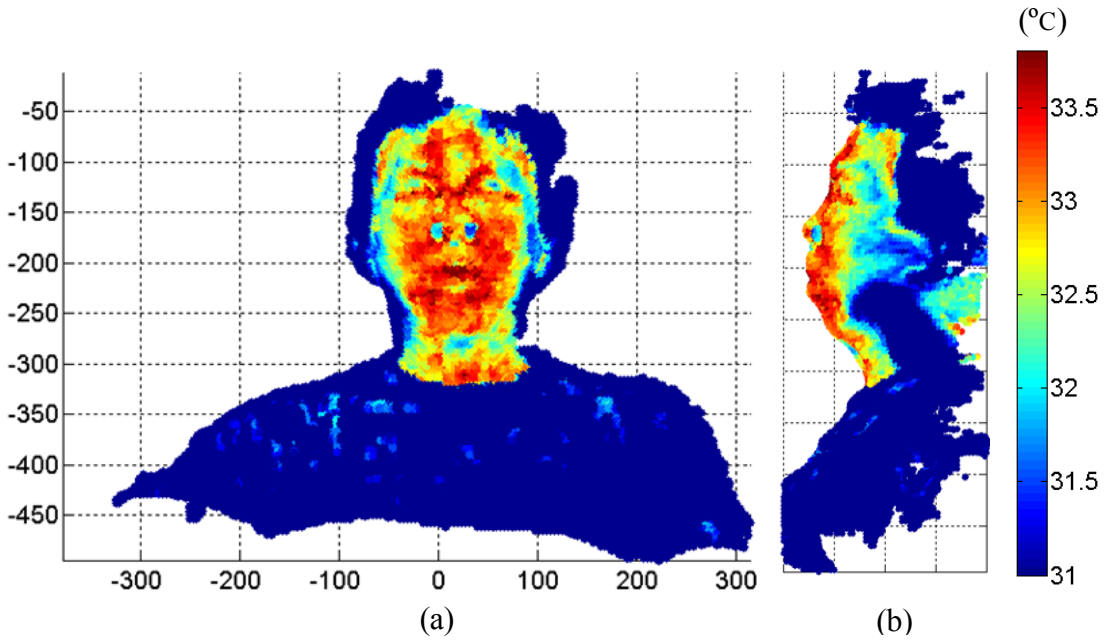


**Figure 5.9** Raw 3D IR thermal map achieved by back-mapping the interpolated temperature from the 2D IR image to the 3D reconstructed surface: (a) front view and (b) side view.

In the side view of the raw 3D IR thermal map in Fig. 5.9(b), we can observe a dramatic decrease of temperature on the left cheek (in reality the cheek surface temperature exhibits much less temperature variation), where the viewing angle is clearly larger than $70^{o}$ with respect to the IR camera axis. The temperature measurement is degraded due to the artifact of directional emissivity.

### 5.4.4 Computing the viewing angle for curvature artifact correction

In Step 4 in Fig. 5.7, the viewing angle distribution over the reconstructed 3D surface is computed using Eq. 5.13, and the result is presented in Fig. 5.10. Using the data for the 3D distribution of the viewing angle, the three directional emissivity correction formulas were applied to the raw 3D IR thermal map, resulting in three accurate 3D IR thermal maps displayed in Fig. 5.11.

As discussed in Chapter 4, in addition to the viewing angle of object, the correction effect depends on the directional emissivity model used. In our experiment the raw 3D IR thermal map is corrected using the three models introduced in Section 4.4.5, the dielectric model [67], the non-dielectric [106], and the cosine model. Results for these three models are displayed in Figs. 5.11(a),(b), Figs. 5.11(c),(d), and Figs. 5.11(e),(f), respectively. When applying correction formula, the room temperature of 23°C was used as the ambient temperature $T_a$ in Eq.4.14. The temperature at the location with the viewing angle close to 0° (red arrow in Fig. 5.10), was taken as the $T_s(\theta = 0)$ in Eq.4.15.

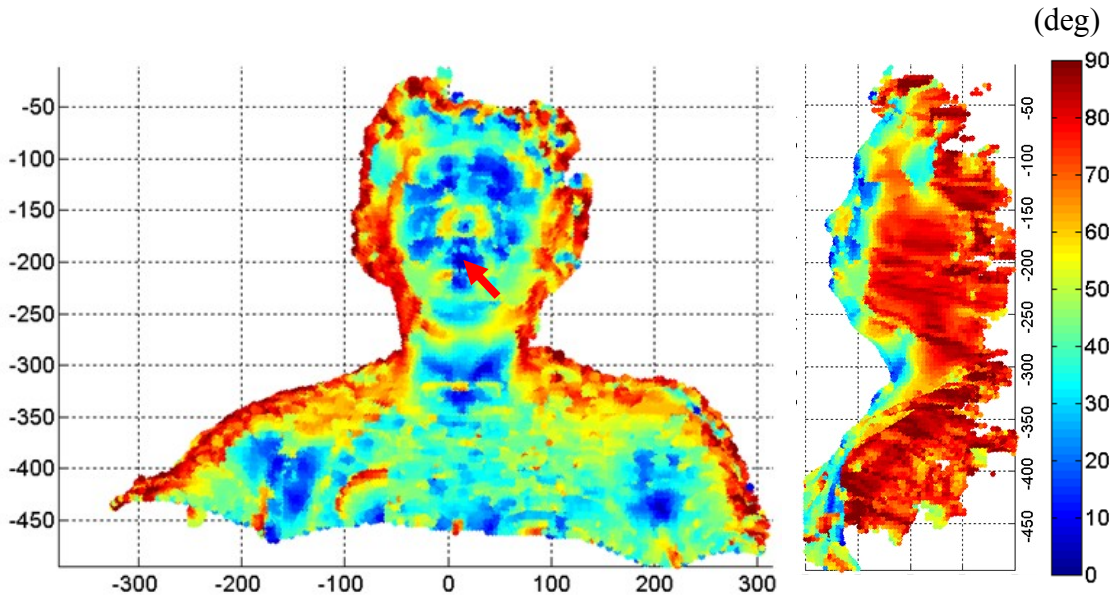


**Figure 5.10** Viewing angle distribution of the reconstructed 3D surface computed by Eq.5.13. The red arrow indicates the location with a viewing angle close to 0°, the temperature at this location is used as the denominator: $T_s(\theta = 0)$ in Eq.4.15 to determine the calibration coefficient *S*.

The three sets of corrected 3D thermal maps in Fig. 5.11 allow us to compare the correction effects generated by the three directional emissivity models. We can observe that in regions with large viewing angles, such as the cheeks, the temperature decreases dramatically in the raw 3D thermal map, as shown in Fig.5.9. The temperature in these regions is effectively recovered in Figs. 5.11(a),(b) (dielectric model) and Figs. 5.11(c),(d) (non-dielectric model). We can also observe that the temperature of the skin corrected by these two models becomes more uniform than the uncorrected distribution (Fig. 5.9). By comparing Figs. 5.11(a),(b) with Figs. 5.11(c),(d), we can conclude that the skin temperature is slightly higher for the non-dielectric model in regions with larger viewing angles (side view). This suggests that the non-dielectric model yields a slightly stronger temperature compensation than the dielectric model. The skin temperature corrected by

cosine model, however, is clearly over-compensated, as illustrated in Figs. 5.11(e),(f), and the facial features even lose the original thermal contrast in the corrected 3D thermal map. The result implies that the cosine function is not a suitable model to describe the directional behavior of skin emissivity. The use of the cosine model may be appropriate in some engineering applications when directional emissivity data are unavailable, however, better models are available for skin properties in medical applications.

To further improve the accuracy of 3D thermal mapping of the human body for medical applications, a systematic experimental study of the directional emissivity would be essential, to validate existing models and develop better models. This study should measure directional emissivity for different skin types and evaluate the influence of factors such as age, hydration level, etc. on the directional emissivity of the human skin.

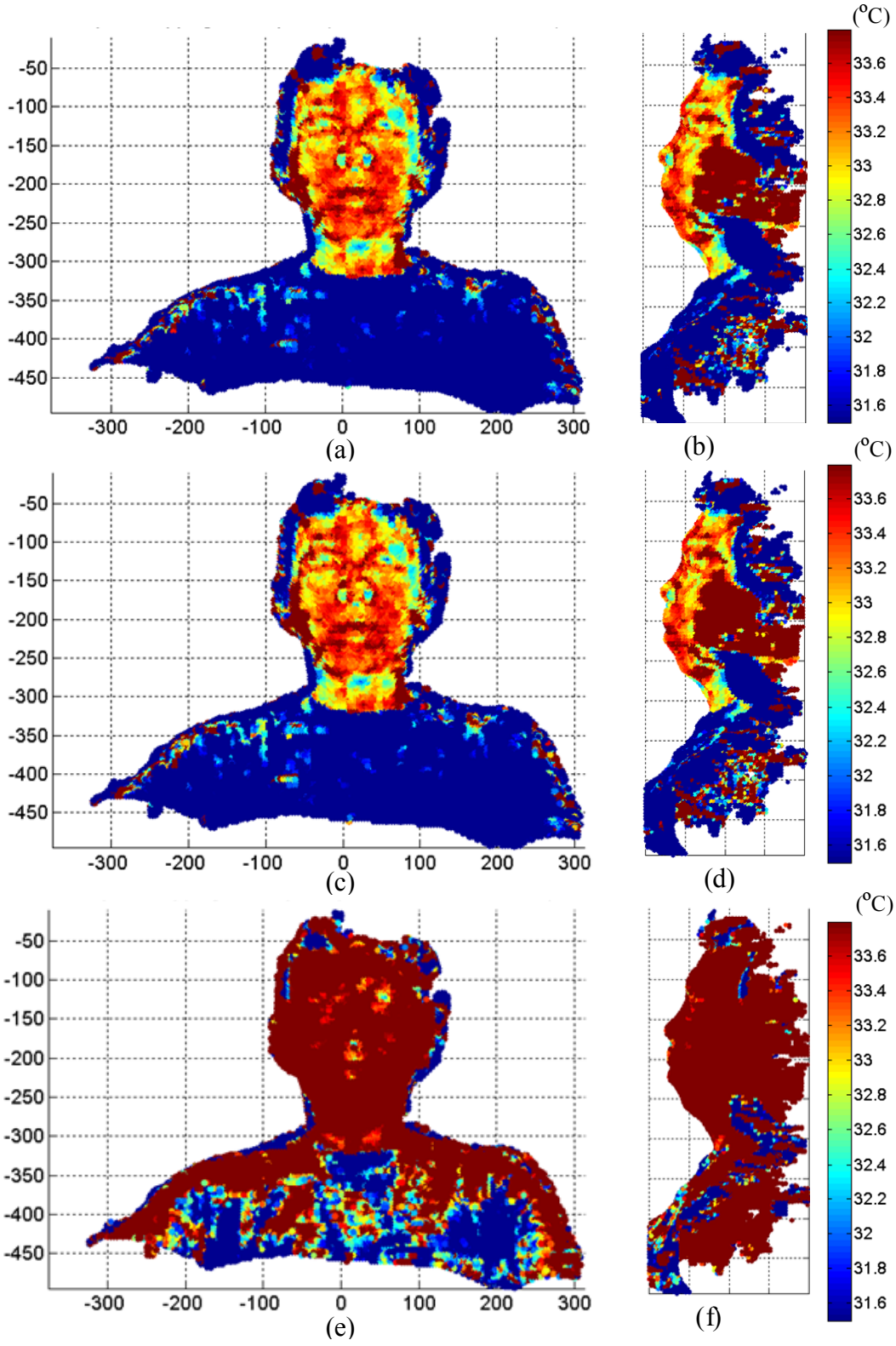


**Figure 5.11** Front view (a) and side view (b) of 3D thermal map corrected by the dielectric model. Front view (c) and side view (d) corrected by the non-dielectric model and the front view (e) and side view (f) for the cosine model.

To evaluate the correction effects quantitatively, we selectively projected the corrected temperature of the face from the 3D space back into 2D image coordinates. The results of back-projection without correction, results corrected by the dielectric model (Figs. 5.11(a),(b)), and the non-dielectric model (Figs. 5.11(c),(d)) are shown in Figs. 5.12(a),(c) and (e), respectively. In the back-projection, temperature profiles along two horizontal lines across the face are shown in Figs. 5.12(b) and (d), where Fig. 5.12(b) illustrates temperature along the line crossing the forehead region (blue line in Figs. 5.12(a),(c),(e)). Fig. 5.12(d) displays temperatures along the line crossing the nose and two cheeks (green line in Figs. 5.12(a),(c),(e)).

The dashed line in Figs. 5.12(b) and (d) shows results without correction, and we can observe the pronounced decrease of temperature toward the two ends of the profile, as the surface of cheek region gradually points away from the camera axis. Conversely, the in profiles corrected by the dielectric and non-dielectric models (the solid and solid-dot lines in Figs. 5.12(b) and (d)), the temperature is more uniform toward the two ends of the profile. The temperature profile corrected by the non-dielectric model shows a stronger compensation. By subtracting the temperature profile of the uncorrected case (the dashed line in Figs. 5.12(b) and (d)) from the two corrected profiles (the solid and solid-dot lines in Figs. 5.12(b) and (d)), the temperature difference generated by the correction formula using the two models is contrasted in Fig. 5.12(f). We can observe that at the location with higher viewing angles (nose and temple regions), the temperature compensation provided by the correction formula is more significant. The magnitude of temperature compensation along the two lines is in the range of 0.2-1.4 $^{o}$C.

Finally, to evaluate the validity of the correction formulas, we acquired the 2D IR image for the side view (profile) of the subject's face as shown in Fig. 5.13(a). The left cheek in Fig. 5.13(a) was facing the IR camera, and thus the temperature distribution of the cheek can be scanned without the interference of the viewing angle artifact. For comparison (with Fig. 5.13(a)), the side views of the reconstructed 3D IR thermal maps before and after applying the correction (Fig. 5.9(b), Fig. 5.11(b) and Fig. 5.11(d)), are also displayed in Figs. 5.13(b)-(d). When compared with the uncorrected 3D IR thermal map (Fig. 5.13(b)), we can observe that the temperature distributions corrected either by the dielectric (Fig. 5.13(c)) or non-dielectric models (Fig. 5.13(d)) exhibit features more similar to the 2D IR image in Fig. 5.13(a). Particularly in the region of the temples and the jaw in Fig. 5.13(a) we can find that some hot spots originally degraded by the viewing angle artifact in Fig. 5.13(b), were recovered and become visually identifiable in Figs. 5.13(c) and (d). Therefore, the proposed four-step correction formula using the dielectric and non-dielectric models does improve the quantitative accuracy of 3D thermal mapping.

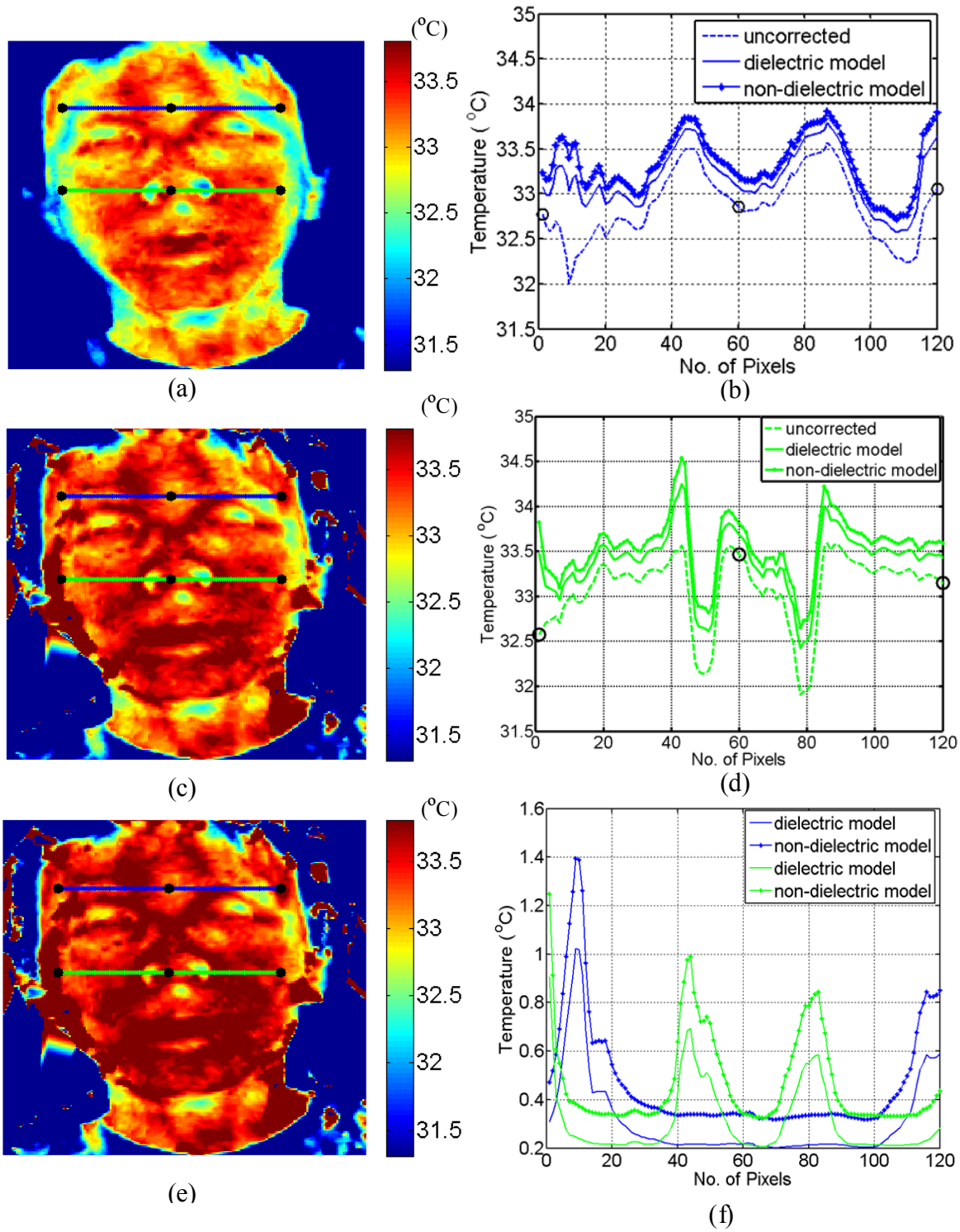


**Figure 5.12 (Left)**: 2D projection of the 3D thermal map of the face: (a) without correction, (c) correction using dielectric model and the (e) non-dielectric model. **(Right)**: (b) Temperature profiles along the blue lines shown in (a)(c)(e). (d) Temperature profiles along the green line shown in (a)(c)(e). (f) Temperature difference between the corrected profiles and the uncorrected profile (subtracting the dashed line from the solid and solid-dot lines in (b) and (d)).

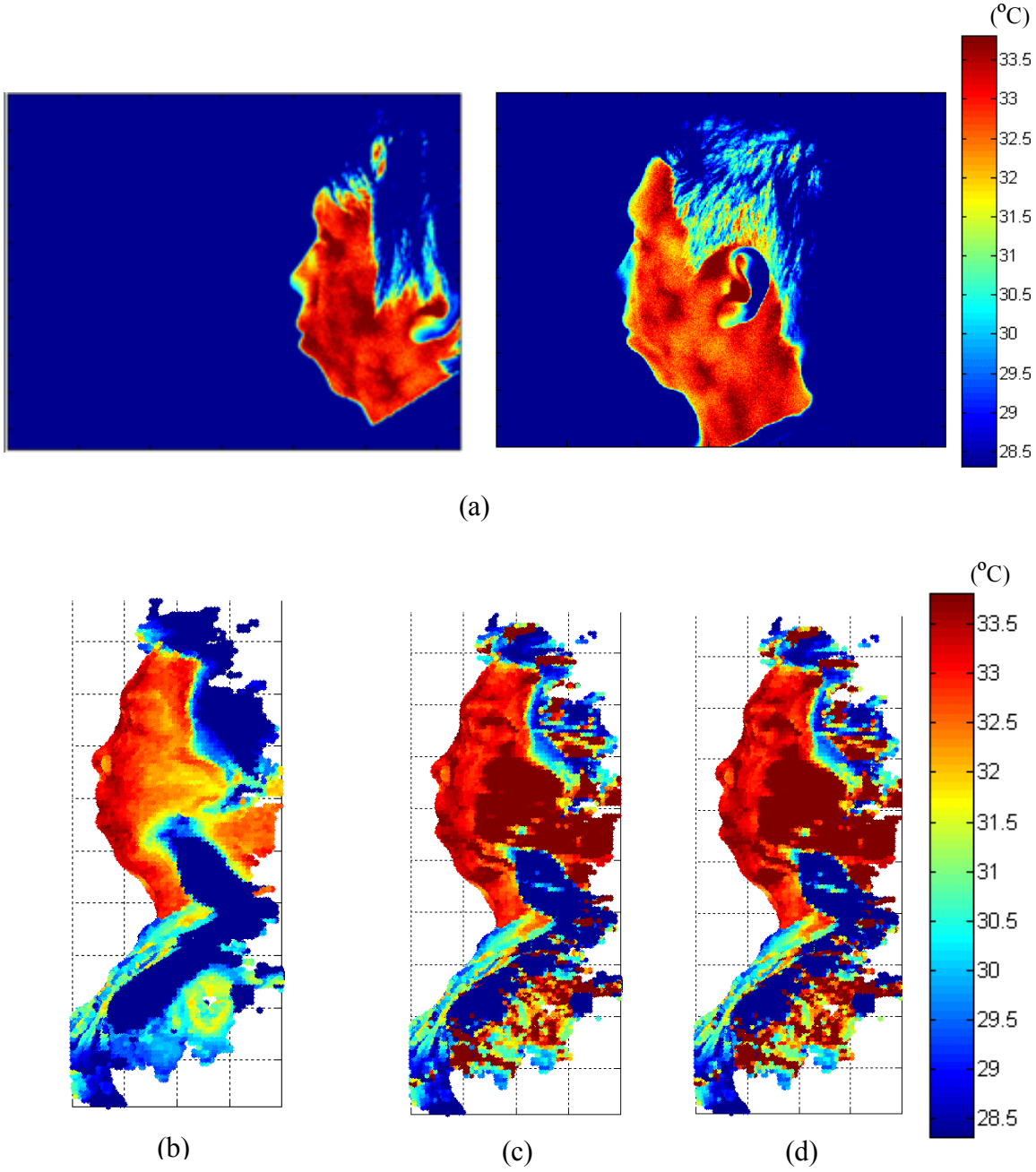


**Figure 5.13** (a) 2D IR image of the side view of face. The image was acquired with the cheek facing the IR camera. (b) Side view of the raw (uncorrected) 3D IR thermal map. Side view of the 3D IR thermal map corrected by the (c) dielectric model and (d) the non-dielectric model.

## 5.5 Discussion and conclusions

In this chapter, we successfully implemented 3D imaging of the human body by integrating the functionalities of the Microsoft Kinect 3D imager and the IR camera. This off-the-shelf hardware, combined with custom-developed and open-source software, serves as a low-cost platform for clinical imaging applications. The resulting 3D thermal images of the skin combine the 3D spatial locations of the body surface with the corresponding temperature texture. The results reveal that the 3D imager of the Kinect, that uses structured light, yields reasonable reconstruction accuracy for 3D skin temperature measurements. Intrinsic and external camera parameters obtained from the checkerboard calibration [130, 131] were employed to project the 3D surface grid to the IR image coordinates. The successful mapping of the thermal texture onto the reconstructed 3D depth map of the face demonstrates the validity of the calibration method introduced by Herrera et al. [130, 131].

One of the key challenges in quantitative medical diagnostic applications of IR thermography is the relatively large systematic measurement error (it can be of the order of 3-4$^{o}$C, depending on the viewing angle and experimental conditions) introduced by applying flat plate blackbody calibration results to IR images of curved surfaces. The 3D surface map generated by the Kinect imager provides the information necessary to correct for artifacts appearing on curved surfaces due to the directional properties of surface emissivity. The viewing angle distribution over the body surface is computed from the surface normal vector orientation for the reconstructed 3D surface grid relative to the camera axis. A four-step approach to correct the viewing angle artifact is then applied to

yield the 3D temperature distributions. According to the visual comparison of the 3D temperature distributions generated by 3D IR thermal map before and after correction, we can observe the skin region influenced by the directional emissivity artifact is reduced. In the corrected images the temperature changes more smoothly toward the regions with larger viewing angles. The resulting temperature patterns display higher similarity to the artifact-free temperature pattern in the 2D IR scan of the profile than those from uncorrected IR thermal map.

Due to incomplete data on the lateral side of a single 2D IR frontal image of the face, in some cases the temperature at a lateral location, such as the ear, is not reconstructed fully in 3D IR thermal map. In addition, since the temperature texture on the 3D surface is computed by interpolation based on 2D IR image data, the spatial reconstruction accuracy is limited by the spatial resolution of the IR camera. The spatial resolution of temperature measurements decreases with increasing viewing angle as a larger surface area is covered per pixel at larger viewing angles. Thus, the resolution of 3D thermal map will improve when a 2D IR image with higher spatial resolution is used for reconstruction. The rapid development of IR technology holds the promise that high-resolution IR imagers will be available on the market at a reasonable cost in the near future. Furthermore, the foreseeable improvement of 3D depth resolution delivered by the new generation of Kinect devices will improve the accuracy of viewing angle mapping, leading to a more accurate correction and improved thermal map.

The inaccuracy caused by the incomplete projection can be improved by scanning multiple views of the human body. This allows the merging of different 3D depth profiles and 2D IR views into a complete 3D IR reconstruction. Multiple orientations provided by

the multiple views can also be used for mutual calibration of the correction formula: temperature measured at the location with large viewing angle in one view, can be calibrated by its corresponding value in another view. The reference value used in the calibration is measured at a location facing the camera with zero viewing angle.

The designed imaging hardware system, which consists of one Kinect device and one IR camera, only needs to be calibrated once, and then the camera parameters obtained are reusable in subsequent measurements. The portability of the system also makes it suitable for the clinical environment. The convenience and the affordability of the system designed in this study makes it a promising solution to enable 3D IR thermographic imaging in medical as well as industrial applications.

# Chapter 6

# Clinical case studies of in-vivo infrared imaging

## 6.1 Overview

The aim of this chapter is to analyze the thermal signatures of different types of skin lesions by capturing infrared images in a clinical setting. We analyzed clinical IR images previously acquired in two patient studies: one study focused on pigmented skin lesions suspicious of melanoma and in the second study vascular tumors classified as infantile hemangioma were evaluated.

The use of dynamic IR imaging for the early detection of melanoma was originally introduced in Chapter 2, and in this chapter the motion tracking approach developed in Chapter 3 is implemented to improve the accuracy of data obtained by dynamic IR imaging. Another application of the imaging tools developed in this study is the assessment of infantile hemangiomas, which are the most common vascular tumors in

infancy with the incidence ranging from 1% to 10% of the population[133-136]. While most hemangioma tumors are benign, tumors located in the critical areas such as the airway can lead to functional deficit [133, 134], and tumors located on the face lead to cosmetic problems. Since infantile hemangioma tumors are highly vascularized, the increased blood flow through the lesion leads to a locally elevated temperature, which makes hemangiomas uniquely suited for IR thermographic assessment.

In this chapter we propose a variety of quantitative image analysis techniques suitable for the assessment of both static and dynamic IR imaging data for different types of skin lesions. As discussed in Chapter 2, the temporal evolution of the thermal contrast between the lesion and healthy tissue obtained by dynamic IR imaging is of interest for the early detection of melanoma [2-8, 55]. As for hemangiomas, the steady-state distribution of skin temperature presented in the static IR images is informative to estimate the tumor size, since the full volume is difficult to assess due to the presence of its deep components. The thermal signature observed in the static IR image also allows to evaluate the effect of treatment on hemangiomas.

## 6.2 Patient studies

### 6.2.1 Pigmented skin lesions

In order to assess pigmented skin lesions, we analyzed dynamic IR image sequences previously acquired in the patient study conducted in the fall of 2009 [4], in the Department of Dermatology Pigmented Lesion Clinic at the Johns Hopkins Hospital

Outpatient Center. The Institutional Review Board (IRB) protocol was approved by the Johns Hopkins Medical Institution IRB (protocol: NA00016040, Using High Resolution Functional Infrared Imaging to Detect Melanoma and Dysplastic Nevi). More details about the clinical study are described in [4]. The IR images analyzed in this chapter were collected from two unique subjects in the study.

### 6.2.2 Infantile hemangioma tumors

The IR images of infantile hemangiomas were acquired in the patient study conducted during fall of 2012 - spring 2013 in the Department of Dermatology at the Johns Hopkins Medical Institutions (protocol: NA_00014694, Retrospective Study to Measure Treatment Outcomes of Vascular Anomalies, and Pediatric Interventional Radiology Procedures). In this chapter, we analyzed IR images acquired from four unique subjects in the study.

## 6.3 Methods

### 6.3.1 Equipment and image acquisition

IR images in the two patient studies were all acquired by the - Merlin® midwave (FLIR System Inc., Wilsonville, OR) infrared camera, which records images in the spectral range of 3-5μm. The detailed specifications and calibration procedures of the infrared camera are described in Chapter 3 (Section 3.3.4) and Chapter 4 (Section 4.4.1).

Additionally, a digital camera - Canon PowerShot G11™ (Canon U.S.A., Inc., One Canon Park, Melville, NY), was also used to acquire the white light image of skin lesions.

During an image acquisition session, an adhesive square paper marker (described in Chapter 3) was first applied in the vicinity of the lesion, and then the white light image of the lesion (Fig. 6.1(a)) was acquired by the digital camera. In static IR image acquisition, a set of 20 infrared images of the lesion for steady-state conditions was acquired at the frame rate of 2 fps. In dynamic IR image acquisition, we first applied a gel pack (Fig. 6.1(b)) for 60 seconds to cool the lesion. After the gel pack was removed, an infrared image sequence of the lesion was acquired for 60-180 seconds at the frame rate of 2 fps, resulting in a sequence of 120-360 image frames. All image processing and analysis algorithms were implemented using MATLAB 2014 (MathWorks Inc., Natick, MA).

### 6.3.2 Motion tracking for dynamic IR imaging

In the analysis of the dynamic IR image sequence, we applied the template-based motion tracking algorithm developed in Chapter 3 to compensate for patient's involuntary movements. To implement the algorithm, we took the region of interest (ROI) extracted from the first IR image (Fig.6.1(c) and (d)) as the template image in the computation. With the aid of the motion tracking algorithm, any particular location on the skin can be automatically tracked throughout the IR image sequence. While the skin surface temperature is recovering from cooling, the thermal recovery at any particular location can thus be recorded for the subsequent analysis.

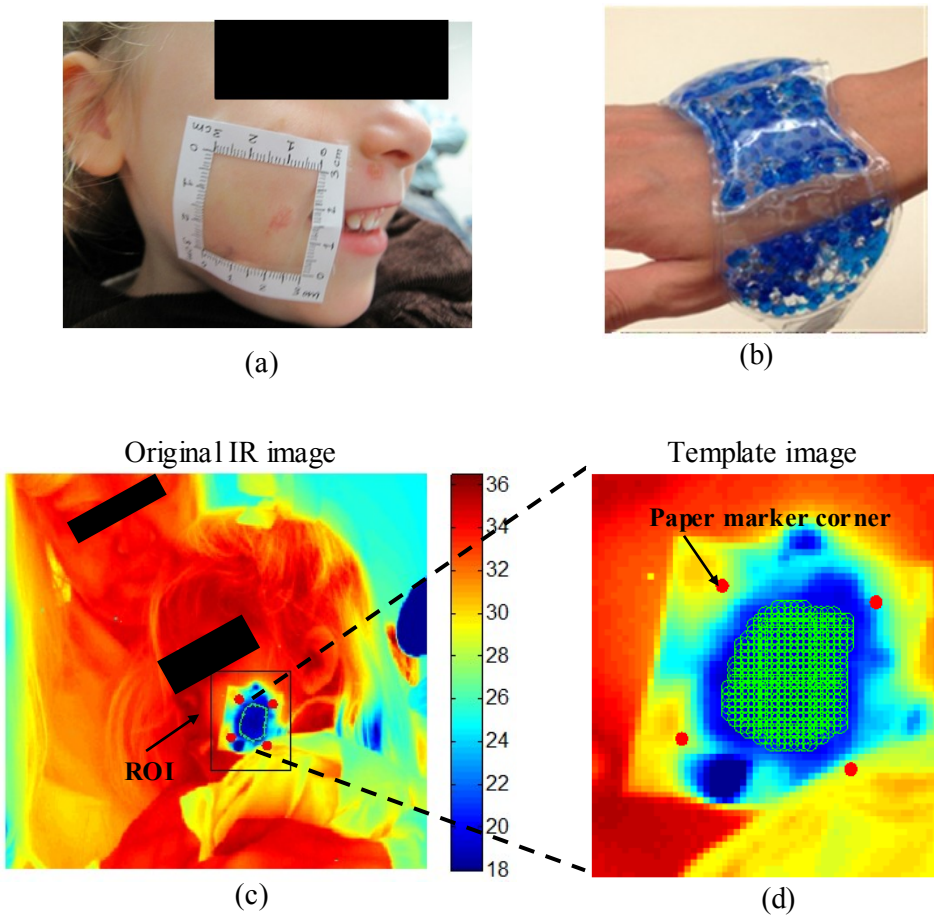


**Figure 6.1** (a) White light image of a skin lesion with the square paper marker. (b) Gel-pack used for cooling in dynamic IR imaging. (c) The first IR image frame (in the sequence) of the skin surface after applying gel-pack cooling. The ROI (marked by a black rectangle) serves as the template image in the motion tracking algorithm, and the area delineated by the green curve represents the lesion boundary registered from the white light image. (d) Template image used for motion tracking computations, grid points represent the pixels enclosed by the lesion boundary (green outline) in (c).

## 6.3.3 Lesion registration and segmentation in the IR image

The lesion area visible in white light photo may not be directly identifiable in the IR image because of low thermal contrast. To locate the area corresponding to the lesion in the IR image, an image registration method, the 2D projective transformation [96] (also

known as homography), was utilized in this study. The algorithm enables the coordinate registration for a planar object between two sets of 2D image coordinates, and it was originally introduced in Chapter 3 (Section 3.4.7) to register the simulated lesion between the white light and the IR image.

The implementation of this algorithm relies on the use of a square paper marker, which is visible in both white light (WL) and IR images (Fig. 6.1). We first located the four corners of the paper marker in both WL and IR images, as displayed in Fig. 6.2. This process was accomplished manually, but can be completed automatically via corner-detection algorithms[97, 98]. The coordinate correspondence relationship between the WL and IR images was established via the four corners of the paper marker. Using the coordinate correspondence of the four corners, the mathematical transformation between the two 2D image coordinates can be formulated. Specifically, for a point with pixel coordinates $[x, y]^T$ in the WL image, the 2D projective transformation is carried out by first converting $[x, y]^T$to the homogeneous coordinates $P_w = [x, y, 1]^T$ by simply adding unity to the third entry of $[x, y]^{\mathrm{T}}$.

In homogeneous coordinates, the coordinate transformation between the two cameras can be described by a $3 \times 3$ matrix $H$. Using the transformation matrix $H$, the point with coordinate $P_w$ in the WL camera frame is transformed to the corresponding point $P_i = [x', y', w]^T$ in the homogeneous coordinates of the IR camera as

$$P_i = H\, P_w \tag{6.1}$$

$$\rightarrow \begin{bmatrix} x' \\ y' \\ w \end{bmatrix} = \begin{bmatrix} h_1 & h_4 & h_7 \\ h_2 & h_5 & h_8 \\ h_3 & h_6 & h_9 \end{bmatrix} \begin{bmatrix} x \\ y \\ 1 \end{bmatrix},$$

where matrix $H$ has 8 degrees of freedom with nine elements $h_1 \ldots . h_9$. Therefore, given the four-point correspondence between two images with different perspectives, the nine elements in matrix $H$ can be determined using the direct linear transformation algorithm [96]. In our application, the four corners of the paper marker, which is visible in both WL and IR images, serve as the control points to formulate the equation of correspondence.

By multiplication of the vector $P_w = [x, y, 1]^T$ and the matrix $H$, we can obtain the 3D vector $P_i = [x', y', w]^T$, as shown in Eq.(6.1). This vector is defined in the homogenous coordinates of the IR camera. The 2D pixel coordinates in the IR image are recovered by dividing the first two entries of $P_i$, $[x', y']^T$, with the third entry $w$. Consequently, we obtain the 2D vector: $[x'/w, y'/w]^T$, which represents the 2D pixel coordinates in the IR image.

By assuming that the paper marker and skin lesion are approximately in the same plane, the transformation matrix $H$ obtained from registration process allows us to locate the visible portion of the lesion in the IR image. As shown in Fig. 6.2(a), the visible boundary of lesion was first segmented in the WL image. The segmentation was accomplished manually, but can be done automatically via the random walker algorithm [95], which was utilized in Chapter 3 (Section 3.4.7). After the lesion boundary is segmented in the white light image, the pixel coordinates of these boundary points can be transformed into the IR image, leading to the corresponding lesion location (contour) in the IR image illustrated by the green contour line in Fig. 6.2(b).

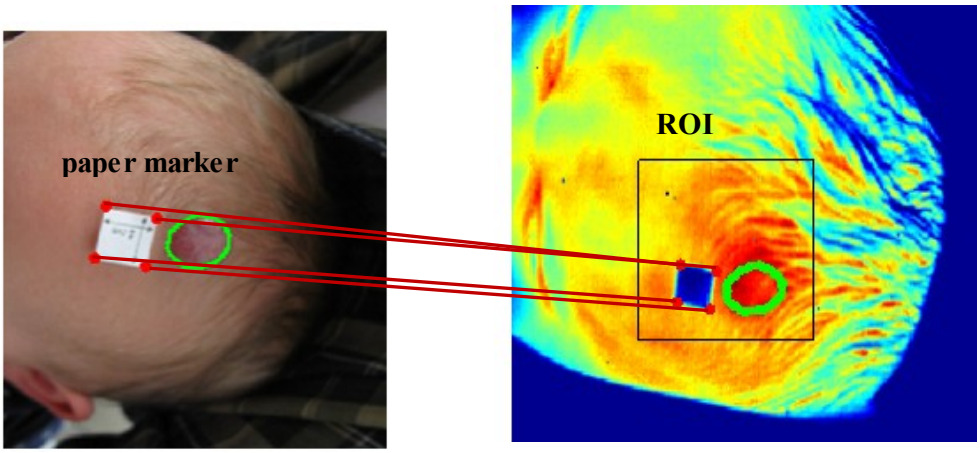


(a) (b)

**Figure 6.2** Registration of the hemangioma lesion between the WL and IR images. (a) White light image of the lesion with a square paper marker with the four corners (red points) and the lesion boundary (green contour line) marked. (b) IR image with the registered hemangioma lesion. The visible lesion boundary (green contour line) is registered using 2D projective transformation.

WL-IR registration allows us to segment the pixels contained by the lesion boundary (Fig. 6.1(d)) in the IR image, which can then be grouped statistically to calculate the mean temperature of the lesion. In addition, by knowing the number of pixels equivalent to the actual dimension of the paper marker, the total number of pixels segmented in WL and IR images enables us to estimate the actual dimension of hemangioma.

## 6.3.4 Mapping of isothermal contours in the ROI

After registering the lesion location in the IR image, the region of interest (ROI) is selected, as indicated by the black rectangle in Fig.6.3(a). The ROI contains the lesion area and surrounding healthy skin. In order to investigate the thermal signature of the

lesion, we applied mapping of isothermal contours to the ROI (Fig. 6.3(b)) as the basis to assess the affected area of hemangiomas. In the contour mapping, each line connects the pixels of equal temperature in the IR thermal map. The contour lines are mapped from low temperature to high temperature, with the temperature difference between two successive contour lines being constant.

The mapping of isothermal contours not only highlights the affected area, which corresponds to the high-temperature contours in the IR thermal maps (34°C or above in Fig.6.3(b)), but it also allows us to examine the thermal gradients around the lesion.

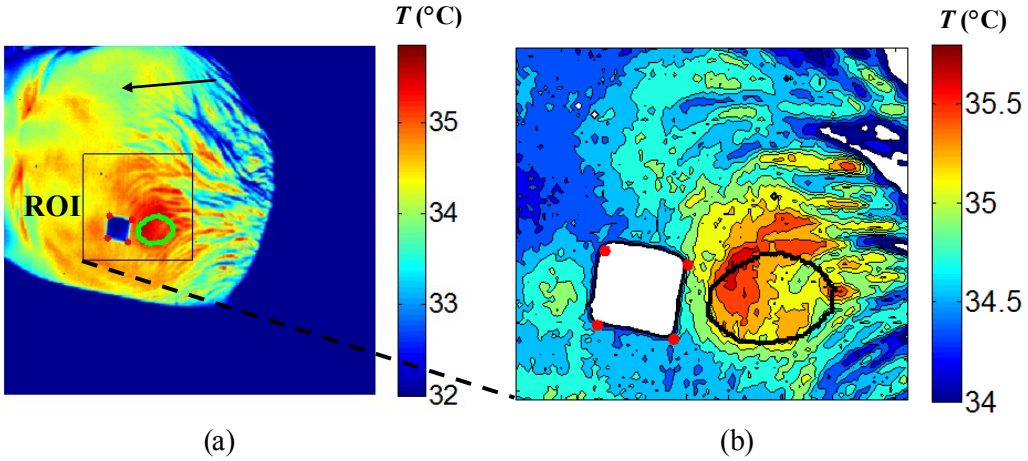


**Figure 6.3** (a) Color coded IR image with a black rectangle representing the selected ROI, which contains the lesion boundary (green contour) registered from white light image. (b) Mapping of isothermal contours for the selected ROI (34°C is used as the baseline temperature for color coding).

## 6.3.5 Calculation of the size of the affected area in IR images

Based on the isothermal contours mapped in the ROI (Section 6.3.4), we can also quantify the size of the affected area in the units of pixels by thresholding the temperature contours. As shown in Fig 6.4(a), 34°C is taken as the baseline (healthy issue)

temperature to plot 3D temperature profile for the ROI in Fig.6.4(b). Contour mapping of the temperature elevation relative to 34°C is displayed in Fig 6.4(c). From the temperature elevation map in Fig.6.4(c), the areas enclosed by the contours with temperature elevation $\Delta T \geq 1.5°C$, 2.0°C, and 2.2°C are presented in Figs. 4.(d),(e), and (f), respectively. These results suggest that the process allows us to measure the skin area having temperature elevation between two selected temperature levels.

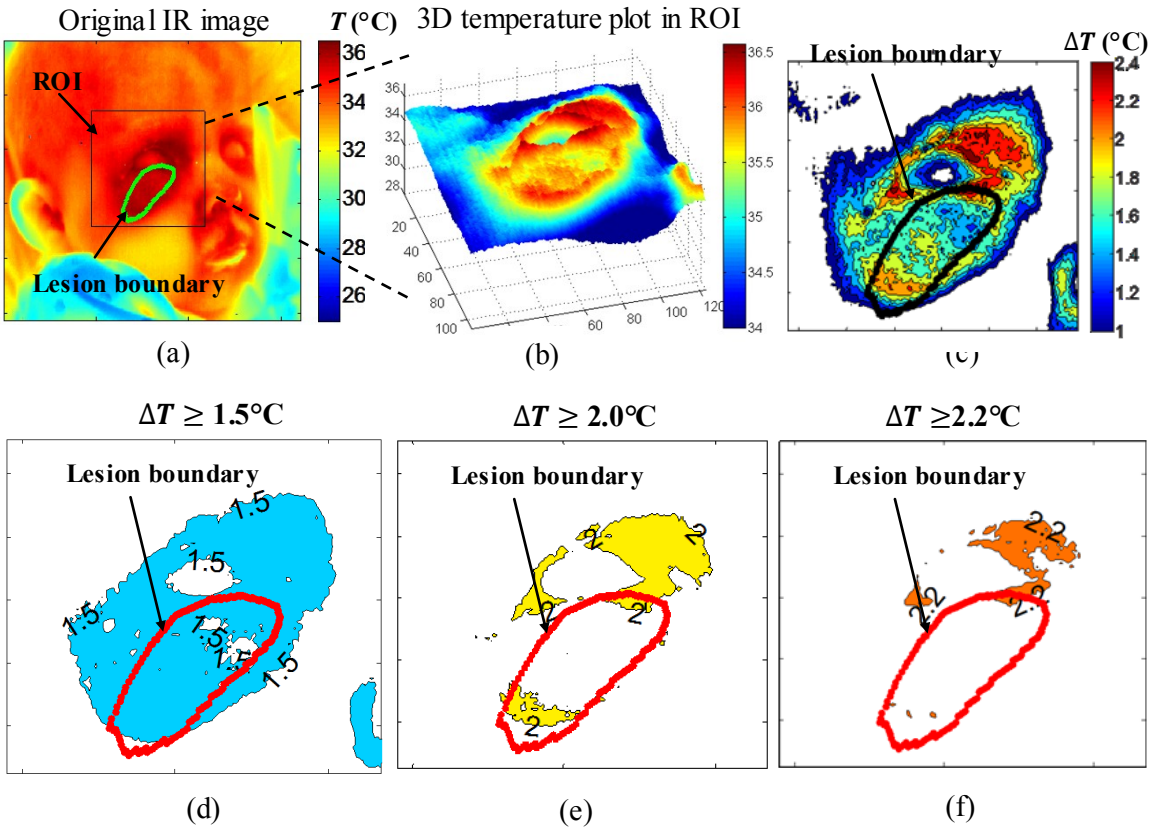


**Figure 6.4** (a) Original IR image from which the ROI is extracted. (b) 3D plot of the temperature distribution in the ROI using 34°C as the baseline temperature: visualization of the temperature elevation as the height in the 3D space. (c) Contours of temperature elevation within the ROI, obtained by subtracting the temperature contour with the base temperature of 34°C. (d)–(f) Areas corresponding to the pixels enclosed by the elevation contours (c) $\Delta T \geq 1.5°C$, 2.0°C, and 2.2°C with respect to 34°C, respectively.

## 6.4 Results

### 6.4.1 Dynamic IR imaging of melanoma with motion tracking

By implementing the motion tracking algorithm from Chapter 3, the dynamic IR image sequence of a malignant melanoma lesion (P04, Clark's level II, superficial spreading type, more details in [4]) is illustrated by six frames in Fig 6.5(a). The template image extracted from the first frame is also presented. To capture the transient, 90 IR images were acquired during the thermal recovery phase for the duration of 180 seconds immediately after the removal of gel-pack cooling. The locations of the lesion and healthy tissue registered in the IR images and are marked by green and black points in Fig.6.5(a), respectively. The direction of the patient's involuntary motion with respect to the first frame (0 s) is indicated by white arrows in each frame. The mean temperatures of the segmented pixels (9 pixels) within the lesion (green) and healthy tissue (black) regions were determined as a function of time and plotted in Fig.6.5(c). To contrast the improvement achieved by the motion tracking method, temperature data without applying the motion tracking are presented in Fig.6.5(b).

With motion tracking on, we observe that the green (lesion) and black (healthy) points in Fig.6.5(a) track the same locations on the skin throughout the IR image sequence, despite of the motion of the subject. In this way motion tracking enables accurate recording of the temperature over time during thermal recovery at any particular location, resulting in the smooth temperature profiles shown in Fig.6.5(c). The thermal contrast is presented in Fig.2.13(b) in Chapter 2. Without motion tracking (Fig.6.5(b)) the resulting temperature profiles exhibit significant fluctuations and essentially overlap, thus

failing to track the recovery temperature at the locations of interest consistently. The results suggest that motion tracking is essential for accurate measurements of temperature evolution of human subjects in clinical practice of dynamic IR imaging.

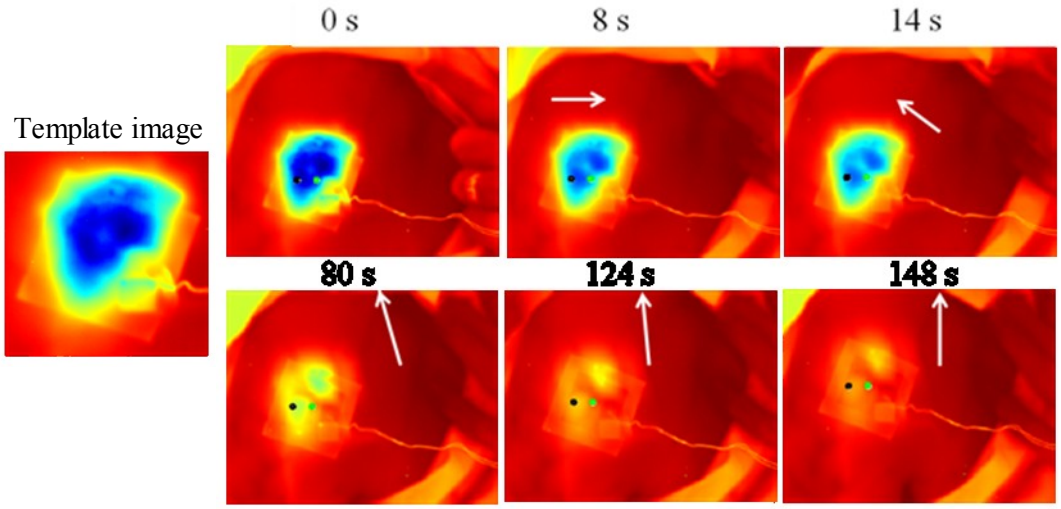


(a)

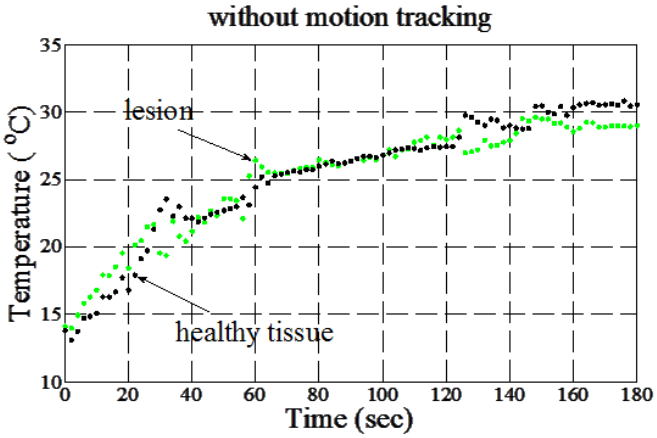


(b)

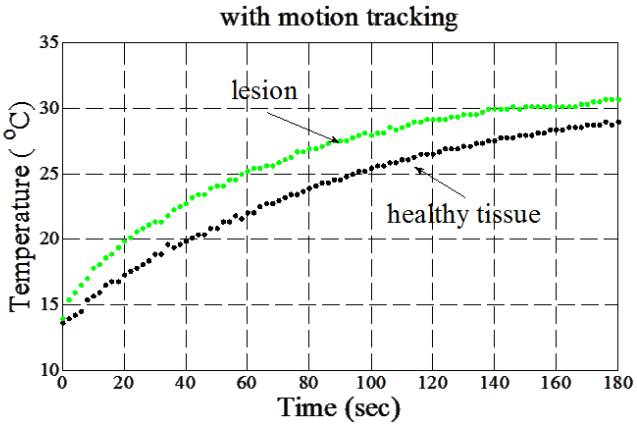


(c)

**Figure 6.5** (P04): (a) IR image sequence of the melanoma lesion during the thermal recovery phase after the removal of cooling (green dots: lesion, black dots: healthy tissue, arrows: motion direction). Mean temperatures of the lesion (green dots) and the surrounding healthy tissue (black dots) during the thermal recovery, (b) recorded without motion tracking and (c) with motion tracking.

### 6.4.2 Visualization of thermal recovery by IR image subtraction

The successful implementation of motion tracking in dynamic IR images enables us to apply another quantitative technique, image subtraction on the region of interest (ROI), which is consistently tracked by the motion tracking algorithm over the IR image sequence. The technique subtracts the intensity of the first IR image from subsequent frames in the same image sequence, thereby contrasting the temperature evolution within the region over time. We selected a pigmented lesion, an atypical compound nevus (Fig.6.6(b), labeled as P12 in the patient study), to implement this technique.

Fig.6.6(a) shows the IR image frame acquired at 30 seconds into the thermal recovery phase. The ROI of this image after subtraction of the ROI of the first IR image frame (0 s), is shown in Fig.6.6(c). By repeating the same subtraction over the entire IR image sequence the evolution of the temperature change of the lesion during thermal recovery is visualized. Figs.6.6(d)-(f) illustrate the ROIs after subtraction in frames from 60 to 160 seconds into the thermal recovery phase.

Image subtraction contrasts the rise of temperature over time with respect to the first frame. In Figs.6.6 (c)-(f) we can track the region recovering from cooling, whereas the color of the regions outside the cooling spot remains static. Furthermore, in Figs.6.6 (e) and (f) we can also observe as the pattern of the lesion (see Fig.6.6(b)) gradually appears, as the temperature elevation exceeds 10°C. This means the temperature within the lesion area recovers faster than the surrounding healthy skin.

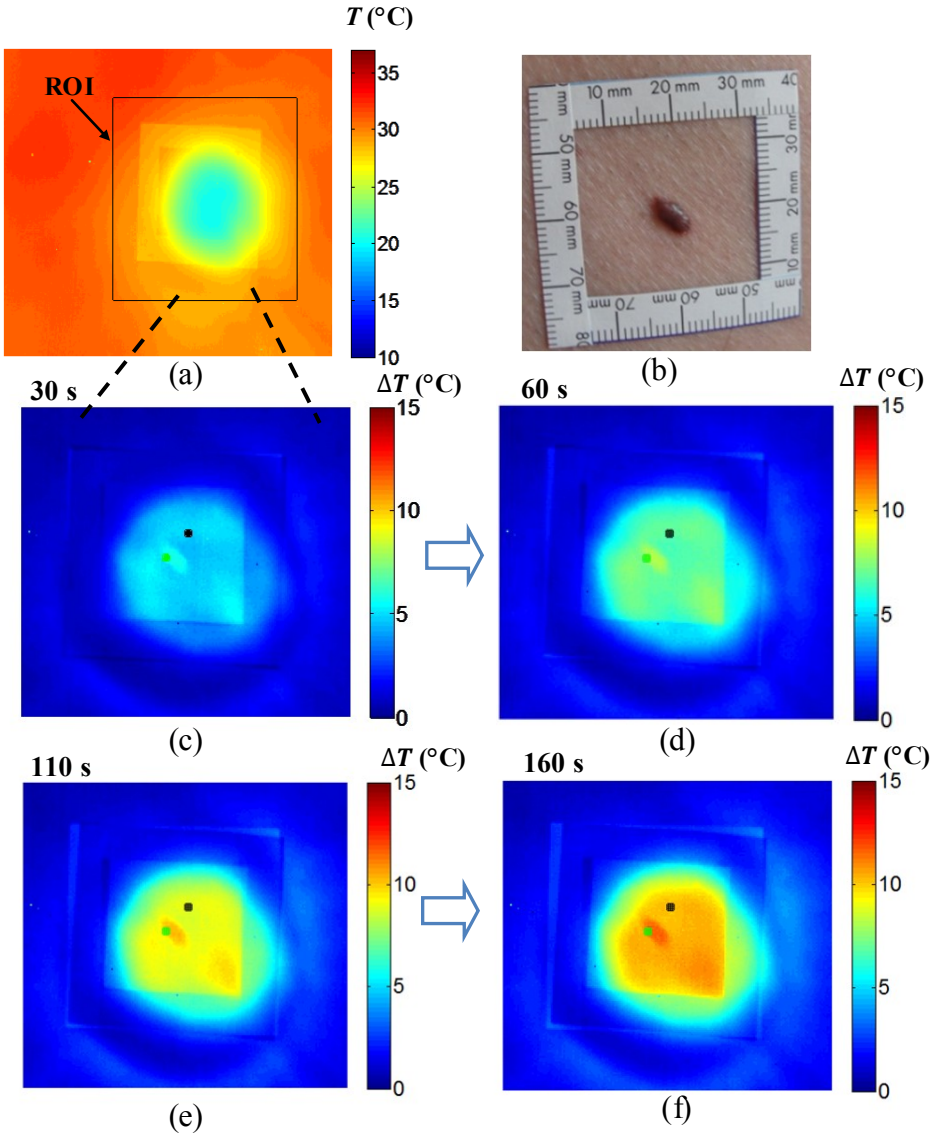


**Figure 6.6** (P12): Visualization of transient thermal contrast using image subtraction. (a) IR image of the skin lesion acquired at 30 seconds into the thermal recovery phase. (b) White light image of the skin lesion. (c) ROI of (a) after subtraction of the first frame of the image sequence. ROIs after subtraction in three subsequent IR image frames at (d) 60 s, (e) 110 s, and (f) 160 s during the thermal recovery phase. The green and black dots represent the registered locations of the lesion and healthy tissue, respectively.

### 6.4.3 Measurement of hemangioma dimensions using static IR imaging

The analysis of static IR images of hemangiomas is illustrated by two case studies (S44 and S20) from our patient study. Key results are summarized in Fig.6.7 and Fig. 6.8. Patient S44 had a superficial, focal hemangioma on the left scalp as shown in the white light photo in Fig.6.7(c). Using the dimensions of the paper marker (1cm ×1cm) as reference, the visible area of the lesion was determined to be approximately 1.2 $cm^2$. Fig.6.7(a) shows the static IR image of the lesion acquired at steady state with the green contour corresponding to the outline of the visible portion of the lesion, and the black rectangle indicating the ROI. Fig 6.7(b) shows the magnified ROI with the contour map of the visible lesion boundary (black contour), registered from the white light (WL) photo in Fig.6.7(c). We can observe that the maximum temperature in the lesion area is 35.8 °C, and the surrounding healthy skin is 34.0 °C during the measurement.

Fig.6.7(d) shows the contours of temperature elevation (compared to the surrounding healthy skin temperature) $\Delta T$ in the ROI using the base temperature of 34.0 °C. We can see that the visible area of the lesion is 1.2-1.8 °C warmer than the healthy skin. The subcutaneous area of the hemangioma (regions of increased vascularity around the visible boundary of the superficial lesion) is 1.0 – 1.4 °C warmer than the healthy skin. Moreover, by counting the total number of pixels enclosed by the contour $\Delta T \geq 1.0$°C, we can estimate the dimensions of the subcutaneous area (based on scaling using the dimensions of the paper marker}. We found that the subcutaneous area was approximately 2.0 $cm^2$, which is around 1.67 times larger than the area of the visible (superficial) lesion (1.2 $cm^2$). Therefore, the analysis of the IR image suggests that the

actual area impacted by the hemangioma is larger than the superficial portion of lesion visible in the WL image.

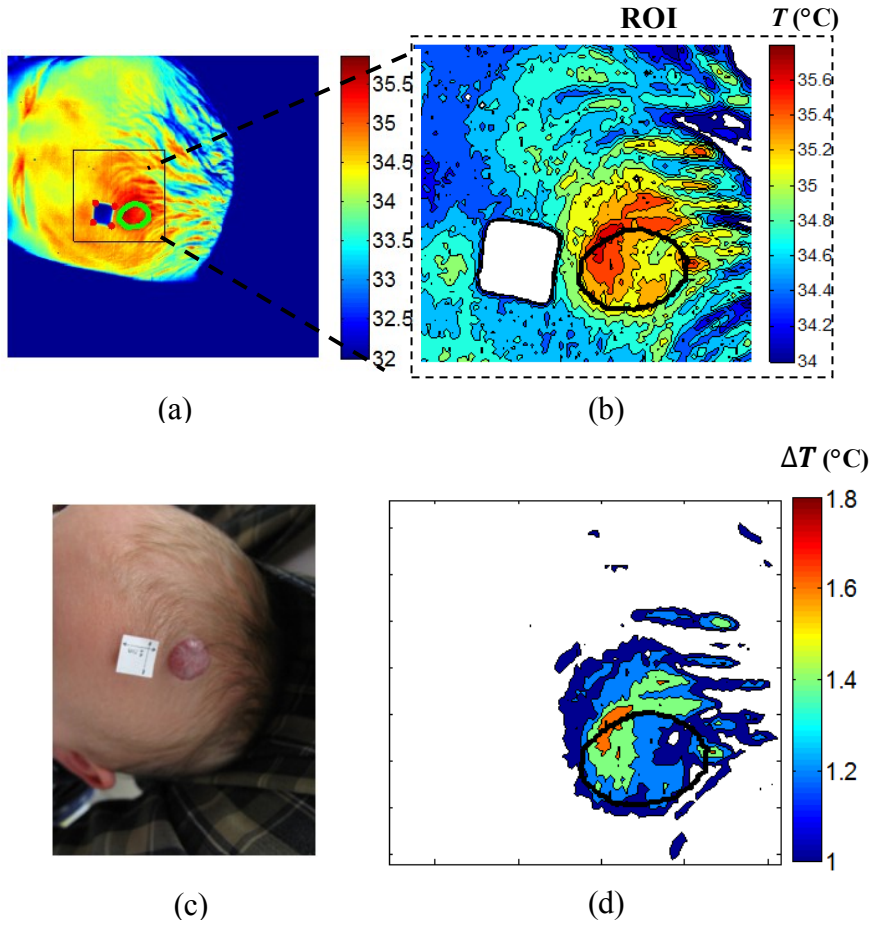


**Figure 6.7** (S44): (a) Color-coded IR image of the lesion. (b) Map of isothermal contours in the ROI. (c) WL image showing the visible (superficial) component of the hemangioma lesion. (d) Contour map of temperature elevation relative to 34.0 °C in the ROI. The measured temperature elevation $\Delta T$ is in the range of 1.0°C – 1.8°C.

Figure 6.8 illustrates the IR image analysis of the hemangioma lesion for subject S20 (Figure 6.8(a)). As shown in the white light photo in Fig.6.8(c), the subject had a deep, focal hemangioma on the glabella at the time of the initial imaging. The area of the visible region of the lesion is around 1.0 $cm^2$.

The IR images shown in Figs.6.8(a) and (b) indicate the maximum temperature of the lesion is about 36.1 °C, and the healthy skin is about 34.0 °C during the measurement. The contours of temperature elevation in Fig.6.8(d) indicate that the superficial lesion is 1.4-2.0 °C warmer than the surrounding healthy skin, and the subcutaneous lesion is warmer than the surrounding healthy skin by 1.0 – 1.6 °C. Similar to S44, the IR image of S20 exhibits a larger hyperthermic affected area, beyond the boundary of the superficial lesion visible in the WL image. By counting the number of pixels enclosed by the contour $\Delta T \geq 1.0$°C of the region exhibiting temperature elevation, we found that the size of affected area is approximately 4.1 $cm^2$, which is about four times larger than the visible lesion area observed in the WL image.

Again, the results reveal that IR imaging is capable of identifying the entire area impacted by the hemangiomas. Especially in patients having a deep lesion, such as S20, the affected area is likely to be underestimated if considering the visible portion of lesion in the WL image only. Visual inspection alone would also underestimate the affected surface area. Quantitative data from the image analysis of the two cases are summarized in Table 6.1. From the ratio of $Area_{IR}/Area_{WL}$ in Table 6.1, we can observe that in both two cases the affected area measured in the IR image is larger than superficial area visible in the WL image.

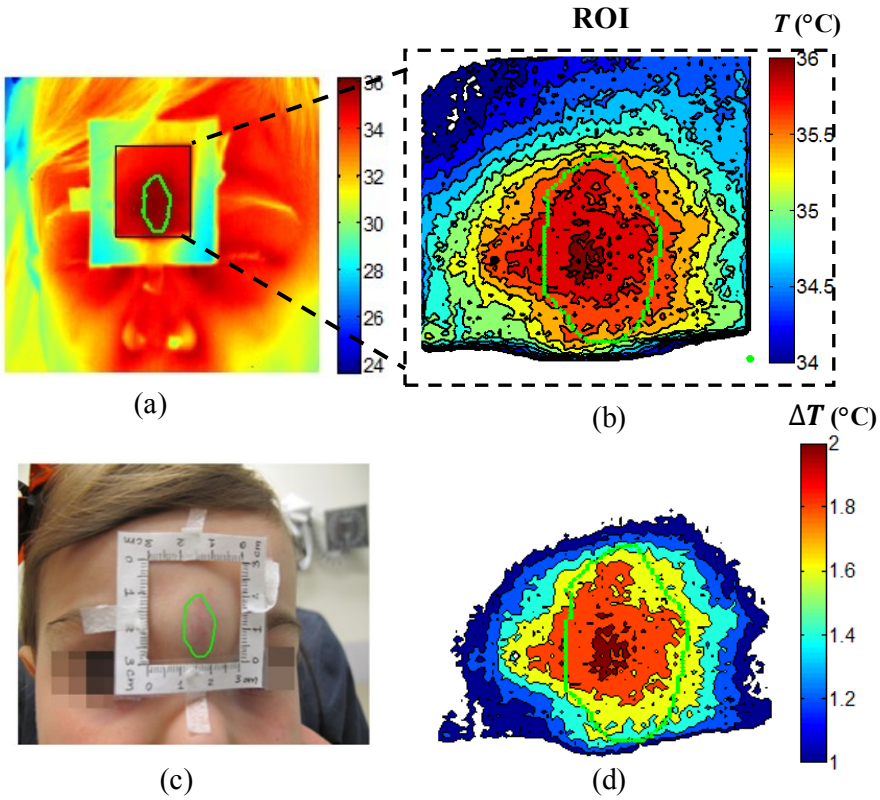


**Figure 6.8** (S20): (a) Color-coded IR image of the lesion. (b) Isothermal contour map in the ROI. (c) WL image showing the visible component of the hemangioma lesion (green contour line) with a square paper marker. (d) Contours of temperature elevation with respect to 34.0 °C in the ROI. The measured temperature elevation is in the range of 1.0°C – 2.0°C.

**Table 6.1** Summary of hemangioma characteristics for S44 and S20

| Case No. | Lesion Description | Maximum Temperature, $T_{max}$ (°C) | Temperature Elevation, $\Delta T$(°C) | $Area_{WL}$ ($cm^2$) | $Area_{IR}$, ($cm^2$) | Area Ratio ($Area_{IR}$ / $Area_{WL}$) |
|---|---|---|---|---|---|---|
| **S44** | **Superficial** | **35.8** | **1.0-1.8** | **1.2** | **2.0** | **1.7** |
| **S20** | **Deep** | **36.1** | **1.0-2.0** | **1.0** | **4.1** | **4.0** |

### 6.4.4 Measurement of hemangioma dimensions over time using static IR images

The thermal signature of hemangioma lesions discussed in foregoing sections conveys important information about the extent of the affected tissue and the activity level of the lesion. In addition to this, the change of lesion shape and size over time (from visit to visit) may be used to quantify the evolution of the lesion as well as the effects of treatment on the lesion. To investigate the area change of lesion contours over time, we acquired a pair of IR images for a subject with a hemangioma (S32) under treatment at two sessions as presented in Fig.6.9. The images shown in Figs.6.9 (a) and (b) were acquired on the day of the initial evaluation when the treatment was started. Image shown in Figs.6.9 (c) and (d) were taken 28 days later.

The WL image pair recorded during these two visits is displayed in Figs. 6.9 (a) and (c). Via WL-IR registration, the location of the visible lesion boundary is registered in the IR images as marked by the green contour lines in Figs.6.9 (b) and (d).

As we compare the thermal contours within the ROI in Fig.6.9(b) (orange and red in the ROI), we observe that these were largely present within the registered lesion boundary, whereas they shrank in size in Fig.6.9(d), which was recorded after 28 days of treatment. Moreover, the contours of the temperature above 36˚ C, which correspond to regions colored red and dark red in Fig.6.9(d), totally disappear from the lesion boundary after 28 days of treatment.

To contrast the area change of these high temperature contours, the area enclosed by the contours of $\Delta T \geq 1.5$˚C relative to the base temperature of 34˚C are presented in

Figs.6.9(e) and (f) for the two exams. The visible boundary of the lesion is marked by the red contour line. By comparing Fig.6.9(e) with Fig.6.9(f), we can observe that the area enclosed by the $\Delta T \geq 1.5^{\circ}$ C contour line, is largely presented within the visible lesion boundary in Fig.6.9(e). This area shrinks significantly within the lesion boundary in Fig.6.9(f). The longitudinal analysis of hemangioma under treatment suggests that the dimension change of isothermal contours, associated with the change of hyperthermic characteristics of the lesion, is potentially an indicator to evaluate the effectiveness of the treatment and the stage of evolution of the hemangioma lesion.

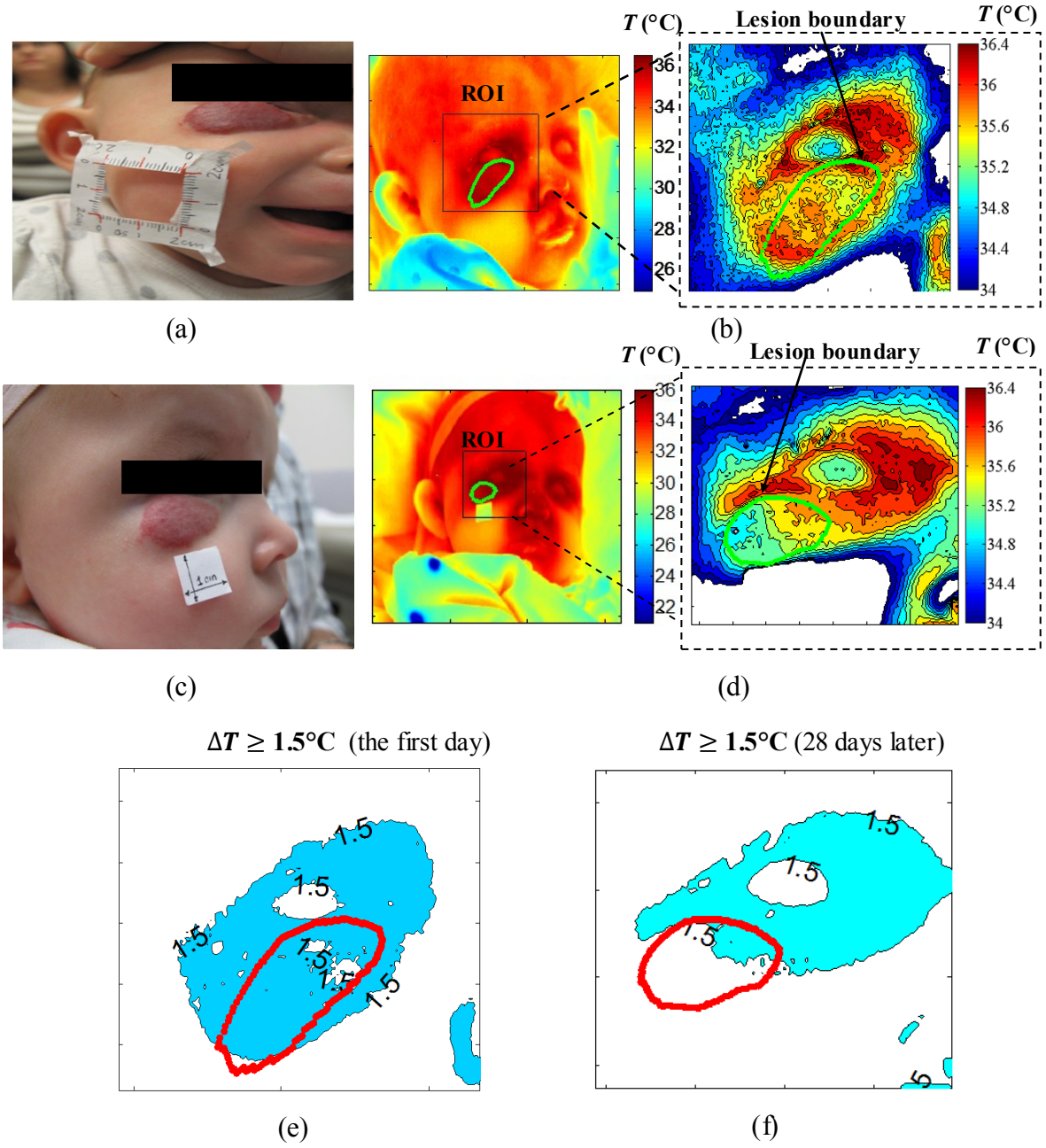


**Figure 6.9** (S32) White light images of the subject with hemangioma under treatment, acquired on the (a) 1st day and (c) 28 days later. IR images with ROI temperature contours acquired on the (b) 1st day and (d) 28 days later, respectively. The boundary of the visible lesion registered from the WL image is marked by the red contour in both cases in (e) and (f). Pixels enclosed by the temperature elevation of $\Delta T \geq 1.5^{\circ}$C relative to the baseline temperature of $34^{\circ}$C , acquired on the (e) 1st day and (f) 28 days later.

### 6.4.5 Dynamic IR image analysis for hemangioma lesions using a symmetrical location

Using the motion tracking method developed in Chapter 3, we can record the thermal recovery of hemangioma and compare it with the thermal recovery of a symmetrical location. For a subject with a lesion on the right cheek (S14), we acquired both static and dynamic IR images as shown in Figs.6.10 (a) and (b), respectively. The dynamic IR image sequence was acquired while the lesion temperature was recovering from the cooling, and Fig.6.10(b) is the first image in the thermal recovery phase. For comparison, the static and dynamic IR images of the left cheek, which was healthy (without lesion), were also acquired as control data (Figs.6.10 (c) and (d)). With the aid of the motion tracking algorithm, the thermal recovery temperatures for both cheeks were recorded over time, as plotted in Fig.6.11.

In the static IR images acquired before cooling, we can observe that the diseased cheek (Fig.6.10(a)) is warmer (inside the paper marker) than the healthy cheek (Fig.6.10(c)). After the cooling stress was applied and then removed, some residual hot spots can still be observed on the cheek with the lesion (Fig.6.10(b)), while the healthy cheek shows a uniform pattern of low temperature (Fig.6.10(d)). The different thermal patterns shown in Figs.6.10(b) and (d) suggest that the cheek with the lesion is cooled less than the healthy check under similar cooling conditions .

In the analysis of thermal recovery, the segmented pixels within the lesion boundary (272 pixels, marked by the green mesh grids in Fig.6.10(b)) are used to compute the mean lesion temperature during thermal recovery. As for the healthy cheek

in Fig.6.10(d), the pixels corresponding to the region under cooling (367 pixels) were selected to compute the mean temperature for comparison. Moreover, as indicated by the black circles in Figs.6.10(b) and (d), we also sampled the temperature at the location away from cooling (outside the paper marker) for reference. The temperature of the un-cooled location over time is plotted by the black dots in Figs.6.11(a) and (b). We can observe that the temperature of the uncooled location remains around 34˚C throughout the thermal recovery phase in both cases.

The results in Fig.6.11 suggest that the mean temperature of the diseased cheek recovered from 27˚C to 34.4˚C within 60 seconds (Fig.6.11(a)), while the mean temperature of the healthy cheek only recovered from 20˚C to 25˚C during the same period of time (Fig.6.11(b)). To present the differences more clearly, the recovery temperatures of both cheeks are plotted together in Fig.6.11(c). The diagram shows that the cheek with lesion recovered at the rate of 7 ˚C /60 s, which is faster than the thermal recovery rate of 5˚C /60 s for the healthy cheek.

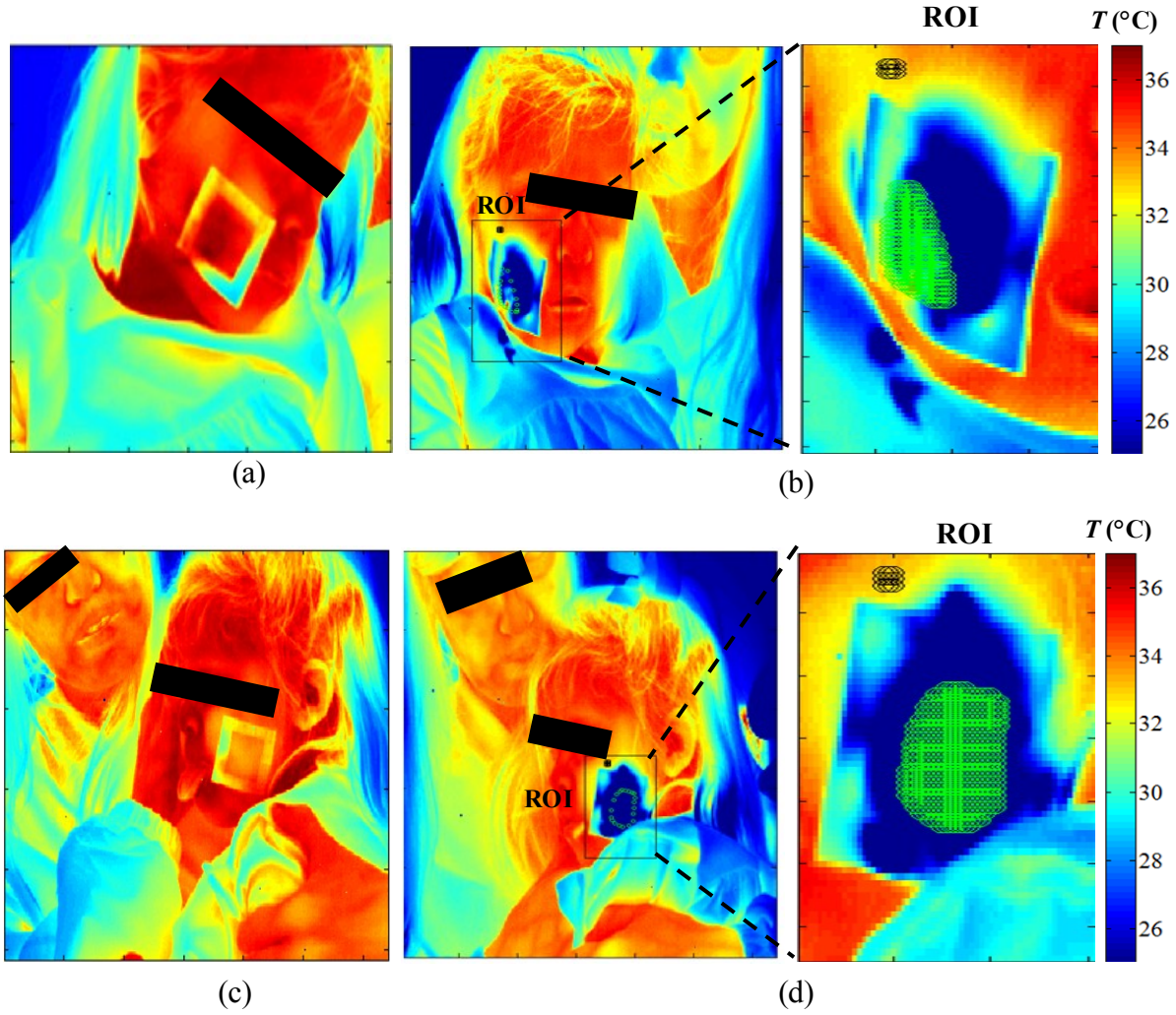


**Figure 6.10** (S14) (a) Static IR image of the right cheek (with lesion) of S14. (b) First frame of the dynamic IR image sequence after cooling (right cheek of S14), where the ROI serves as the template image for motion tracking. (c) Static IR image of the left cheek (without lesion) of S14. (d) First frame of the dynamic IR image sequence after cooling (left cheek of S14). In (b) and (d), the green grids represent the IR pixels segmented to compute the mean temperature during the thermal recovery, and the black circles represent the locations of the uncooled region at which the static skin temperature was recorded for reference.

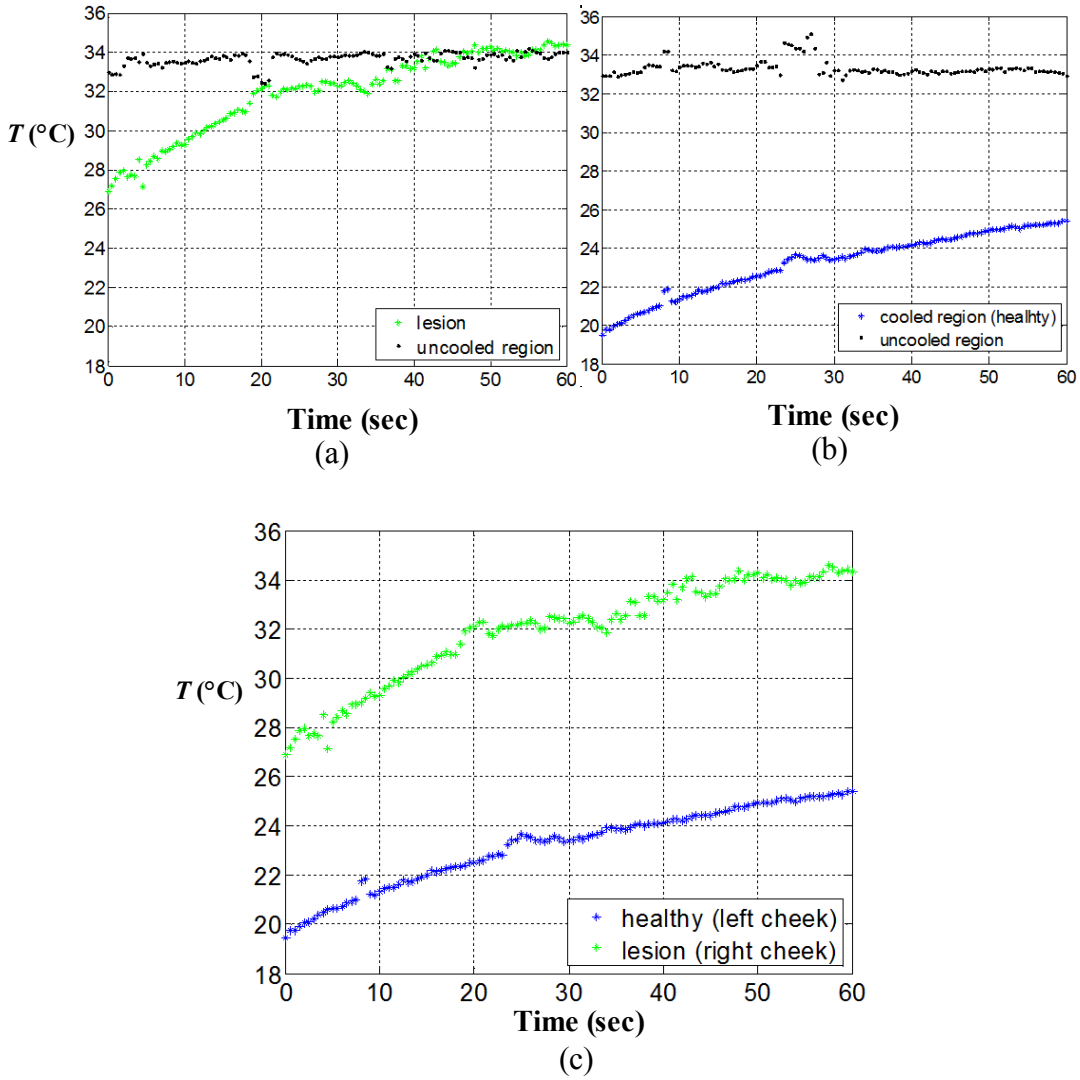


**Figure 6.11** (S14) Temperature of the (a) right cheek (with lesion) and (b) of the left cheek (without lesion) of patient S14 during the thermal recovery phase. Black dots represent the static temperature of the uncooled region in Fig.6.10(b) and Fig.6.10(d), respectively. (c) Temperatures of both cheeks of patient S14 during thermal recovery.

## 6.5 Conclusions and discussion

By applying static and dynamic IR imaging in a clinical setting, in this chapter we implemented a variety of quantitative techniques to analyze the thermal signatures of skin lesions with different characteristics. In the application of dynamic IR imaging for pigmented skin lesions, we verified the clinical performance of the motion tracking algorithm developed in Chapter 3. The motion tracking approach not only improves the accuracy of temperature measurements recorded from the IR images, but it also enables the application of image subtraction techniques to visualize the thermal recovery in the region of interest.

In addition, we demonstrated that static IR imaging can be utilized to assess the vascular network of hemangiomas relative non-invasively, quickly and inexpensively. We developed the technique of WL-IR image registration, which allows us to compare the location of visible portions of hemangiomas with their thermal signatures in the same IR image. The comparison indicates that the vascular hyperthermic activity of hemangioma often extends beyond the visible, superficial portion of the lesion observed in the white light images. This result implies that the visual inspection based purely on the redness or discoloration observed in the white light image may underestimate the extent of the skin area affected by hemangiomas. Furthermore, by comparing IR images of hemangioma at different times in a longitudinal assessment, we demonstrated that the change of dimension of the isothermal contours is associated with the regression (or growth during the early stage) of hemangioma. We showed examples of quantitative assessment of hemangioma using dynamic IR imaging with motion tracking, which allows us to compare the transient thermal signature of hemangioma along with the

healthy skin at the symmetrical location., The distinct difference between the behavior of hemangioma and healthy skin during thermal recovery suggests the potential use of dynamic IR imaging for quantitative assessment of lesions. In general, the clinical study indicates that IR images provide a more complete picture of hemangiomas and could thus serve as an informative, quantitative method to examine the condition of the lesion at the time of the exam as well as the evolution of the lesion over time.

In the clinical study some limitations of IR image acquisition and analysis were also identified. First, it is difficult to image lesions proximal to the eyes, which have stronger vascular activity than lesions at other locations, making the thermal signature of the lesion less distinctive. Second, for larger lesions, uniform cooling is more difficult to apply prior to dynamic IR imaging. Furthermore, for lesions located on a highly-curved skin surface, the WL-IR registration can become inaccurate due to the assumption of planar objects for the 2D projective transformation. Skin curvature also causes measurement errors associated with directional emissivity, as discussed in Chapters 4 and 5. Because of directional properties, lesion temperatures on curved surfaces are underestimated in measurements relying on IR imaging. Limitations related to skin curvature also stress the need for handheld IR cameras with 3D imaging capabilities in a clinical setting, which is on the horizon, as shown in Chapter 5.

# Chapter 7

# Conclusions and discussion

Infrared (IR) thermography is a non-invasive imaging modality that allows the measurement of the spatial/temporal variations of the infrared radiation emitted by the human body and captured by the two-dimensional (2D) focal plane array of the IR camera. In the medical applications of quantitative diagnostics, the challenge is the need to convert the radiation emitted by the complex three-dimensional (3D) shape of the human body into accurate temperature data with the desired order of $0.1^{o}C$ or better. Considering the challenges and demands in the clinical applications, in this work we tackled several aspects critical to the measurement accuracy in the attempt to advance the quantitative use of IR thermography in medical diagnostics.

In the analysis of skin cooling using computational model, we identified two types of thermal responses in the dynamic IR imaging of near-surface lesion. Shorter cooling leads to a maximum of thermal contrast within the first few seconds of thermal recovery. Longer cooling durations result in a maximum that is lower, broader and it appears later in time (20- 40 s after the removal of cooling). The computational model

was validated using data from in vivo dynamic IR imaging measurements. The analysis suggests that it is feasible to apply a moderate temperature (about 20 °C) to achieve effective skin cooling, with an acceptable cooling duration (< 2 min) in a clinical setting. This level of cooling could minimize the discomfort of patient. Furthermore, the analysis of skin cooling also provides a quantitative basis for the selection and optimization of cooling conditions in the clinical practice of dynamic IR imaging. To verify the theoretical relation between the cooling conditions (cooling temperature, cooling time, cooling method) and the thermographic thermal contrasts, further study based on the in-vivo experiments of IR imaging is expected.

We demonstrated that the motion tracking approach proposed in Chapter 3 is capable of following the involuntary motion of the subject in the IR image sequence, thereby allowing us to track the temperature evolution for a particular region on the skin. By a proper selection of the template image along with template update, the tracking results can be further improved for the IR image sequences acquired in thermal recovery phase. Furthermore, by implementing the motion tracking approach in the analysis of clinical data as presented in Chapter 6, we showed the achieved tracking accuracies are promising in terms of satisfying the demands imposed by the clinical applications. On the other hand, the proposed tracking approach is currently implemented in the post-processing stage. To allow the physician to interact with the measurement results and receive immediate feedback to adjust the imaging parameters as needed, it is advantageous to implement the tracking approach real-time in the stage of IR image acquisition.

Considering both the theoretical models of directional emissivity and the experimental results from phantom imaging, we developed an empirical formula in Chapter 4 to correct the curvature-induced artifacts in IR thermography. The empirical formula was further integrated into a devised 3D imaging methodology in the study of Chapter 5, which is based on a system combining Kinect and IR cameras. Using the system, we successfully demonstrated the feasibility of mapping the 2D IR thermography onto the 3D surface of human body, and the accuracy of temperature measurement was improved by the application of the empirical formula. However, considering the incomplete projection of temperature data on the 3D skin surface generated in Chapter 5, it is desirable to scan the multiple views of IR thermography for human body to generate a complete 3D thermographic reconstruction. Moreover, regarding the convenience and the affordability provided by the devised system, it is promising to facilitate the 3D IR thermographic imaging on the clinical site.

Based on the analysis of clinical data acquired from the patient studies previously conducted, the quantitative use of IR thermography for the measurement of pigmented lesions and hemangiomas was demonstrated in Chapter 6. We designed a variety of quantitative techniques to analyze the thermal signatures of lesions with different characteristics, measured in both static and dynamic IR imaging. The hands-on experiences gained from the clinical IR imaging also help us identify the future work to advance this technology in medical applications. In the diagnosis of hemangiomas, the longitudinal comparison based on the follow-up IR images for the same patient is of particular interest to evaluate the stage of tumor under treatment. To make the comparison quantitatively valid, the longitudinal study of IR thermography will require a

standardized imaging environment, in which the imaging conditions (ambient temperature, focal length, imaging time, the positioning of patient, and etc) are accurately controlled. Additionally, we found the process of image analysis was time consuming. It is our hope to develop a software platform with a single user interface to unify each individual task (WL-IR registration, ROI selection, input parameters for contours mapping and motion tracking, and etc) for image analysis, which will make the whole process more automatic and efficient. Finally, we identified the potential use of 3D IR thermography on the clinical site, which is capable of combining the volumetric and thermal information as demonstrated in Chapter 5, and thus a more complete picture can be provided for hemangiomas in terms of the relation between tumor size and temperature.

For the quantitative use of IR thermography in medical applications, we believe the knowledge obtained in this work can be helpful to improve the technology in both feasibility and delicacy. It is our hope that IR imaging will become the standard modality in clinics to provide an accurate, non-invasive, efficient, and affordable healthcare.

# Bibliography

[1] T.M. Button, H. Li, P. Fisher, R. Rosenblatt, K. Dulaimy, S. Li, B. O'Hea, M. Salvitti, V. Geronimo, C. Geronimo, S. Jambawalikar, P. Carvelli, R. Weiss, "Dynamic infrared imaging for the detection of malignancy", *Phys. Med. Biol.*, 49 (2004) 3105-3116.

[2] M.P. Cetingul, C. Herman, "A heat transfer model of skin tissue for the detection of lesions: sensitivity analysis", *Phys. Med. Biol.*, 55 (2010) 5933-5951.

[3] M.P. Cetingul, H.E. Cetingul, C. Herman, "Analysis of transient thermal images to distinguish melanoma from dysplastic nevi", *Proceedings of SPIE Medical Imaging 2011: Computer-Aided Diagnosis*, 2011.

[4] M.P. Cetingul, C. Herman, "Quantification of the thermal signature of a melanoma lesion", *Int. J. Therm. Sci.*, 50 (2011) 421-431.

[5] M.P. Cetingul, C. Herman, "The assessment of melanoma risk using the dynamic infrared imaging technique", *J. Thermal Sci. Eng. Appl.*, 3(3) (2011) 031006.

[6] C. Herman, M.P. Cetingul, "Quantitative visualization and detection of skin cancer using dynamic thermal imaging", *J. Vis. Exp.*, (2011).

[7] C. Herman, "Emerging technologies for the detection of melanoma: achieving better outcomes", *Clin. Cosmet. Investig. Dermatol.*, 5 (2012) 195-212.

[8] C. Herman, "The role of dynamic infrared imaging in melanoma diagnosis", *Expert Rev. Dermatol.*, 8 (2013) 177-184.

[9] M. Gautherie, "Thermobiological assessment of benign and malignant breast diseases", *Am. J. Obstet. Gynecol.*, 147 (1983) 861-869.

[10] A.J. Collins, E.F.J. Ring, J.A. Cosh, P.A. Bacon, "Quantitation of thermography in arthritis using multi-isothermal analysis .1. Thermographic index", *Ann. Rheum. Dis.*, 33 (1974) 113-&.

[11] P. Aksenov, I. Clark, D. Grant, A. Inman, L. Vartikovski, J.-c. Nebel, "3D thermography for quantification of heat generation resulting from inflammation ", *8th 3D modelling symposium*, 2003.

[12] X.Y. Ju, J.C. Nebel, J.P. Siebert, "3D thermography imaging standardization technique for inflammation diagnosis", *Proceedings of SPIE Infrared Components and Their Applications*, 2005, 266-273.

[13] M.P. Cetingul, "Using high resolution infrared imaging to detect melanoma and dysplastic nevi", *Ph.D. dissertation, Johns Hopkins University*, (2010).

[14] R. Marchesini, A. Bono, C. Bartoli, M. Lualdi, S. Tomatis, N. Cascinelli, "Optical imaging and automated melanoma detection: questions and answers", *Melanoma Res.*, 12 (2002) 279-286.

[15] A.A. Marghoob, L.D. Swindle, C.Z. Moricz, F.A. Sanchez Negron, B. Slue, A.C. Halpern, A.W. Kopf, "Instruments and new technologies for the in vivo diagnosis of melanoma", *J. Am. Acad. Dermatol.*, 49 (2003) 777-797; quiz 798-779.

[16] S.Q. Wang, H. Rabinovitz, A.W. Kopf, M. Oliviero, "Current technologies for the in vivo diagnosis of cutaneous melanomas", *Clin. Dermatol.*, 22 (2004) 217-222.

[17] E.L. Psaty, A.C. Halpern, "Current and emerging technologies in melanoma diagnosis: the state of the art", *Clin. Dermatol.*, 27 (2009) 35-45.

[18] J.K. Patel, S. Konda, O.A. Perez, S. Amini, G. Elgart, B. Berman, "Newer technologies/techniques and tools in the diagnosis of melanoma", *Eur. J. Dermatol.*, 18 (2008) 617-631.

[19] E.B. Silberstein, G.K. Bahr, J. Kattan, "Thermographically measured normal skin temperature asymmetry in the human male", *Cancer*, 36 (1975) 1506-1510.

[20] L.J. Jiang, E.Y. Ng, A.C. Yeo, S. Wu, F. Pan, W.Y. Yau, J.H. Chen, Y. Yang, "A perspective on medical infrared imaging", *J. Med. Eng. Technol.*, 29 (2005) 257-267.

[21] D.A. Kennedy, T. Lee, D. Seely, "A comparative review of thermography as a breast cancer screening technique", *Integr. Cancer. Ther.*, 8 (2009) 9-16.

[22] R.S. Handley, "The temperature of breast tumors as a possible guide to prognosis", *Acta Unio. Int. Contra. Cancrum.*, 18 (1962).

[23] M. Gautherie, C.M. Gros, "Breast thermography and cancer risk prediction", *Cancer*, 45 (1980) 51-56.

[24] K. Ammer, E.F. Ring, Standard procedures for infrared imaging in medicine, in: Bronzino J.D. (Ed.) Biomedical Engineering Handbook, 3rd ed.,Medical Systems and Devices, CRC Press, 2006, pp. 32-31 - 32-14.

[25] SEER stat fact sheets: melanoma of the skin, in, National Cancer Institute, Bethesda, MD 2012.

[26] C.M. Balch, A.C. Buzaid, S.J. Soong, M.B. Atkins, N. Cascinelli, D.G. Coit, I.D. Fleming, J.E. Gershenwald, A. Houghton, J.M. Kirkwood, K.M. McMasters, M.F. Mihm, D.L. Morton, D.S. Reintgen, M.I. Ross, A. Sober, J.A. Thompson, J.F. Thompson, "Final version of the american joint committee on cancer staging system for cutaneous melanoma", *J. Clin. Oncol.*, 19 (2001) 3635-3648.

[27] Official website of skin cancer foundation - Skin Cancer Facts, in, 2011.

[28] J. Cary, L. Kalisher, N. Sadowsky, B. Mikic, "Thermal evaluation of breast disease using local cooling", *Radiology*, 115 (1975) 73-77.

[29] H.H. Pennes, "Analysis of tissue and arterial blood temperatures in the resting human forearm", *J. Appl. Physiol.*, 1 (1948) 93-122.

[30] I.A. Lubashevsky, V.V. Gafiychuk, "Mathematical description of the heat transfer in living tissue (Part 1) ", *Adap-org/9911001*, (2004).

[31] C.K. Charny, "Mathematical models of bioheat transfer", *Adv. Heat Trans.*, 22 (1992) 19-155.

[32] H. Arkin, L.X. Xu, K.R. Holmes, "Recent developments in modeling heat-transfer in blood-perfused tissues", *IEEE Trans. Biomed. Eng.*, 41 (1994) 97-107.

[33] J. Crezee, J. Mooibroek, J.J.W. Lagendijk, G.M.J. Vanleeuwen, "The theoretical and experimental evaluation of the heat-balance in perfused tissue", *Phys. Med. Biol.*, 39 (1994) 813-832.

[34] M. Stanczyk, J.J. Telega, "Modelling of heat transfer in biomechanics—a review. part I. Soft Tissues", *Acta Bioeng. Biomech.*, 4 (2002) 31-61.

[35] A.R.A. Khaled, K. Vafai, "The role of porous media in modeling flow and heat transfer in biological tissues", *Int. J. Heat Mass Tran.*, 46 (2003) 4989-5003.

[36] F. Xu, T.J. Lu, K.A. Seffen, E.Y.K. Ng, "Mathematical modeling of skin bioheat transfer", *Appl. Mech. Rev.*, 62 (2009).

[37] S. Mahjoob, K. Vafai, "Analytical characterization of heat transport through biological media incorporating hyperthermia treatment", *Int. J. Heat Mass Tran.*, 52 (2009) 1608-1618.

[38] S. Mahjoob, K. Vafai, "Analysis of bioheat transport through a dual layer biological media", *J. Heat Trans-T. Asme*, 132 (2010).

[39] S. Mahjoob, K. Vafai, "Analytical characterization and production of an isothermal surface for biological and electronic applications", *J. Heat Trans-T. Asme*, 131 (2009).

[40] S. Mahjoob, K. Vafai, "Analysis of heat transfer in consecutive variable cross-sectional domains: applications in biological media and thermal management", *J. Heat Trans-T. Asme*, 133 (2011).

[41] A. Bhargava, A. Chanmugam, C. Herman, "Heat transfer model for deep tissue injury: a step towards an early thermographic diagnostic capability", *Diagn. Pathol.*, 9 (2014) 36.

[42] J.G. Zaspel, H.M. Schnell, "Cooling extensive burns: sprayed coolants can improve initial cooling management - a thermography-based study", *Burns*, 34 (2008) 505-508.

[43] P. Axelrod, "External cooling in the management of fever", *Clin. Infect. Dis.*, 31 (2000) S224-S229.

[44] C.H. Wyndham, N.B. Strydom, H.M. Cooke, J.S. Maritz, J.F. Morrison, P.W. Fleming, J.S. Ward, "Methods of cooling subjects with hyperpyrexia", *J. Appl. Physiol.*, 14 (1959) 771-776.

[45] H.H. Zenzie, G.B. Altshuler, M.Z. Smirnov, R.R. Anderson, "Evaluation of cooling methods for laser dermatology", *Laser. Surg. Med.*, 26 (2000) 130-144.

[46] R.G. Wheeland, Cutaneous surgery, Philadelphia: WB Saunders, 1994.

[47] B.A. Gilchrest, S. Rosen, J.M. Noe, "Chilling port wine stains improves the response to argon-laser therapy", *Plast. Reconstr. Surg.*, 69 (1982) 278-283.

[48] E. Armon, G. Laufer, "New techniques for reducing the thermochemical damage in the course of laser-surgery", *Laser. Surg. Med.*, 7 (1987) 162-168.

[49] C. Chess, Q. Chess, "Cool laser optics treatment of large telangiectasia of the lower extremities", *J. Dermatol. Surg. Oncol.*, 19 (1993) 74-80.

[50] B. Dreno, T. Patrice, P. Litoux, H. Barriere, "The benefit of chilling in argon-laser treatment of port-wine stains", *Plast. Reconstr. Surg.*, 75 (1985) 42-45.

[51] A.J. Welch, M. Motamedi, A. Gonzalez, Evaluation of cooling techniques for the protection of the epidermis during Nd-YAG laser irradiation of the skin, in: Joffe S.N. (Ed.) Neodymium-YAG laser in medicine and surgery, Elsevier, New-York 1983, pp. 195-204.

[52] A. Di Carlo, "Thermography and the possibilities for its applications in clinical and experimental dermatology", *Clin. Dermatol.*, 13 (1995) 329-336.

[53] T.M. Buzug, S. Schumann, L. Pfaffmann, U. Reinhold, J. Ruhlmann, "Functional infrared imaging for skin-cancer screening", *Conf. Proc. IEEE Eng. Med. Biol. Soc.*, 1 (2006) 2766-2769.

[54] G.A. Santa Cruz, J. Bertotti, J. Marin, S.J. Gonzalez, S. Gossio, D. Alvarez, B.M. Roth, P. Menendez, M.D. Pereira, M. Albero, L. Cubau, P. Orellano, S.J. Liberman, "Dynamic infrared imaging of cutaneous melanoma and normal skin in patients treated with BNCT", *Appl. Radiat. Isot.*, 67 (2009) S54-58.

[55] C. Herman, M.P. Cetingul, "In-vivo detection of skin cancer using the dynamic infrared imaging technique", *J. Heat Trans-T. Asme*, 133 (2011).

[56] A.S. Ahuja, K.N. Prasad, W.R. Hendee, P.L. Carson, "Thermal conductivity and diffusivity of neuroblastoma tumor", *Med. Phys.*, 5 (1978) 418-421.

[57] S.B. Wilson, V.A. Spence, "A tissue heat transfer model for relating dynamic skin temperature changes to physiological parameters", *Phys. Med. Biol.*, 33 (1988) 895-912.

[58] J. Werner, M. Buse, "Temperature profiles with respect to inhomogeneity and geometry of the human body", *J. Appl. Physiol.*, 65 (1988) 1110-1118.

[59] D.A. Torvi, J.D. Dale, "A finite-element model of skin subjected to a flash fire", *J. Biomech. Eng-T. Asme*, 116 (1994) 250-255.

[60] F.A. Duck, "Physical properties of tissue : a comprehensive reference book", *London : Academic Press*, (1990).

[61] C.W. Song, A. Lokshina, J.G. Rhee, M. Patten, S.H. Levitt, "Implication of blood flow in hyperthermic treatment of tumors", *IEEE Trans. Biomed. Eng.*, 31 (1984) 9-16.

[62] J.W. Draper, J.W. Boag, "Skin temperature distributions over veins and tumours", *Phys. Med. Biol.*, 16 (1971) 645-656.

[63] Z.S. Deng, J. Liu, "Mathematical modeling of temperature mapping over skin surface and its implementation in thermal disease diagnostics", *Comput. Biol. Med.*, 34 (2004) 495-521.

[64] K.R. Pardasani, N. Adlakha, "Exact solution to a heat-flow problem in peripheral tissue layers with a solid tumor in the dermis", *Indian. J. Pure Appl. Math.*, 22 (1991) 679-687.

[65] B.F. Jones, "A reappraisal of the use of infrared thermal image analysis in medicine", *IEEE T. Med. Imaging*, 17 (1998) 1019-1027.

[66] J. Steketee, "Spectral emissivity of skin and pericardium", *Phys. Med. Biol.*, 18 (1973) 686-694.

[67] D.J. Watmough, P.W. Fowler, R. Oliver, "The thermal scanning of a curved isothermal surface: implications for clinical thermography", *Phys. Med. Biol.*, 15 (1970) 1-8.

[68] T.Y. Cheng, C. Herman, "Involuntary motion tracking for medical dynamic infrared thermography using a template-based algorithm", *Proceedings of SPIE Medical Imaging 2013: Image Processing*, 2013.

[69] T.Y. Cheng, C. Herman, "Motion tracking in infrared imaging for quantitative medical diagnostic applications", *Infrared Phys. Technol.*, 62 (2014) 70-80.

[70] C. Dai, Y. Zheng, X. Li, "Layered representation for pedestrian detection and tracking in infrared imagery", *2nd Joint IEEE International Workshop on Object Tracking and Classification in and Beyond the Visible Spectrum* 2005.

[71] M. Yasuno, N. Yasuda, M. Aoki, "Pedestrian detection and tracking in far infrared images", *Conference on Computer Vision and Pattern Recognition Workshop*, 2004, 125-131.

[72] J. Zhou, J. Hoang, "Real-time robust human detection and tracking system", *2nd Joint IEEE International Workshop on Object Tracking and Classification in and Beyond the Visible Spectrum*, 2005.

[73] M. Anbar, C. Brown, L. Milescu, J. Babalola, L. Gentner, "The potential of dynamic area telethermometry in assessing breast cancer - Emphasizing physiological information in the diagnosis and management of breast cancer", *IEEE Eng. Med. Biol. Mag.*, 19 (2000) 58-62.

[74] M. Anbar, L. Milescu, A. Naumov, C. Brown, T. Button, C. Carty, K. AlDulaimi, "Detection of cancerous breasts by dynamic area telethermometry", *IEEE Eng. Med. Biol. Mag.*, 20 (2001) 80-91.

[75] M. Anbar, "Assessment of physiologic and pathologic radiative heat dissipation using dynamic infrared imaging", *Ann. Ny. Acad. Sci.*, 972 (2002) 111-118.

[76] V. Agostini, S. Delsanto, F. Molinari, M. Knaflitz, "Evaluation of feature-based registration in dynamic infrared imaging for breast cancer diagnosis", *Conf. Proc. IEEE Eng. Med. Biol. Soc.*, 1 (2006) 953-956.

[77] V. Agostini, S. Delsanto, M. Knaflitz, F. Molinari, "Noise estimation in infrared image sequences: a tool for the quantitative evaluation of the effectiveness of registration algorithms", *IEEE Trans. Biomed. Eng.*, 55 (2008) 1917-1920.

[78] V. Agostini, M. Knaflitz, F. Molinari, "Motion artifact reduction in breast dynamic infrared imaging", *IEEE Trans. Biomed. Eng.*, 56 (2009) 903-906.

[79] B.J. Fan, Y.K. Du, L.L. Zhu, J. Sun, Y.D. Tang, "A robust template tracking algorithm with weighted active drift correction", *Pattern Recogn. Lett.*, 32 (2011) 1317-1327.

[80] D. Schreiber, "Robust template tracking with drift correction", *Pattern Recogn. Lett.*, 28 (2007) 1483-1491.

[81] P. Mitra, C.A. Murthy, S.K. Pal, "Unsupervised feature selection using feature similarity", *IEEE Trans. Pattern Anal. Mach. Intell.*, 24 (2002) 301-312.

[82] P. Tissainayagam, D. Suter, "Object tracking in image sequences using point features", *Pattern Recogn.*, 38 (2005) 105-113.

[83] D. Freedman, T. Zhang, "Active contours for tracking distributions", *IEEE Trans. Image Process.*, 13 (2004) 518-526.

[84] N. Paragios, R. Deriche, "Geodesic active contours and level sets for the detection and tracking of moving objects (vol22, pg 279, 2000)", *IEEE Trans. Pattern Anal. Mach. Intell.*, 22 (2000) 415-415.

[85] B. Bascle, R. Deriche, "Region tracking through image sequences", *Proceedings of Fifth International Conference on Computer Vision*, 1995, 302-307.

[86] A.D. Jepson, D.J. Fleet, T.F. El-Maraghi, "Robust online appearance models for visual tracking", *IEEE Trans. Pattern Anal. Mach. Intell.*, 25 (2003) 1296-1311.

[87] B.D. Lucas, T. Kanade, "An iterative image registration technique with an application to stereo vision.", *Proceedings of the International Joint Conference on Artificial Intelligence*, 1981, 674-679.

[88] D. Comaniciu, V. Ramesh, P. Meer, "Kernel-based object tracking", *IEEE Trans. Pattern Anal. Mach. Intell.*, 25 (2003) 564-577.

[89] I. Matthews, T. Ishikawa, S. Baker, "The template update problem", *IEEE Trans. Pattern Anal. Mach. Intell.*, 26 (2004) 810-815.

[90] S. Baker, I. Matthews, "Lucas-Kanade 20 years on: A unifying framework", *Int. J. Comput. Vision.*, 56 (2004) 221-255.

[91] T. Ishikawa, I. Matthews, S. Baker, "Efficient image alignment with outlier rejection, technical report", *CMU-RI-TR-02-27, Carnegie Mellon University Robotics Institute*, (2002).

[92] S. Baker, R. Gross, I. Matthews, Lucas–Kanade 20 years on: A unifying framework: Part 2, in: Technical Report CMU-RI-TR-03-0, Carnegie Mellon University Robotics Institute, 2003.

[93] M.P. Cetingul, C. Herman, R.M. Alani, "Skin imaging with infrared thermography and confocal microscopy", *Ht2009: Proceedings of the ASME Summer Heat Transfer*, 2009, 731-739.

[94] in, MATLAB Central

<http://www.mathworks.com/matlabcentral/fileexchange/24677-lucas-kanade-affine-template-tracking>, 2009.

[95] L. Grady, "Random walks for image segmentation", *IEEE Trans. Pattern Anal. Mach. Intell.*, 28 (2006) 1768-1783.

[96] R. Hartley, A. Zisserman, Multiple View Geometry in Computer Vision, 2 ed., Cambridge University Press, 2004.

[97] C. Harris, M. Stephens, "A combined corner and edge detector", *Proceedings of the 4th Alvey Vision Conference*, 1988, 147-151.

[98] J.B. Shi, C. Tomasi, "Good features to track", *IEEE Computer Society Conference on Computer Vision and Pattern Recognition*, 1994, 593-600.

[99] T. Cheng, C. Herman, "Optimization of skin cooling for thermographic imaging of near-surface lesions", *IMECE2011:Proceedings of the ASME 2011 International Mechanical Engineering Congress & Exposition*, 2011, 351-360.

[100] T.M. Buzug, S. Schumann, L. Pfaffmann, U. Reinhold, J. Ruhlmann, "Skin-tumour classification with functional infrared imaging", *Proceedings of the Eighth IASTED International Conference on Signal and Image Processing*, 2006, 313-322.

[101] J.A. Clark, "Effects of surface emissivity and viewing angle errors in thermography", *Acta thermographica*, 1 (1976) 138-141.

[102] C.J. Martin, D.J. Watmough, "Thermal scanning of curved surfaces", *Acta thermographica*, 2 (1977) 18-22.

[103] R.E. Woodrough, Medical Infra-red Thermography: Principles and Practice, Cambridge: Cambridge University Press, 1982.

[104] C.J. Ash, E. Gotti, C.H. Haik, "Thermography of the curved living skin surface", *Mo Med.*, 84 (1987) 702-708.

[105] M. Anbar, "Potential artifacts in infrared thermographic measurements", *Thermology*, 273 (1991) 3.

[106] S. Hejazi, R. Spangler, "Theoretical modeling of skin emissivity", *Proceedings of the Annual International Conference of the IEEE Engineering in Medicine and Biology Society*, 1992, 258-259.

[107] R. Siegel, J.R. Howell, Thermal Radiation Heat Transfer, 3 ed., Taylor & Francis Inc, Hemisphere, Washington, 1992.

[108] M.E. Thomas, Optical Propagation in Liquids in: Optical Propagation in Linear Media Oxford University Press 2006 pp. 423-442

[109] M.E. Thomas, Applied Physics Laboratory at Johns Hopkins University, 2015.

[110] M.R. Querry, D.M. Wieliczka, D.J. Segelstein, Handbook of Optical Constants of Solids II, Academic Press, San Diego, 1991.

[111] "Emissivity Coefficients of some common Materials", *http://www.engineeringtoolbox.com/emissivity-coefficients-d_447.html*.

[112] S. Nakamura, M. Saito, L.F. Huang, M. Miyagi, K. Wada, "Infrared optical-constants of anodic alumina films with micropore arrays", *Japanese Journal of Applied Physics Part 1-Regular Papers Short Notes & Review Papers*, 31 (1992) 3589-3593.

[113] D.W. Lewis, H.O. Goller, C.D. Teates, "Apparent temperature degradation in thermograms of human anatomy viewed obliquely", *Radiology*, 106 (1973) 95-99.

[114] G. Sansoni, M. Trebeschi, F. Docchio, "State-of-the-art and applications of 3D imaging sensors in industry, cultural heritage, medicine, and criminal investigation", *Sensors*, 9 (2009) 568-601.

[115] K. Khoshelham, S.O. Elberink, "Accuracy and resolution of kinect depth data for indoor mapping applications", *Sensors*, 12 (2012) 1437-1454.

[116] P. Henry, M. Krainin, E. Herbst, X.F. Ren, D. Fox, "RGB-D mapping: Using Kinect-style depth cameras for dense 3D modeling of indoor environments", *Int. J. Robot. Res.*, 31 (2012) 647-663.

[117] V. Hilsenstein, "Surface reconstruction of water waves using thermographic stereo imaging", *Proceedings of Image and Vision Computing New Zealand, Dunedin, New Zealand*, 2005, 102-107.

[118] Y.H.Ng, R.Du, "Acquisition of 3D surface temperature distribution of a car body", *Proceedings of IEEE International Conference on Information Acquisition*, 2005, 16-20.

[119] C. Rocchini, P. Cignoni, C. Montani, P. Pingi, R. Scopigno, "A low cost 3D scanner based on structured light", *Comput. Graph. Forum*, 20 (2001) C299-+.

[120] L. Ciupitu, A.N. Ivanescu, S. Chivescu, S. Brotac, "Vision system for human body infrared thermography", *Annals of Daaam for 2009 & Proceedings of the 20th International Daaam Symposium*, 2009, 1545-1546.

[121] R.Q. Yang, Y.Z. Chen, "Design of a 3-D infrared imaging system using structured light", *IEEE T. Instrum. Meas.*, 60 (2011) 608-617.

[122] I. Grubisic, L. Gjenero, T. Lipic, I. Sovic, T. Skala, "Medical 3D thermography system", *Periodicum Biologorum*, 113 (2011) 401-406.

[123] J. Shotton, T. Sharp, A. Kipman, A. Fitzgibbon, M. Finocchio, A. Blake, M. Cook, R. Moore, "Real-time human pose recognition in parts from single depth images", *Communications of the Acm*, 56 (2013) 116-124.

[124] K. Skala, T. Lipic, I. Sovic, L. Gjenero, I. Grubisic, "4D thermal imaging system for medical applications", *Periodicum Biologorum*, 113 (2011) 407-416.

[125] H.P. Oliveira, P. Patete, G. Baroni, J.S. Cardoso, "Development of a BCCT quantitative 3D evaluation system through low-cost solutions", *Proceedings of the 2nd International Conference on 3D body Scanning Technologies*, 2011, 16-27.

[126] G. Lu, G.N. DeSouza, J. Armer, B. Anderson, C.-R. Shyu, "A system for limb-volume measurement using 3D models from an infrared depth sensor", *Computational Intelligence in Healthcare and e-health (CICARE), 2013 IEEE Symposium on*, 2013, 64-69.

[127] G. Cardone, A. Ianiro, G. dello Ioio, A. Passaro, "Temperature maps measurements on 3D surfaces with infrared thermography", *Exp. Fluids*, 52 (2012) 375-385.

[128] S. Colantonio, M. Benvenuti, M.G. Di Bono, G. Pieri, O. Salvetti, "Object tracking in a stereo and infrared vision system", *Infrared Phys. Technol.*, 49 (2007) 266-271.

[129] in, Official website of ReconstructMe (PROFACTOR)

http://reconstructme.net/, 2015.

[130] C.D. Herrera, J. Kannala, J. Heikkila, "Joint depth and color camera calibration with distortion correction", *IEEE Trans. Pattern Anal. Mach. Intell.*, 34 (2012) 2058-2064.

[131] C.D. Herrera, Kinect Calibration Toolbox, in, http://www.ee.oulu.fi/~dherrera/kinect/, 2012.

[132] J. Heikkila, "Geometric camera calibration using circular control points", *IEEE Trans. Pattern Anal. Mach. Intell.*, 22 (2000) 1066-1077.

[133] K.E. Holland, B.A. Drolet, "Infantile hemangioma", *Pediatr. Clin. North. Am.*, 57 (2010) 1069-1083.

[134] A.N. Haggstrom, B.A. Drolet, E. Baselga, S.L. Chamlin, M.C. Garzon, K.A. Horii, A.W. Lucky, A.J. Mancini, D.W. Metry, B. Newell, A.J. Nopper, I.J. Frieden, "Prospective study of infantile hemangiomas: clinical characteristics predicting complications and treatment", *Pediatrics*, 118 (2006) 882-887.

[135] B.A. Drolet, N.B. Esterly, I.J. Frieden, "Hemangiomas in children", *N. Engl. J. Med.*, 341 (1999) 173-181.

[136] C. Kilcline, I.J. Frieden, "Infantile Hemangiomas: How Common Are They? A systematic review of the medical literature", *Pediatr. Dermatol.*, 25 (2008) 168-173.

# Vita

Tze-Yuan Cheng received his B.S degree in Mechanical Engineering and M.S degree in Biomedical Engineering from National Taiwan University (NTU), Taipei, Taiwan in 2003 and 2005, respectively. He then joined Taiwan Diplomatic Alternative Service Program during 2005-2006 and worked as a medical engineer assistant in Mzuzu Central Hospital, Republic of Malawi. After finishing the fourteen-month oversea service, he worked as an assistant engineer in National Instruments (NI) Taiwan in 2007, and safety assessment engineer in Underwriters Laboratories (UL) Taiwan in 2008. He moved to United States to pursue PhD degree in 2009, and then he received his M.S.E degree in Mechanical Engineering from The Johns Hopkins University, Baltimore, Maryland in 2011. In 2015, he completed his doctoral study.